GEOCHEMICAL STUDIES OF THE CORES OF

TERRESTRIAL PLANETARY BODIES

by

Nancy Lynne Chabot

A Dissertation Submitted to the Faculty of the

DEPARTMENT OF PLANETARY SCIENCES

In Partial Fulfillment of the Requirements
For the Degree of

DOCTOR OF PHILOSOPHY

In the Graduate College

THE UNIVERSITY OF ARIZONA

1999

INFORMATION TO USERS

GEOCHEMICAL STUDIES OF THE CORES OF

TERRESTRIAL PLANETARY BODIES

by

Nancy Lynne Chabot

A Dissertation Submitted to the Faculty of the

DEPARTMENT OF PLANETARY SCIENCES

In Partial Fulfillment of the Requirements
For the Degree of

DOCTOR OF PHILOSOPHY

In the Graduate College

THE UNIVERSITY OF ARIZONA

1999

UMI Number: 9957965

Copyright 1999 by
Chabot, Nancy Lynne

All rights reserved.

UMI®

THE UNIVERSITY OF ARIZONA ®
GRADUATE COLLEGE

As members of the Final Examination Committee, we certify that we have

read the dissertation prepared by___Nancy Lynne Chabot_____

entitled ___Geochemical Studies of the Cores of Terrestrial Planetary___

_____Bodies_____

_____

_____

_____

and recommend that it be accepted as fulfilling the dissertation

requirement for the Degree of ___Doctor of Philosophy_____

_____   __11/5/99__
Michael J. Drake   Date

_____   __11/5/99__
John S. Lewis   Date

_____   __11/5/99__
Carolyn C. Porco   Date

_____   __11/5/99__
Peter H. Smith   Date

_____   __11/5/99__
Timothy D. Swindle   Date

Final approval and acceptance of this dissertation is contingent upon
the candidate's submission of the final copy of the dissertation to the
Graduate College.

I hereby certify that I have read this dissertation prepared under my
direction and recommend that it be accepted as fulfilling the dissertation
requirement.

_____   __11/5/99__
Dissertation Director Michael J. Drake   Date
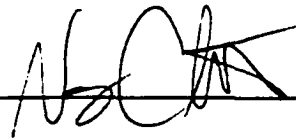
STATEMENT BY AUTHOR

This dissertation has been submitted in partial fulfillment of requirements for an advanced degree at The University of Arizona and is deposited in the University Library to be made available to borrowers under rules of the Library.

Brief quotations from this dissertation are allowable without special permission, provided that accurate acknowledgment of source is made. Requests for permission for extended quotation from or reproduction of this manuscript in whole or in part may be granted by the copyright holder.

SIGNED: _____

ACKNOWLEDGEMENTS

Every time I think about it, I feel very lucky for my graduate school experience. Over these years, I've been asked more than once if I worried about finding a job when I finished. I've always answered that I enjoyed what I was currently doing and wouldn't want to be doing anything else. I've always meant it and always will.

Limiting the acknowledgements to one page is perhaps a blessing in disguise. There are so many people who have, at one time or another, helped me out in a way I will always remember. I appreciate all those times more than you probably know. Especially, there are numerous current and previous LPL grad students who have done everything for me, from taking me out and reminding me there is more to life, to listening to me and letting me know they were there. I could not begin to thank you all in this page, but don't doubt how much it has meant to me.

Five years ago, I would have never guessed Mike Drake would become my advisor. Today, I wouldn't want to imagine it any other way. For me, Mike has been the ideal advisor. He has always encouraged me to follow my own ideas. He has given me confidence when I needed it most. And he has offered me so much support throughout my grad years, both intellectual and moral. For all of this and more I am very thankful.

Chris Capobianco and Kevin Righter have both spent numerous hours answering my many questions, teaching me lab procedures, and just being available. They have been like advisors to me, and I am very grateful for all of their efforts. I can honestly say that a lot of what I have learned in grad school, I have learned from them.

As for my dissertation research, I'd like to acknowledge that it was supported by a NASA GSRP grant for three years and thank my dissertation committee for their time. I also appreciate that during my graduate years I have had opportunities to experience more than just my dissertation research. I thank Peter Smith for giving me the opportunity to assist with the calibrations of IMP and be part of the team. I thank Dave Kring for letting me help in the classification of new meteorites, for the interest he has shown in my work, and for the many supportive words he has given me. I thank Ralph Harvey for the unique opportunity to be a member of the ANSMET field team; it will always be one of my fondest memories. I thank Greg Hoppa and Bob Strom for being co-authors on our lunar lineaments paper. I thank quite a few observers in the department, especially Bob Brown, who have let me tag along on runs and exposed me to research very different from my own. I also thank the JPL workshop program for teaching me about spacecraft design and sending me to the Pathfinder launch.

Throughout most of my years in Tucson, there have been two people who have been very important to me. I can not imagine what my life would have been like without either of them nor do I want to. I have relied on them, and they have seen me through a lot. I honestly feel my life is richer consequently. To David Trilling: thank you for always believing in me. To Nick Rossett: thank you for being a friend like no other.

To Michelle Chabot: thank you for being a good sister, especially when I've most needed one. And to my parents, I dedicate this dissertation, hoping to convey how important you have been to me.

DEDICATION

to my Mom and Dad,
who have always encouraged and supported me,

I could never express how much you have given me,
or how much I appreciate it.

TABLE OF CONTENTS

TABLE OF CONTENTS - *Continued*

LIST OF FIGURES

LIST OF FIGURES – *Continued*

LIST OF TABLES

ABSTRACT

From the Earth to asteroids, numerous rocky bodies in our solar system are believed to have a metallic core at their center. However, due to the inaccessibility of these cores, fundamental issues, such as the composition of the cores or the processes of core formation and core evolution, are not well known. I have conducted both theoretical and experimental geochemical studies which have improved our understanding of the cores of terrestrial planetary bodies.

The radioactive decay of K is an important planetary heat source, but the distribution of K in terrestrial planetary bodies has been debated. My experimental work, which examined the solubility of K in metal, shows no evidence for K to be an important heat source in metallic cores.

The element pairs of Ag, Pd and Re, Os have been used to date core formation and core evolution events in our solar system. My experimental determination of the partitioning behavior of these important elements can be used to better understand their distribution in iron meteorites, our only samples of planetary cores.

Simple fractional crystallization of a metallic core cannot explain the elemental trends observed within iron meteorite groups. I have developed a crystallization model which suggests slight inhomogeneities and mixing in the molten core were important during core evolution.

As a metallic core crystallizes, liquid immiscibility may be encountered, which could significantly affect the subsequent evolution of the core. My experimental work

suggests the role of liquid immiscibility during the crystallization of a metallic core is significantly smaller than the published phase diagram implies.

These four topics, though each an independent project, together provide insight into the nature of the cores of terrestrial planetary bodies and the processes which affect those cores.

CHAPTER 1

INTRODUCTION

1.1 Cores in our Solar System

The term terrestrial planetary bodies is used to refer to objects which resemble Earth. Like the Earth, a significant portion of a terrestrial planetary body is composed of silicate rocks. Also like the Earth, most terrestrial planetary bodies are believed to have metallic cores at their centers.

Information about the cores of terrestrial planetary bodies is significantly limited due to the inaccessible location of the cores. The majority of the information about the Earth's core comes from seismic studies. By observing how waves are reflected and refracted, one can determine various properties about the material through which the waves are propagating. Using seismology, a core's size, structure, and density can be determined. Information about the state of the core, whether it is solid or liquid, can also be obtained. Although seismic studies could also be used to determine the interior structure of other terrestrial planetary bodies, the majority of information about the cores of other planetary bodies comes from spacecraft missions. By noting the effect that a body's gravity has on the spacecraft, information can be deduced about the distribution of mass within the planetary body. This method has been used to determine the presence of metallic cores in other terrestrial planetary bodies, along with the approximate sizes of these cores.

Though the generation of planetary magnetic fields is not fully understood, the presence, or lack, of an internally-driven magnetic field has also been used to infer properties of the cores of planetary bodies (e.g. Stevenson et al., 1983). The Earth has a magnetic field which is believed to be powered by convection in the outer molten portion of the metallic core. It has been argued that without an actively growing solid inner core, convection, and consequently the magnetic field, would not currently be maintained. In the past, when the planets were hotter, thermal convection could be maintained in a fully molten core and a magnetic field could be produced (Lister and Buffett, 1995; Buffett et al., 1996). However, the interior temperature of a terrestrial planet is believed to no longer be high enough to drive convection by itself. Thus, planetary bodies which are observed to have cores but no magnetic fields are often believed to have cores which are either entirely molten or lack a significant molten portion.

The other information we have about the cores of terrestrial planetary bodies comes from iron meteorites, some of which are believed to be samples of the disrupted metallic cores of asteroid-sized bodies (Scott, 1972). Iron meteorites thus offer a unique opportunity as the only samples we have from any planetary cores. Studies of iron meteorites indicate cores formed in asteroid-sized bodies early in the history of the solar system, ~4.56 billion years ago (Horan et al., 1998). After ~100 million years, all the cores which the iron meteorites represent had completely solidified (Smoliar et al., 1996; Shen et al., 1996). As will be discussed later in this chapter in more detail, iron

meteorites have provided much insight into the composition and evolution of planetary cores.

Figure 1.1 shows the interior structures of the terrestrial planetary bodies in our solar system to scale. Table 1.1 lists the radii of the cores as well as the strength of any detected magnetic fields. References are also listed at the bottom of Table 1.1. The size and structure of the Earth's core is well known from seismology. The inner core is solid with a density consistent with Fe-Ni. The outer core is liquid and requires a composition of Fe and Ni along with ~10 wt% of a light element to explain the inferred density. The light element in the core is debated, with popular choices being S, Si, C, and O (MacDonald and Knopoff, 1958; Murthy and Hall, 1970; Newsom and Sims, 1991; Wood, 1993).

Mariner 10 provided the most precise measurement of Mercury's mass and density and also detected a magnetic field. Models suggest Mercury's core is now almost completely solid, with the thin molten layer maintaining the observed magnetic field. The sizes of the cores of both Venus and Mars have been determined from spacecraft data, and neither of the planets is observed to have a present-day magnetic field. The cores of both planets have thus been suggested to be fully molten. The Martian core is suggested to have a high S-content, which requires a lower temperature to begin crystallizing solid metal. As for Venus, the slightly lower central pressure than the Earth, the slow rotation rate, and a higher interior temperature due to the lack of heat transport from plate tectonics have all been offered as explanations for how a planet so similar to the Earth in size and density can currently have a fully molten core.
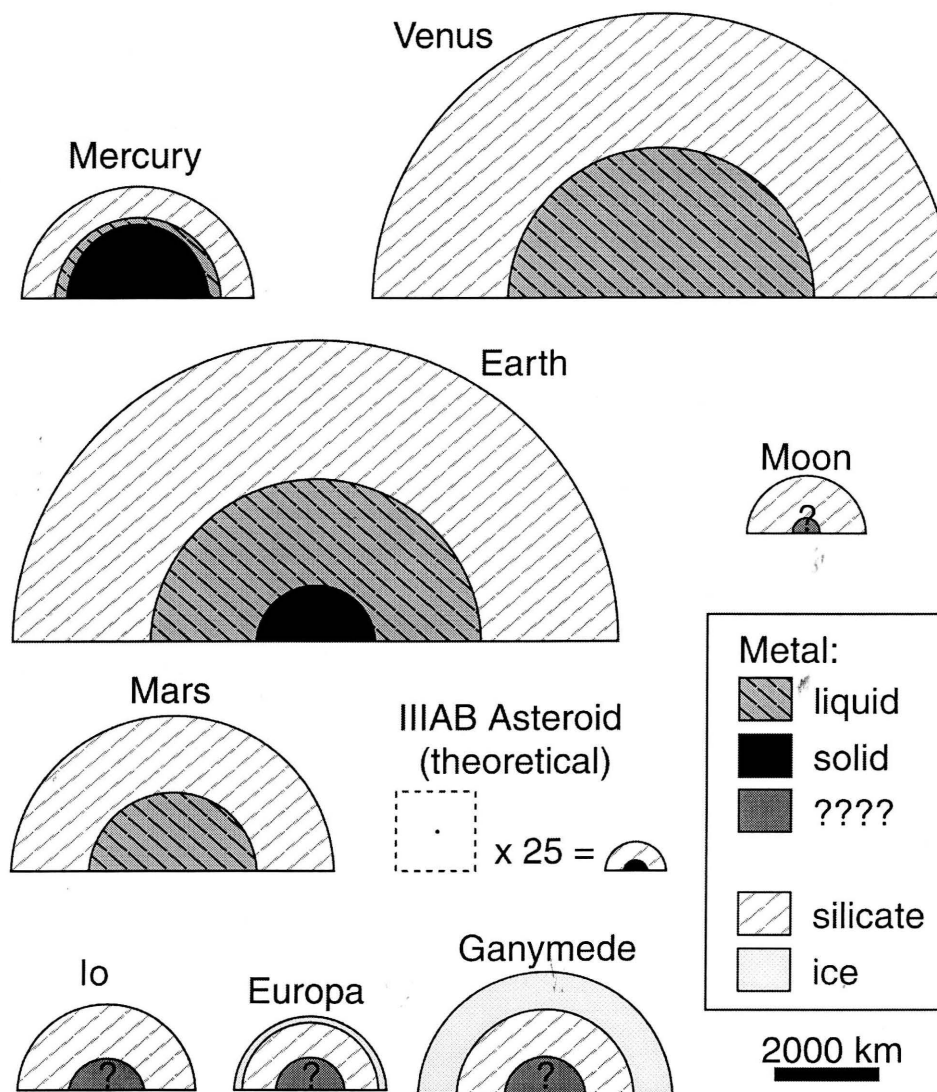
FIG. 1.1. The interior structures of terrestrial planetary bodies in our solar system are shown on the same scale. There is evidence from IIIAB iron meteorites that asteroids as small as 25 km in radius can have metallic cores. The size of the cores of the moons of Jupiter have only been estimated in the last few years, and modeling of the solid or liquid state of these cores has yet to be reported. The existence of a small metallic core in the Moon is only recently proven, and the solid or liquid state of the cores of the terrestrial planets, other than the Earth, are based on model results. Cores that have been thermally modeled are not represented by question marks in this figure, even though the state of their cores is known only from modeling. We have much yet to learn about the cores of terrestrial planetary bodies. Table 1.1 lists the numbers and references on which this figure is based.

TABLE 1.1. Terrestrial planetary bodies in our solar system.

Planetary Body	Radius (km)	Core Radius (km)	Inner Core Radius (km)	Surface Magnetic Field (Gauss)
Earth	6378 [a]	3485 [c]	1250 [c]	0.31 [a]
Venus	6052 [a]	3200 [c]		$\leq 2 \times 10^{-5}$ [a]
Mars	3396 [a]	1780 [c]		$\leq 3 \times 10^{-4}$ [a]
Mercury	2440 [a]	1750 [c]	1500 [c]	3×10^{-3} [a]
Moon	1738 [a]	220 - 450 [d]		$< 3 \times 10^{-3}$ [a]
Io	1821 [a]	660 - 950 [e]		1.3×10^{-2} [f]
Europa	1565 [a]	470 - 940 [g]		$\leq 2.4 \times 10^{-3}$ [h]
Ganymede	2634 [a]	400 - 1300 [i]		7.5×10^{-3} [j]
IIIAB asteroid	25 [b]	10 [b]		

References: (a) Beatty et al. (1999). (b) Rasmussen (1989). (c) Jacobs (1992). (d) Konopliv et al. (1998). (e) Anderson et al. (1996b). (f) Kivelson et al. (1996b). (g) Anderson et al. (1997). (h) Kivelson et al. (1997). (i) Anderson et al. (1996a). (j) Kivelson et al. (1996a).

Recent data about the Moon indicate that a small lunar core does exist with a maximum radius of ~400 km. The lack of much metal in the Moon is consistent with the theory that the Moon was formed from a dust cloud which resulted from a giant impact on the Earth (Cameron, 1986). Though the Moon has no intrinsic magnetic field today, many lunar samples show evidence of cooling in the presence of a magnetic field. As for other moons in the solar system, recently, the Galileo spacecraft has provided some unanticipated information about the moons of Jupiter. Gravity data are consistent with Io, Europa, and Ganymede all having metallic cores. Furthermore, internal magnetic fields have been detected for both Io and Ganymede. Although detailed thermal models have not been conducted, it has been suggested that, though these are small planetary bodies, their cores are still partially molten (Schubert et al., 1996).

Cooling rates determined from the largest iron meteorite group suggest asteroids as small as 25 km in radius may have metallic cores. Many asteroids have been identified which are spectrally consistent with being composed of Fe-Ni metal (Gaffey et al., 1989), and radar observations of a 2 km near-Earth asteroid suggest it has a metallic composition (Ostro et al., 1991). Some stony meteorites have also been interpreted as coming from an asteroid which contained a metallic core, such as the eucrite meteorites which appear to be derived from the 275 km radius asteroid Vesta (Consolmagno and Drake, 1977; Binzel and Xu, 1993).

1.2 Core Formation

Though it has been debated, the terrestrial planets are largely believed to have accreted hot from planetesimals composed of metal and silicate. After accretion, the interior of the planet was warm enough to allow the denser metal to coalesce and sink through the silicates to the center of the planet. The resulting structure of the planet was a central metallic core surrounded by a silicate mantle. Radiometric dating indicates core formation in the Earth concluded 4.45 billion years ago (Oversby and Ringwood, 1971), very early in the history of the solar system.

Most studies aimed at trying to learn about core formation in terrestrial planetary bodies attempt to understand the formation of the Earth's core. While the Earth's core may be inaccessible, we have numerous samples of the Earth's mantle (Morgan et al., 1980; Jagoutz et al., 1979). The segregation of metal and silicate during core formation will affect the composition of both the core and the mantle. The mantle abundance of many siderophile elements, elements which prefer to be in a metallic state, have frequently been used to understand the process of core formation since the concentration of these elements is believed to have been established early in the history of the Earth. Examination of natural samples and experiments suggest the concentration of many siderophile elements in the Earth's mantle is many orders of magnitude higher than would be produced by equilibrium between metal and silicate at low pressures and temperatures (e.g. Ringwood, 1966; Murthy, 1991; Capobianco et al., 1993).

One theory used to explain the abundance of siderophile elements in the Earth's mantle is heterogeneous accretion of the Earth (Wänke, 1981), illustrated in Fig. 1.2. In

the heterogeneous accretion theory, the material from which the Earth is growing becomes more oxidized as accretion proceeds. Initially, core formation proceeded in a manner similar to that suggested by equilibrium calculations. However, as more oxidized material accreted to the Earth, siderophile elements became oxidized and remained in the silicate mantle rather than being segregated to the core. Eventually, the material falling to the Earth was so oxidized, metal was no longer stable, and core formation ceased. This last influx of material to the Earth which was essentially uninvolved in core formation is often referred to as the late veneer.

The step-like pattern in the mantle's siderophile concentrations is often cited as evidence of the addition of material to the mantle by heterogeneous accretion. In the Earth's mantle, most moderately siderophile elements are similarly depleted relative to their primitive abundances; most highly siderophile elements also have similar depletions to each other but are more depleted than the moderately siderophile elements. However, the depletions of the moderately and highly siderophile elements are not as large as equilibrium between metal and silicate would suggest because, according to the heterogeneous accretion theory, the elements were added to the mantle in an oxidation state such that they were not segregated to the core. There are exceptions to the stepped pattern, such as the element Ga, which is moderately siderophile but shows no depletion in the Earth's mantle after volatility corrections are applied (Newsom and Sims, 1991). It has also been argued that the extensive amount
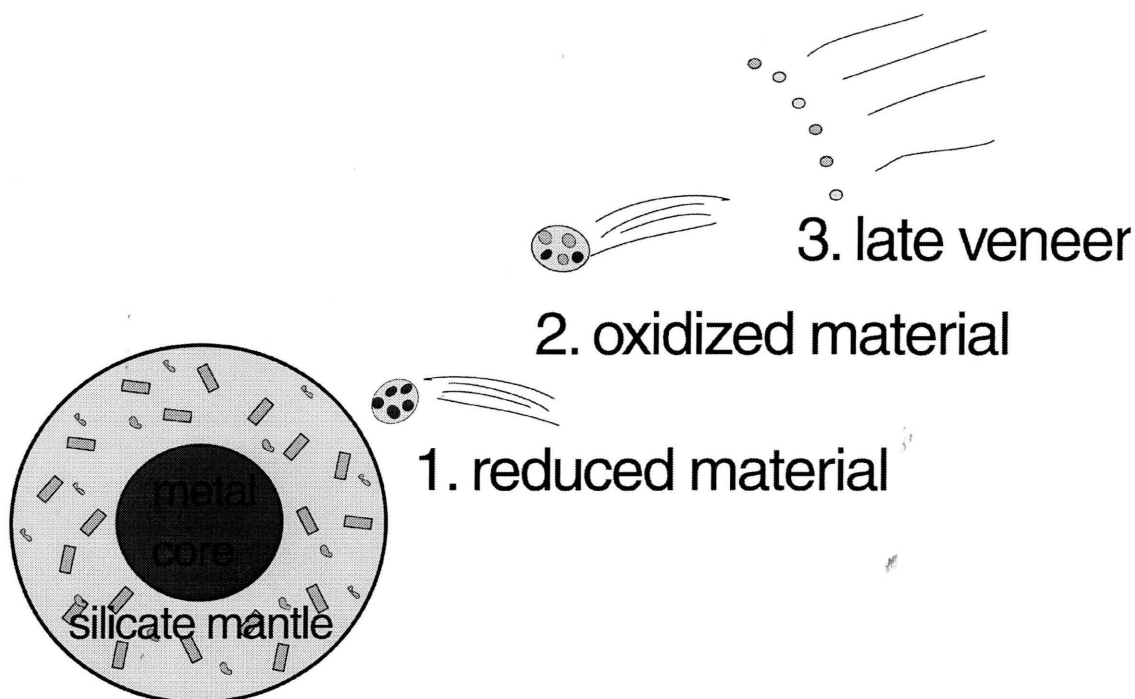
FIG. 1.2. This cartoon illustrates the theory of heterogeneous accretion. In the theory, the material being added to the Earth was not constant over the entire growth of the Earth. The first material added contained metal and silicate, and the metal segregated to the core, carrying with it the siderophile elements. This constituted the majority of the material which was accreted to the Earth. The material added towards the end of the Earth's growth was more oxidized than the initial material, and this caused moderately siderophile elements, which had previously segregated to the core, to be concentrated in the mantle. The final material which accreted to the Earth, referred to as the late veneer, was effectively not involved in core formation, enriching the mantle in all types of siderophile elements.

of mixing required to produce homogeneous mantle samples around the world from an influx of oxidized material is difficult at best (Jones and Drake, 1986).

Data from experiments at near surface conditions cannot account for the Earth's siderophile element pattern, but it has been suggested that equilibrium at a higher pressure and temperature might be able to explain the concentrations (Murthy, 1991). Experimental data have shown that the partitioning of elements between metal and silicate is significantly different at different thermodynamic conditions. Using parameterizations of experimental data and giving consideration to the volatility of each element, the mantle's concentrations of moderately siderophile elements Ni, Co, Mo, W, P, Ga, Cu, and Sn and the highly siderophile element Re can be explained by equilibrium between liquid metal and liquid silicate at a pressure of ~250 kbars and a temperature of ~2200K using an oxygen fugacity and compositions relevant to the early Earth (Li and Agee, 1996; Righter et al., 1997; Righter and Drake, 1997; Righter and Drake, 1999). There are insufficient experimental data to try and explain the abundance of other siderophile elements.

Figure 1.3 shows the core formation scenario suggested by equilibrium between liquid metal and liquid silicate at ~250 kbars. Molten melt coalesces and ponds at the base of a ~1000 km deep magma ocean where it equilibrates with the liquid silicate. Diapirs from the ponded metal then descend through the solid mantle and form a fully molten metallic core. Interestingly, the depth of the magma ocean corresponds roughly to the current day boundary between the upper and lower mantle. A mineral transition marks the boundary between the upper and lower mantle and may also explain how the

upper mantle could be molten while the lower mantle remained solid. This core formation scenario has also been shown to be consistent with our limited information about the Moon, Mars, and the asteroid Vesta (Righter and Drake, 1996).

Experiments conducted at pressures applicable to the Earth's lower mantle suggest that any equilibration between the metal and the solid mantle as the metal descends to the core will influence the observed mantle siderophile abundances (Tschauner et al., 1999). Thus, if the siderophile element pattern of the mantle is already matched well by equilibrium between liquid metal and liquid silicate at the base of a deep magma ocean, the metal diapirs cannot react at all with the solid mantle as they sink. Alternatively, the compositions of the upper and lower mantles are different or the equilibrium core formation scenario has to be revised to include the effects of both the liquid and solid portions of the mantle.

In the past, previous core formation models, which at first also looked promising, have proved to be unsuccessful once they attempted to explain the concentration of more elements in the Earth's mantle (e.g. Jones and Drake, 1986). To better determine the relative roles of the late veneer and metal-silicate equilibrium, more experimental data for more elements are still needed. Thermodynamic conditions can significantly affect how an element will partition between metal and silicate and consequently how the process of core formation will affect the distribution of elements in terrestrial planetary bodies.
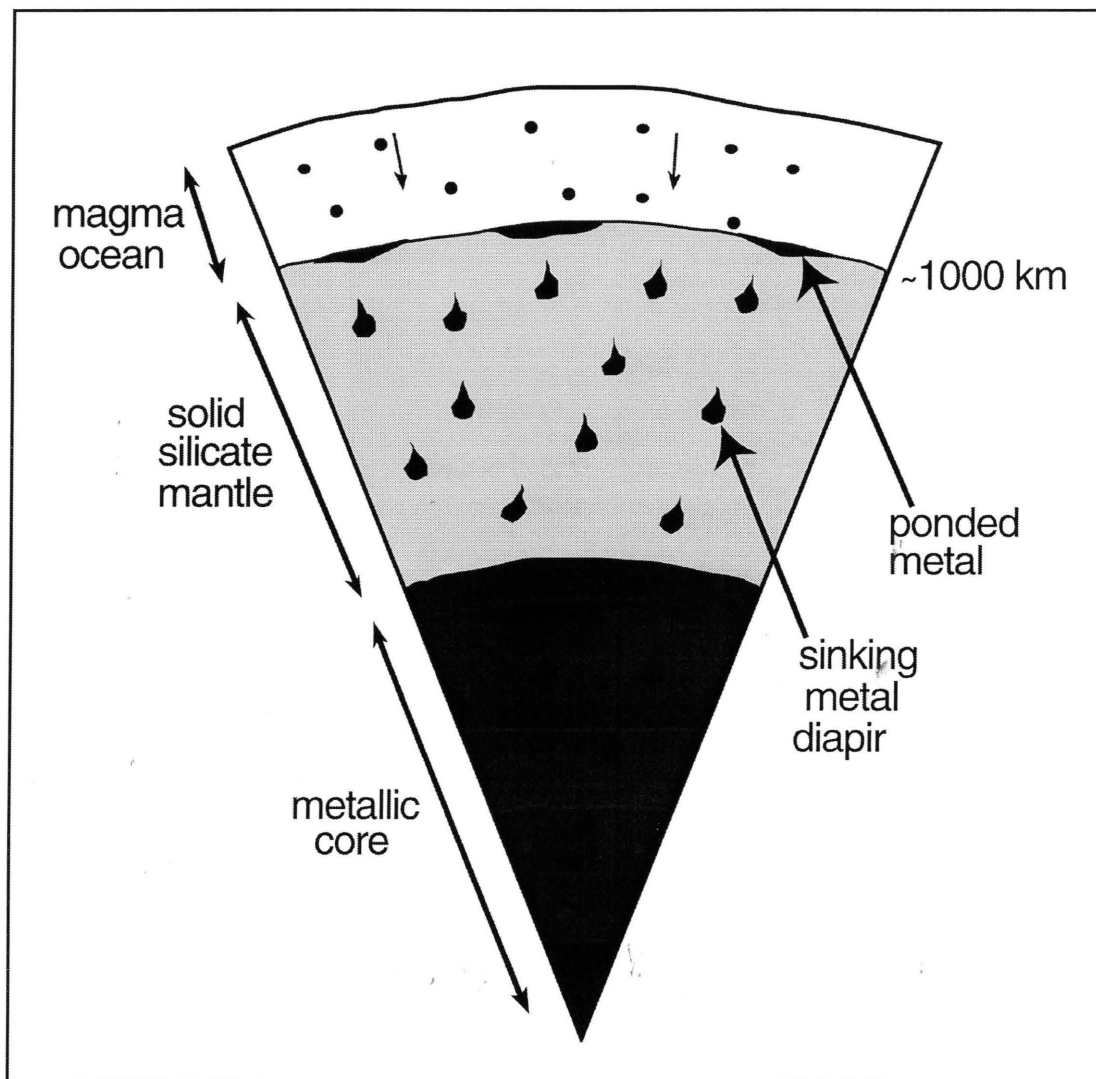
Fig. 1.3. A theory of core formation which involves equilibrium between metal and silicate at a high pressure and temperature is illustrated by this cartoon. In this theory, the upper portion of the Earth is composed of a magma ocean with a depth of ~1000 km. Molten metal easily coalesces and sinks through this liquid portion of the Earth. The metal ponds at the base of the magma ocean, where it equilibrates with the liquid silicate in the magma ocean. Eventually metal diapirs form from the ponded metal and sink through the solid lower mantle to form the core.

1.3 Core Evolution

As discussed in the previous section, a core is believed to be fully molten just after its formation. As the planetary body cools, so does the core. After some time, depending largely on the size of the planetary body, the core will begin to solidify. The Earth's core is currently in this state of its evolution, with the inner core solidifying from the molten outer core. The Earth's core, however, is inaccessible, and consequently, iron meteorites, as our only samples of planetary cores, have provided most of our insight into the evolution of planetary cores.

The majority of iron meteorites are divided into two main classes: the magmatic and non-magmatic groups (Scott and Wasson, 1975). Meteorites from both classes form distinct clusters on element versus element diagrams, but the shapes of the clusters are fundamentally different between the two classes. Figure 1.4 shows two magmatic and two non-magmatic iron meteorite groups on a plot of Ir against Ni. The magmatic iron meteorite groups show strong interelement correlations and define trends on element versus element diagrams which are similar among all the magmatic groups. In contrast, the elemental trends defined by the non-magmatic groups are more diffuse and trend in different directions than the trends of the magmatic groups. In addition, the non-magmatic groups contain abundant chondritic silicates and primordial noble gases, both of which are very rare or absent in magmatic iron meteorites. The presence of silicates with primitive compositions and the retention of gases which can be lost through outgassing suggest that non-magmatic iron meteorites did not experience a prolonged melting event. It has been proposed that non-magmatic iron meteorites represent

numerous impact-generated melt pools which cooled rapidly enough to have incomplete segregation of the melt from the nearby unmelted silicates (Choi et al., 1995).

Magmatic iron meteorites, on the other hand, are believed to be pieces of metallic cores of asteroid-sized bodies (Scott, 1972). Each magmatic group represents the core of a single parent body. The magmatic iron meteorite group with the most members is the IIIAB group, which is composed of nearly 200 meteorites, and is, consequently, well studied. The large number of IIIAB meteorites by itself suggests a large mass of metal in the parent body. Cooling rate data for the IIIAB group also supports a core origin for these meteorites. Due to the high thermal conductivity of Fe-Ni metal, a planetary core is expected to be nearly isothermal, with the entire core cooling at the same rate. Multiple IIIAB iron meteorites, which span the full range of elemental concentrations in the group, yield the same cooling rate (Rasmussen, 1989). The IIIAB cooling rate is consistent with the cooling rate expected for a metallic core of a parent body with a radius of 25 km (Rasmussen, 1989).

As mentioned and shown on Fig. 1.4, magmatic iron meteorites, when plotted by group, all display similar, well-defined trends on element versus element diagrams. The elemental trends are attributed to the solidification of the once molten metallic core; as the core cooled, Fe-Ni metal began to fractionally crystallize which created a range of concentrations for each element in the solid metal (Scott, 1972). The process of fractional crystallization occurs when the metallic liquid and the previously solidified metal do not remain in equilibrium. The lack of equilibrium can arise if the crystallization rate is much faster than the rate of diffusion in the solid metal or if the

solid is physically removed from the liquid after it crystallizes. In either case, once the solid is crystallized, it does not change its composition. Due to mass balance and element conservation considerations, the liquid composition is continually changing during the crystallization process, and consequently, the composition of the crystallizing metal will be different than the previously solidified metal. Thus, the result of fractional crystallization will be the formation of solids with a range of compositions.

Within a single magmatic group, the concentration of an element, such as Ir, can vary by over three orders of magnitude. Fractional crystallization can generate large fractionations in elements, and the elemental partitioning behavior suggested by the fractionations in magmatic iron meteorites is also generally consistent with laboratory partitioning studies (Willis and Goldstein, 1982; Jones and Drake, 1983).

Since the elemental trends observed in magmatic iron meteorite groups appear to be caused by the solidification of a metallic core, understanding these trends provides insights into the method of core evolution. Though the general process of fractional crystallization can explain the large fractionations observed in the trends, understanding the detailed shape of the trends can give information about the specific method of crystallization. Did the cores of asteroid-sized bodies crystallize from the core-mantle boundary inward or did they crystallize outward, as the core of the Earth is doing? Did heterogeneities exist in the molten portion of the core or was the metallic liquid always well mixed? Did the core crystallize in a planar, concentric manner or did large dendritic structures form on the crystallization front? Insights into questions such as
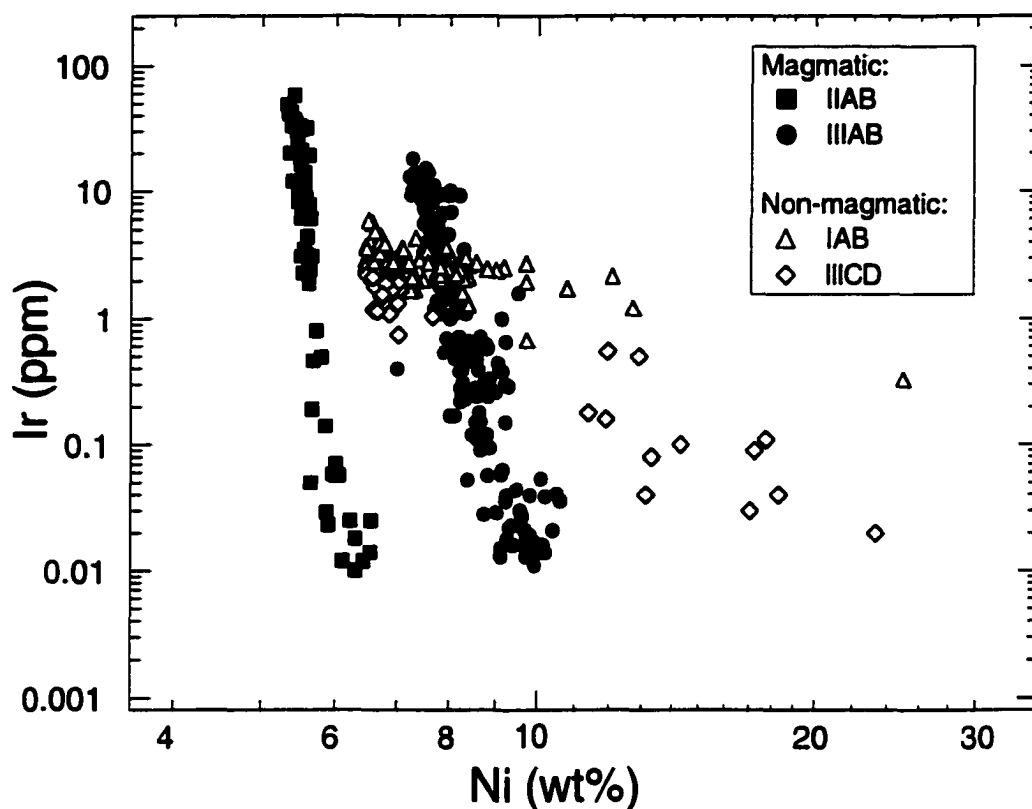
FIG. 1.4. The majority of iron meteorites are divided into two classes, magmatic and non-magmatic. Shown on this figure are two magmatic groups and two non-magmatic groups. The magmatic iron meteorites are believed to be samples of the metallic cores from asteroid-sized bodies. On element versus element diagrams, the magmatic groups form distinct well-defined trends which are similar in shape between the different magmatic groups. Non-magmatic groups exhibit more scattered trends, with two IAB meteorites having a Ni concentration >30wt% and not shown on this diagram. References for the IIIAB meteorite data are given in Table A1 of Haack and Scott (1993). The IIAB meteorite data is from Wasson (1974), Kracher et al. (1980), Malvin et al. (1984), and Wasson et al. (1989). The IAB and IIICD meteorite data is from Choi et al. (1995).

these and others regarding the evolution of planetary cores can be gained by understanding the elemental trends in magmatic iron meteorites.

1.4 Dissertation Outline

As discussed above, detailed theoretical and experimental studies are required to understand core formation and core evolution in terrestrial planetary bodies. These studies include both performing laboratory experiments and interpreting meteorite data. In this dissertation, I present my research which has involved the experimental determination of the partitioning of trace elements and the modeling of iron meteorite crystallization trends.

I begin in Chapter 2 by defining a partition coefficient, illustrating the need for geochemical experiments, and introducing the different experimental and analytical methods I have used in my research. The next four chapters, Chapters 3-6, each detail a different study which has implications for the cores of terrestrial planetary bodies. Chapter 3 investigates the role of radioactive heating from K in planetary cores. Potassium is an important planetary heat source, and to understand the distribution of K between the core and mantle, I have examined experimentally the solubility of K in metal. Chapter 4 examines the partitioning of element pairs used as chronometers. Both the pair of Ag and Pd and the pair of Re and Os have been used to date events which occurred early in the solar system, and I have conducted experiments to better understand the partitioning of these useful elements during core crystallization. Chapter 5 examines the effect that mixing in the molten core may have had on the partitioning of

elements during crystallization of the core. Simple fractional crystallization of a metallic core can not explain the observed elemental trends in magmatic iron meteorites, and I have developed a mixing model which is able to better reproduce the observed meteorite data. Chapter 6 investigates the role of liquid immiscibility during core crystallization. The onset of liquid immiscibility could significantly affect the subsequent evolution of a core, and I have determined the location of the liquid immiscibility field at conditions relevant to terrestrial planetary cores. The final chapter, Chapter 7, summarizes the major conclusions of these studies and discusses how the results have added to our knowledge of the cores of terrestrial planetary bodies and the processes which affect them.

CHAPTER 2

USING EXPERIMENTAL GEOCHEMISTRY TO STUDY CORES

2.1 Understanding Trace Element Partitioning Behavior

The distribution of trace elements in a planetary body will be affected by the planetary processes which have occurred. Processes such as core formation and core evolution, which were just discussed in Chapter 1, cause elements to partition between different portions of the planetary body. Understanding the distribution of trace elements can be used to interpret how these processes have acted and to deduce the composition of planetary cores.

However, it is first necessary to understand the partitioning behavior of the elements of interest. The partitioning behavior of elements is known to be dependent on a number of thermodynamic variables. Pressure, temperature, oxygen fugacity, and silicate and metallic composition can have a large effect on the resulting partitioning behavior. Systematic geochemical experiments which investigate the effect of a single variable while holding the other thermodynamic conditions constant are used to determine the partitioning behavior.

The quantity normally measured in the experiments is the partition coefficient. The partition coefficient is simply the ratio of the concentrations of an element between two phases. For example, during core formation, elements are believed to have partitioned between the silicate mantle and the metallic core. Consequently, experiments which are

frequently applied to understanding core formation involve metal/silicate partition coefficients, defined as:

$$D_E(met/sil) = \frac{wt\%E(metal)}{wt\%E(silicate)}$$

Eq. 2.1

where E is the element of interest and $D(met/sil)$ is the metal silicate partition coefficient. Whether the metal and silicate are solid or liquid can affect the partitioning behavior, and it is necessary to specify the state of each phase when defining a metal/silicate partition coefficient. During the solidification of a metallic core, elements will partition between the solid crystallizing metal and the remaining molten metal. The partition coefficient used to understand this process is given by:

$$D_E(sol.met/liq.met) = \frac{wt\%E(solidmetal)}{wt\%E(liquidmetal)}$$

Eq. 2.2

where E is the element of interest and $D(sol.met/liq.met)$ is the solid metal/liquid metal partition coefficient. Both of these partition coefficients have been introduced as the ratio of concentrations in wt%. However, molar partition coefficients which ratio the atomic concentrations are also used. In this work I use the variable k to denote a molar partition coefficient and the variable D to represent a weight partition coefficient.

Systematic experiments have shown the partition coefficients of elements can vary by orders of magnitude with varying thermodynamic conditions. Also, different

elements can exhibit very different partitioning behavior. As one example, Fig. 2.1 plots

the experimentally determined solid metal/liquid metal partition coefficients for Ir, Ge,

and Ag, three elements which exhibit very different partitioning behavior as a function

of the S concentration in the metallic liquid (Willis and Goldstein, 1982; Jones and

Drake, 1983; Chabot and Drake, 1997). As shown in Fig. 2.1, D(Ir) increases by over

two orders of magnitude from the S-free system to the Fe-FeS eutectic composition

while D(Ag) shows the opposite behavior, decreasing as the S-content of the metallic

liquid increases. The partition coefficient for Ge exhibits the interesting behavior of

changing from incompatible (D<1) to compatible (D>1) in solid metal with increasing

S-content of the metallic liquid. This just illustrates the necessity of systematic

geochemical experiments since the manner in which the partitioning behavior is

affected by thermodynamic variables is significant but not the same for all the elements.

In the next sections, I introduce the three experimental methods I have used to

conduct partitioning experiments. The last section of this chapter describes the use of

the electron microprobe for analysis of my experiments.

2.2 Vertical Tube Furnace Experiments

A vertical tube furnace was used to conduct experiments at atmospheric pressure

and temperatures between 1050–1455°C. Because of the 1 bar pressure limitation of

these experiments, the experimental results are most applicable to small planetary

bodies rather than large planets. Thus, the experiments I conducted in the vertical tube
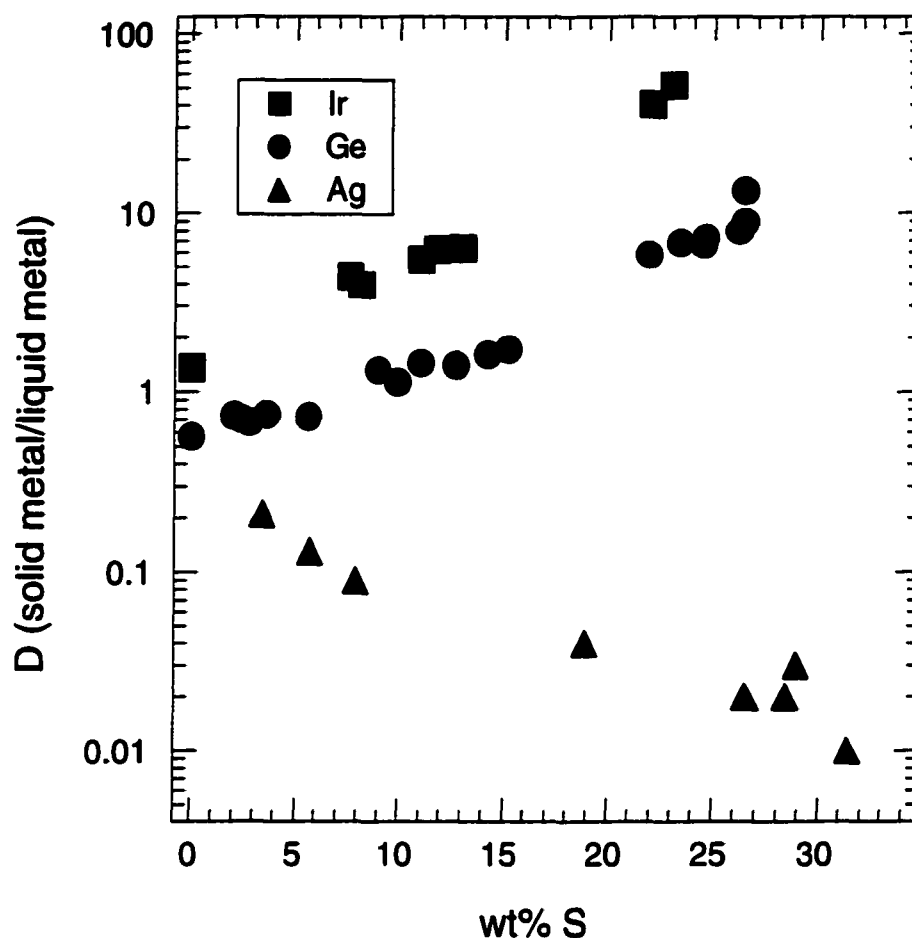
FIG. 2.1. The partitioning behavior of elements can be significantly affected by thermodynamic variables, such as pressure, temperature, oxygen fugacity, and composition. To illustrate this point, the experimentally determined solid metal/liquid metal partition coefficients (D) are shown for Ir, Ge, and Ag as a function of the S-content of the metallic liquid (Willis and Goldstein, 1982; Jones and Drake, 1983; Chabot and Drake, 1997). The effect of S on the solid metal/liquid metal partitioning behavior can be quite different for different elements, illustrating the need for experimental data to understand the partitioning behavior of each element.

furnace were solid metal/liquid metal partitioning experiments, which were used to understand magmatic iron meteorites and the evolution of planetary cores.

Figure 2.2 shows the general experimental assembly. The starting mixture, which was usually some combination of Fe, FeS, P, and Ni doped with the trace element of interest at ~wt% level, was contained in an alumina crucible and inserted into a high-purity silica glass tube. The crucible rested on a "cushion" of silica wool to help keep the crucible from moving during the remaining preparation of the assembly. After a solid silica glass rod was placed on top of the crucible, a second, smaller diameter silica tube was attached to the top of the original tube by melting the two tubes together and forming a ring seal. The smaller diameter tube was attached to a vacuum, which then evacuated the assembly. Once evacuated, the assembly was sealed by melting the smaller diameter tube shut. The sealed tube was then formed into a curved shape to facilitate hanging in the furnace. A ring seal was also created between the wider silica glass tube and the solid silica glass rod, which minimized the volume containing the sample without requiring any direct heating near the crucible. The assembly was then lowered into the vertical tube furnace. The furnace was heated to the temperature of interest and held at that temperature for a duration long enough for the sample to achieve equilibrium. Consequently, run durations varied from many weeks to just a few hours, depending inversely on the temperature. To complete the experiment, samples were quenched by removing the silica tube from the furnace and immersing the tube in water, preserving the compositions of the equilibrium phases that existed at the run
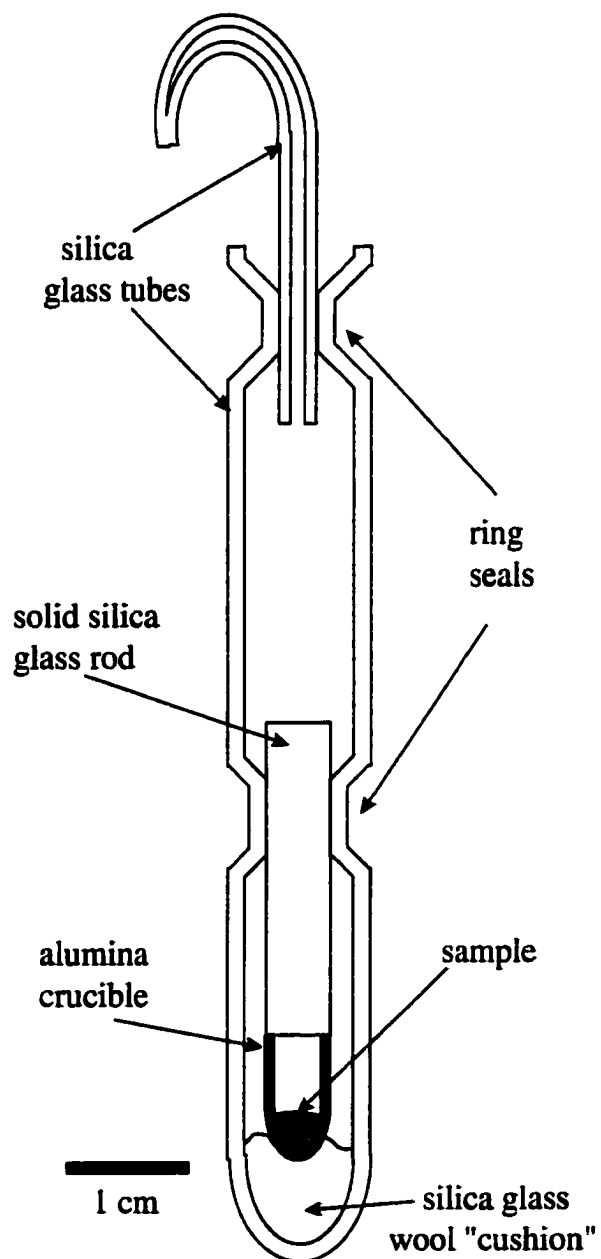
FIG. 2.2. The assembly used to perform experiments in a vertical tube furnace is illustrated. The sample is contained in an alumina crucible within an evacuated silica tube. The entire assembly is hung in the furnace.

conditions. After quenching, the assembly was broken open and the crucible was mounted in epoxy in preparation for polishing.

2.3 Piston Cylinder Experiments

Using a piston cylinder apparatus, experiments were conducted at a temperature of 1900°C and a pressure of 15 kbars. Along with the ability to run at a higher pressure and temperature than experiments conducted in a vertical tube furnace, the piston cylinder assembly is still reliable and relatively easy to create. For these reasons, experiments investigating the effects of composition on elemental partitioning between metal and silicate were conducted in the piston cylinder.

Figure 2.3 shows the basic assembly used for the piston cylinder experiments. A thermocouple is created by linking a W_5Re wire with a $W_{26}Re$ wire at the top of a thin alumina tube. The insulated thermocouple is then inserted through the support block and base plug, as shown in Fig. 2.3. An insulator is placed atop the support block so the only electrical path will be through the furnace of the experiment. A thin alumina disk is situated between the sample capsule and the thermocouple; this serves to protect the thermocouple from being damaged during the run but still allows the sample to be located close to the spot where the temperature is being monitored. Crushable MgO surrounds the capsule and the insulated thermocouple wires. For my experiments, capsules were fabricated out of alumina or graphite. A furnace, which is composed of a graphite tube covered by a graphite disk, sits on top of the base plug and encloses the capsule and surrounding MgO. A tube of $BaCO_3$ is placed around the graphite furnace

crushable MgO

capsule

alumina disk

alumina thermocouple
insulator

base plug support
block insulator

Pb foil

BaCO$_3$ cell

graphite furnace

W$_5$Re-W$_{26}$Re thermocouple

base plug insulator
(pyrex)

base plug

base plug support
block

Teflon insulator

2 cm
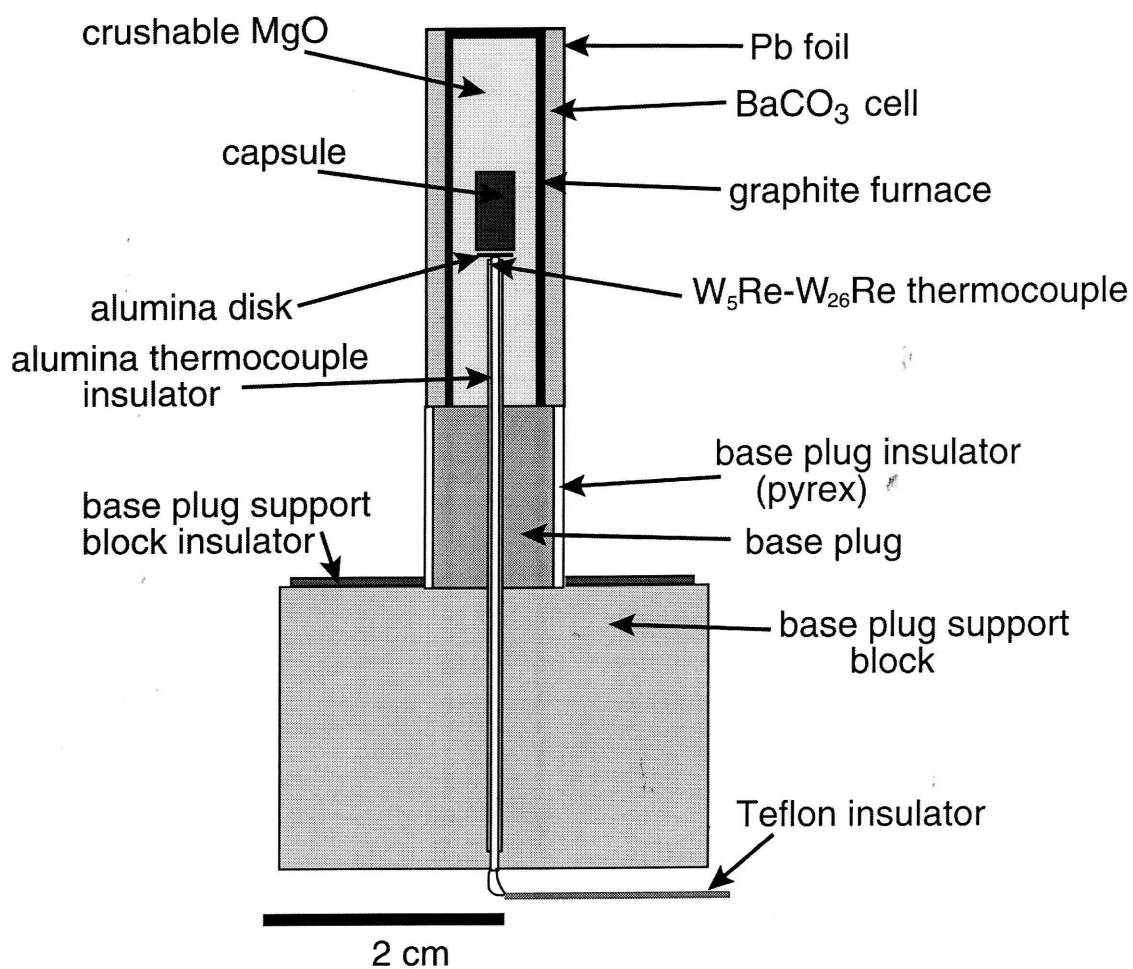
FIG. 2.3. The assembly used to conducted experiments in a piston cylinder apparatus is shown. In my experiments, the sample was contained in either a capsule made of alumina or graphite.

and serves as the pressure medium for the experiment. A thin layer of Pb foil is wrapped around the outside of the $BaCO_3$ to provide lubrication while the experiment is being pressurized.

Experiments were quickly brought to the pressure of interest and then heated for ~1 hour before reaching the desired temperature. Run durations varied from minutes to hours, depending on temperature. Experiments were quenched by abruptly shutting off the power. Even at the highest temperatures, after 20 seconds, the temperature had dropped to below 500°C. It was necessary during the quench to manually adjust the pressure to keep the run as isobaric as possible.

2.4 Multi-Anvil Experiments

With its pressure capabilities, the multi-anvil offers the opportunity to conduct experiments which are relevant to larger planetary bodies. However, the procedure for conducting experiments in the multi-anvil, unlike in the vertical tube furnace or the piston cylinder, is still being developed in our laboratory. Using the multi-anvil, I have conducted a number of exploratory metal/silicate partitioning experiments at temperatures ranging from 1400-1900°C. Though the multi-anvil is capable of achieving a maximum pressure of ~250 kbars, my experiments were conducted between 45-80 kbars.

Figure 2.4 illustrates a typical sample assembly. The multi-anvil uses eight W-C cubes to compress the assembly, and consequently, the pressure medium is in the shape of an octahedron. I used octahedrons which were cast out of predominantly a mixture of
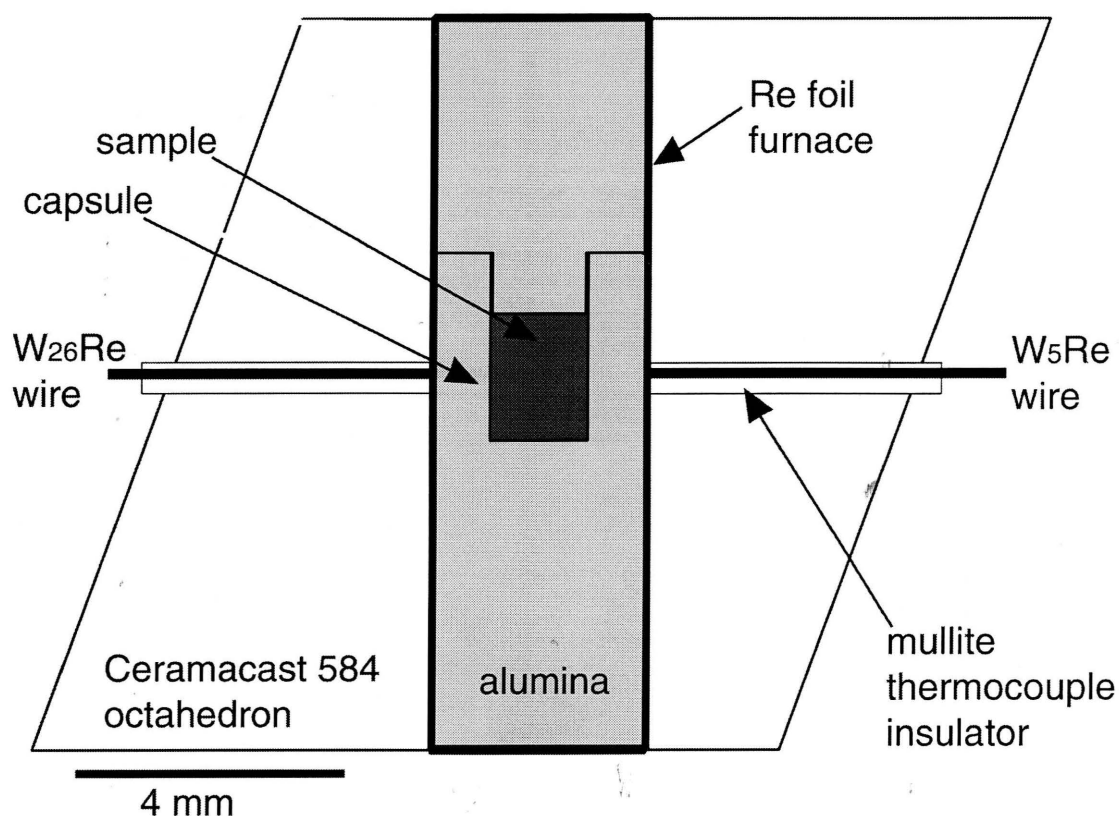
FIG. 2.4. The experimental assembly used for multi-anvil runs is illustrated. Though a furnace fabricated from Re foil is shown, both graphite and Re furnaces were used in my experiments. The materials located within the furnace also varied depending on the details of each experiment. This figure shows the simplest assembly I used, where the experimental sample is contained within an alumina capsule.

MgO and Al_2O_3. Two holes are drilled in the octahedron. One hole is ~3mm in diameter and contains the furnace and sample. The other hole, which is much smaller and perpendicular to the first, allows the thermocouple to be passed through the octahedron and positioned near the middle of the furnace, where the sample will be located. Like the piston cylinder assembly, a thermocouple is created by linking a W_5Re wire with a $W_{26}Re$ wire. The portions of the wires which pass through the octahedron are protected by mullite tubes. In some of the experiments and as shown in Fig. 2.4, the furnace is made out of Re foil. A rectangle of Re foil is formed into a tube, with foil left at either end to be folded to form a hollow cylinder of Re foil. In other experiments, a graphite furnace was used, as is done in the piston cylinder experiments.

Once the thermocouple and furnace are in place, the material inside the furnace varies depending on the experimental sample. The simplest experiments I conducted are shown in Fig. 2.4. A capsule and lid are machined out of an alumina rod. The capsule is designed so the experimental sample remains in the hotspot in the middle of the furnace. This sample configuration worked well for experiments run at 1700°C and lower. However, in experiments at higher temperatures, the experiment would suddenly lose power and the temperature would drop. Examining these failed experiments showed that the Re furnace had melted causing the furnace to become inoperative. Although the capsules showed no leaks, it seems likely that the sample material migrated to contaminate the Re furnace and caused it to melt. However, I did successfully conduct multi-anvil experiments at 1900°C by using a graphite capsule. With the graphite capsule, it was necessary to isolate the capsule from the furnace. In

the experiments with graphite capsules, a thin tube of magnesia or alumina is used to line the inside of the furnace. A complication encountered by using graphite, either for the capsule or for the furnace, is the C phase transition which transforms graphite into diamond. Using my usual preparation techniques, I was unable to cut and polish the experiments in the graphite/diamond capsules due to the hardness of the diamond phase. At 1900°C, this limits experiments to a maximum pressure of ~75 kbars. Creating assemblies with capsules machined out of MgO or using a denser alumina lining between the furnace and the capsule for all the experiments may allow me to conduct future experiments at higher pressures and temperatures.

Once in the multi-anvil, the sample was slowly pressurized, usually overnight. After achieving the desired pressure, the sample was heated for 25-45 minutes until the set point temperature was reached. The run duration depended on the temperature, varying from hours to minutes. The experiment was quenched by abruptly shutting of the power used to heat the sample. The experiment was depressurized slowly over many hours, and the entire octahedron was then mounted in epoxy.

2.5 Electron Microprobe Analysis

All my experiments were analyzed with an electron microprobe. In the microprobe, the experimental sample is bombarded with a beam of electrons, which excites electrons from the inner shells of the atoms of the sample. When the inner shells are refilled, the transition of the electrons between different energy levels produces X-rays which are characteristic of the elements undergoing the transitions. Spectrometers which use a

crystal to disperse the emitted X-rays, much like a prism, are able to resolve the different wavelengths of the X-ray lines from different elements. By scanning the spectrometers over a range of wavelengths, an X-ray spectrum is generated. A qualitative analysis of the composition of the sample can be obtained by identifying which X-ray lines correspond to which elements. A quantitative measure of the concentration of each element can be made by comparing the intensity of a line to a standard of a known composition.

In preparation for microprobe analysis, the sample, which is mounted in epoxy, is sliced in half. Often if a sample is fragile, it is then embedded with a layer of epoxy on the newly cut surface. Polishing of the sample is done with diamond paste. Figure 2.5a shows a typical vertical tube furnace experiment after being polished. For microprobe analysis, it is necessary for the surface of the sample to create a path for the electrical current in the electron beam. Consequently, a layer of carbon ~20 nm thick is coated on the top of the polished surface, making the surface conductive without significantly interfering with the X-rays generated.

Once in the microprobe, the sample can be viewed as a back-scattered electron (BSE) image. Figure 2.5b, shown on the same scale as Fig. 2.5a, shows a BSE image of a typical multi-anvil experiment. The electron microprobe beam can be focussed to a diameter of ~1 μm, allowing analysis of the different phases present in the samples. However, complications in the measurements can arise. Depending on the beam conditions and the density of the sample, the electron beam can penetrate ~0.3-5.0 μm beneath the surface of the sample. If a different phase is present just below the phase

being measured, X-rays may be generated from both phases, affecting the resulting measurement. Secondary fluorescence effects, discussed in detail in Chapter 3, may also compromise measurements. Silicate liquids which quenched to glasses and contain Na and K require a defocused beam to avoid migration of these elements away from the area of the sample being analyzed. My experiments also commonly contained a metallic liquid phase with a dendritic texture, as shown in Fig. 2.5c. The metallic liquid, though it was a single phase at run conditions, formed multiple phases during the quenching process. The resulting quenched metallic liquid is composed of Fe dendrites surrounded by interstitial material which is enriched in any light elements, such as C, P, and S. Analysis of the bulk composition of a metallic liquid with a dendritic texture was done by using a 10 μm raster analysis, discussed in more detail in Chapter 4.

For each phase, multiple microprobe measurements were made and averaged. The error of homogenous phases was computed as twice the standard deviation of the multiple microprobe analyses. For heterogeneous phases, such as those with dendritic textures, the variation between two microprobe measurements reflects the heterogeneity of the phase, not how accurately the bulk composition can be determined. Consequently, for these phases, twice the standard deviation of the mean was used as the error.
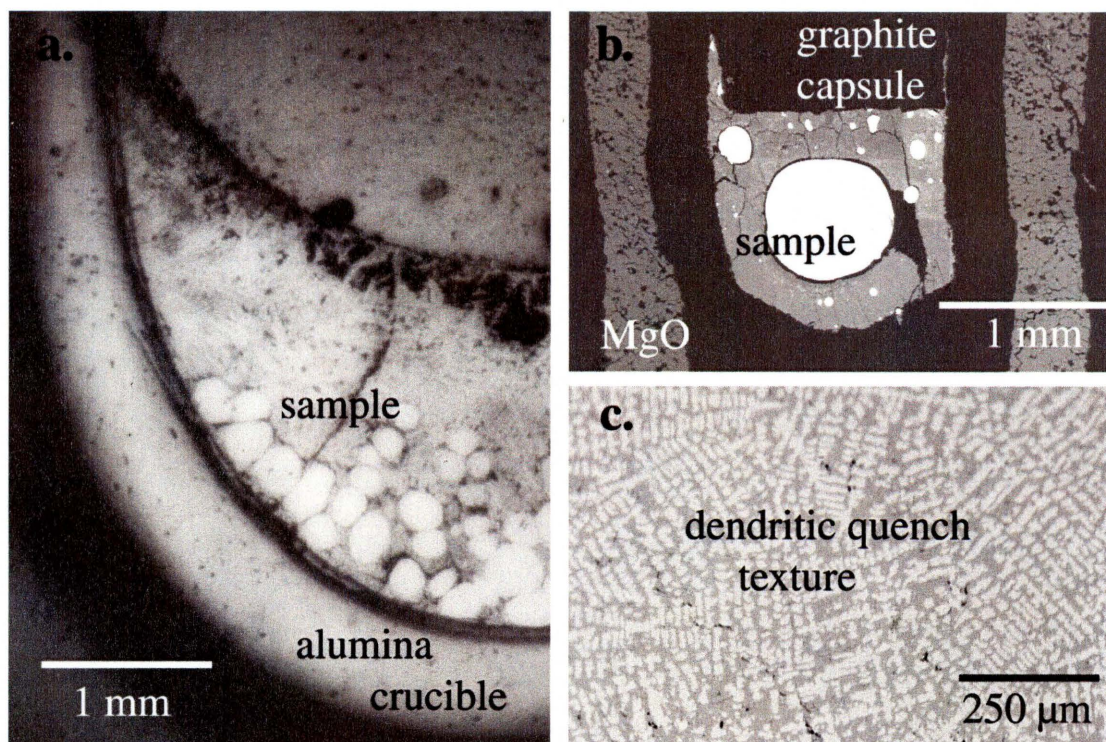
FIG. 2.5. (a) A photograph of a typical run product from a vertical tube furnace experiment is shown. This sample has been cut and polished. The two phases of solid metal and liquid metal are clearly identifiable in the sample. **(b)** A back scattered electron (BSE) image of a multi-anvil experiment was generated by the electron microprobe. Note that (a) and (b) have the same scale bar. Piston cylinder experiments produce a run product similar in size to that shown in (b). Experiments conducted above atmospheric pressure in the piston cylinder or multi-anvil have much smaller sample sizes. To generate the pressure in the experiments, the force is focussed to a small area, while experiments conducted at atmospheric pressure in the vertical tube furnace have no such limitations. **(c)** In all of the types of experiments, the metallic liquid did not quench to a single phase. Instead, a dendritic texture of Fe dendrites surrounded by an interstitial phase enriched in light elements, such as C, P, or S, was formed.

CHAPTER 3

RADIOACTIVE HEATING FROM POTASSIUM IN CORES

To determine the role of radioactive heating as an energy source in planetary cores, the solubility of K in metal has been examined experimentally. Two sets of systematic experiments were conducted at 15 kbars and 1900°C which investigated the effects of metallic and silicate composition on K partitioning between Fe alloys and silicate melts. Experiments indicate S increases the solubility of K in metal, but the presence of C in the metallic liquid, unlike S, does not increase K solubility in metal to a level detectable with the electron microprobe. The silicate composition significantly affects the solubility of K in S-rich metal, with the metal/silicate partition coefficient for K increasing by nearly two orders of magnitude with increasing depolymerization of the silicate melt.

Using an appropriate silicate composition for the early, differentiating Earth and assuming S is a significant light element in the core, the metal/silicate partition coefficient for K is $6*10^{-3}$ at 15 kbars and 1900°C. Such a partitioning value, if representative of the behavior of K at core formation conditions, suggests the presence of less than 1 ppm K in the Earth's core with a present day heat generation of 10^{10} W, which is 2-3 orders of magnitude lower than estimates of the power necessary to drive the Earth's geodynamo. Other thermodynamic variables may also affect the solubility of K in metal, but exploratory experiments, conducted at a variety of pressures and temperatures, have shown no increase in the solubility of K in metal.

3.1 Motivation

The decay of K has long been considered an important heat source for terrestrial planets. Generally, though, it is not considered a significant heat source for planetary cores, due to the tendency of K to form oxides and silicates and thus have a low solubility in metals. So it follows that K would be concentrated in the silicate mantle and excluded from the metallic core during a core formation event.

However, the partition coefficients of elements are known to be dependent on a number of thermodynamic variables. Pressure, temperature, oxygen fugacity, and silicate and metallic compositions can have a large effect on the resulting partitioning behavior. If the specific conditions of core formation did result in an increased solubility of K in the metallic core, this would have implications for the thermal history, geodynamo, and mantle dynamics of that planetary body. According to estimates of the heat source necessary in the Earth's core to maintain the observed magnetic field (Gubbins et al., 1979), ~1000 ppm K in the core could supply enough energy by itself, without any other radioactive heat sources such as U and Th, to drive convection and power the geomagnetic dynamo.

The role of radioactive heating in planetary cores is not a new question (Hall and Murthy, 1971; Lewis, 1971). Murrell and Burnett (1986) summarized the early metal/silicate experimental partitioning studies (Goettel, 1972; Oversby and Ringwood, 1972; Goettel and Lewis, 1973; Oversby and Ringwood, 1973; Goettel, 1976; Ganguly and Kennedy, 1977), the majority of which were conducted at low pressures. Upon

trying, Murrell and Burnett (1986) were unable to reproduce many of these earlier results and concluded that the weight ratio metal/silicate partition coefficient for K,

$$D_K = \frac{wt\%K(met.)}{wt\%K(sil.)}$$ Eq. 3.1

at 15 kbars and 1450°C was 0.0027, considerably lower than earlier studies had suggested. Since the work of Murrell and Burnett (1986), a handful of experiments have been conducted. Ito et al. (1993) reported an experiment at 260 kbars and 2600°C with a higher D_K, suggesting higher pressures and temperatures might increase the solubility of K in metal. However, the metal phases analyzed with the electron microprobe were less than 10 μm in diameter. My experience, presented in detail in the analytical section of this chapter, suggests such a measurement is compromised by secondary fluorescence effects from the neighboring K-rich silicate. Ohtani et al. (1992) and Ohtani et al. (1995) reported results from six experiments which contained numerous tracers, among which was K. The conditions varied between 1500-2600°C and 40–70 kbars, and the measured D_K ranged from the value of Murrell and Burnett (1986) to two orders of magnitude higher. In the papers, 10 μm is shown to be the typical metallic size, but the analytical details are not discussed, nor are any possible reasons for the large observed variation in D_K. Also, the six experiments are run at isolated and changing conditions, making interpretation difficult. The results of experiments at 200 kbars and 2500°C have also been reported (Ohtani and Yurimoto, 1996; Ohtani et al., 1997), but the errors

associated with the K measurements are so large as to make meaningful determinations of D_K impossible.

Theoretical studies and different types of experiments have also debated the solubility of K in metal and the effects of thermodynamic variables such as pressure. Bukowinski (1976), by theoretical considerations of the equation of state, concluded K could behave like a transition metal at pressures as low as 500 kbars and suggested enough K might be contained in the outer core to power the Earth's geodynamo. Similarly, Liu (1986) concluded that the compressible nature of K at high pressures could permit K partitioning into the core. Somerville and Ahrens (1980) conducted shock experiments of $KFeS_2$ and, upon applying the results to thermodynamic equations, came to the opposite conclusion, commenting that especially in the presence of a silicate mantle, partitioning even trace amounts of K into the core was unlikely. Using molecular orbital calculations, Sherman (1990) concluded K cannot alloy with metallic iron and does not have an enhanced affinity for S at higher pressures applicable to planetary cores. However, with a laser heated diamond anvil cell and starting with elemental K and Ni, Parker et al. (1996) reported forming K and Ni compounds at 310 kbars and 2500 K.

I have undertaken a systematic experimental study to understand the solubility of K in metal. Because of the significant consequences radioactive heating as an energy source in planetary cores could have, it is of interest to isolate and understand the effects of the relevant thermodynamic variables.

3.2 Experimental Method

Two sets of systematic experiments were conducted (Chabot and Drake, 1999c). The first set varied the S-content of the metallic liquid and is listed in Table 3.1. The second set is listed in Table 3.2 and consists of experiments run with different silicate compositions. Exploratory experiments (Chabot and Drake, 1998) were also conducted at a variety of pressures and temperatures, and the preliminary results of these experiments are listed in Table 3.3.

3.2.1. Set 1: Varying S-Content

For the first set of experiments, due to concerns over low K solubilties and detection limits, it was desired to have a high activity of K in the sample. Consequently a K-rich starting silicate composition was used. For each experiment, ground natural K-feldspar was mixed in approximately a 1:1 ratio with an Fe, FeS metallic mixture. The Fe, FeS metallic mixture was different for each experiment to vary the resulting metallic composition in the run product. All the experiments were contained in alumina capsules.

Experiments were conducted in the piston cylinder apparatus and held at 15 kbars and 1900°C for durations of at least 40 minutes before the power was abruptly shut off, quenching the run. Care was taken to keep the quench as isobaric as possible by manually adjusting the pressure during the quenching process. After 20 seconds, the temperature had dropped to 500°C, and no evidence was seen for temperature gradients at run conditions or during quenching.
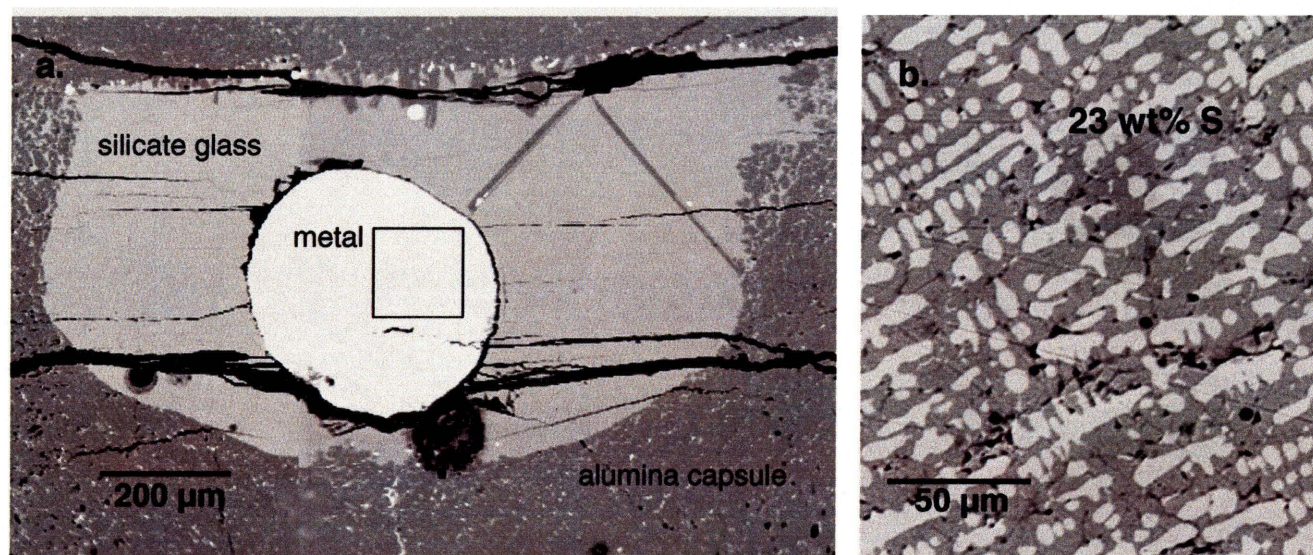
FIG. 3.1. BSE images of run 13, an experiment which examined the effect of S on K solubility in metal, are shown. **(a)** The experiment is contained in an alumina capsule, and the silicate liquid quenched to a homogeneous glass. The boxed region is enlarged in **(b)**. Unlike the silicate phase, the metallic phase, due to the presence of S, did not quench to a single phase but rather formed Fe dendrites surrounded by FeS interstitial material.

TABLE 3.1. Set 1: Examining the effect of S.

Run:	14	25	11	24	13
Duration (min.)	40	60	40	150	40
Metal					
Fe (wt%)	99.9 ±0.6	97.3 ±0.3	88.3 ±0.5	80.8 ±0.5	76.7 ±1.4
S (wt%)	0	2.3 ±0.2	11.3 ±0.4	18.9 ±0.5	22.9 ±1.3
K (ppm)	≤ 10	20 ±8	50 ±20	40 ±16	70 ±28
Silicate					
Si (wt%)	23.1 ±0.2	15.6 ±0.5	20.0 ±0.5	18.1 ±0.3	20.1 ±0.3
Al (wt%)	16.6 ±0.1	21.7 ±0.7	17.1 ±0.8	19.5 ±0.5	18.4 ±0.3
Fe (wt%)	4.9 ±0.1	6.8 ±1.0	10.0 ±0.5	7.5 ±0.4	6.4 ±0.3
Na (wt%)	2.6 ±0.1	5.5 ±0.3	2.2 ±0.1	3.6 ±0.2	3.2 ±0.1
K (wt%)	8.0 ±0.2	6.7 ±0.2	6.6 ±0.2	7.2 ±0.2	7.4 ±0.2
S (100*wt%)	0	8 ±1.6	9 ±1	13 ±1.8	13 ±1.4
Calculated					
D_K (*10^{-3})	< 0.13	0.3 ±0.12	0.8 ±0.3	0.6 ±0.2	0.9 ±0.4
D_S	0	30 ±6	130 ±15	150 ±20	180 ±20
log fO_2 - logIW	-2.4	-2.0	-1.6	-1.7	-1.8

Reported errors are ±2σ. Aside from K and S, for which special analytical procedures were used, concentrations below 0.2 wt% are not reported.

The resulting run product was mounted in epoxy and sliced in half. The exposed surface was ground down and polished without the use of water, due to the comment by Murrell and Burnett (1986) that K-sulfides are water soluble. The silicate phase quenched to a homogeneous glass while the metallic phase formed Fe dendrites surrounded by FeS interstitial material. Figure 3.1 shows BSE images of a typical run product for this first set of experiments.

3.2.2. Set 2: Varying Silicate Composition

The starting compositions in the second set of experiments consisted of K-feldspar, two different K-rich basalts (Mas-49, Mas-4a from Carmichael et al., 1996), Allende (Jarosewich, 1990), a mantle peridotite (KLB-1 from Takahashi, 1986), and mixtures of these natural materials, doped with K-carbonate when necessary to keep K concentrations at levels detectable with the electron microprobe. For each experiment, the silicate was mixed in approximately a 1:1 ratio with an Fe, FeS metallic mixture and contained in a graphite capsule. A graphite capsule, unlike an alumina capsule, does not affect the final silicate composition by reacting with the silicate melt at run conditions. All experiments were conducted in the piston cylinder and held at 15 kbars and 1900°C for at least 20 minutes before being quenched. Run products were prepared and polished using the same procedure as the first set.

The resulting run products contained three phases: one silicate phase and two metallic phases, as shown in Fig. 3.2a. The two metallic phases present in each of the samples correspond to two immiscible metallic liquids present at run conditions, one S-
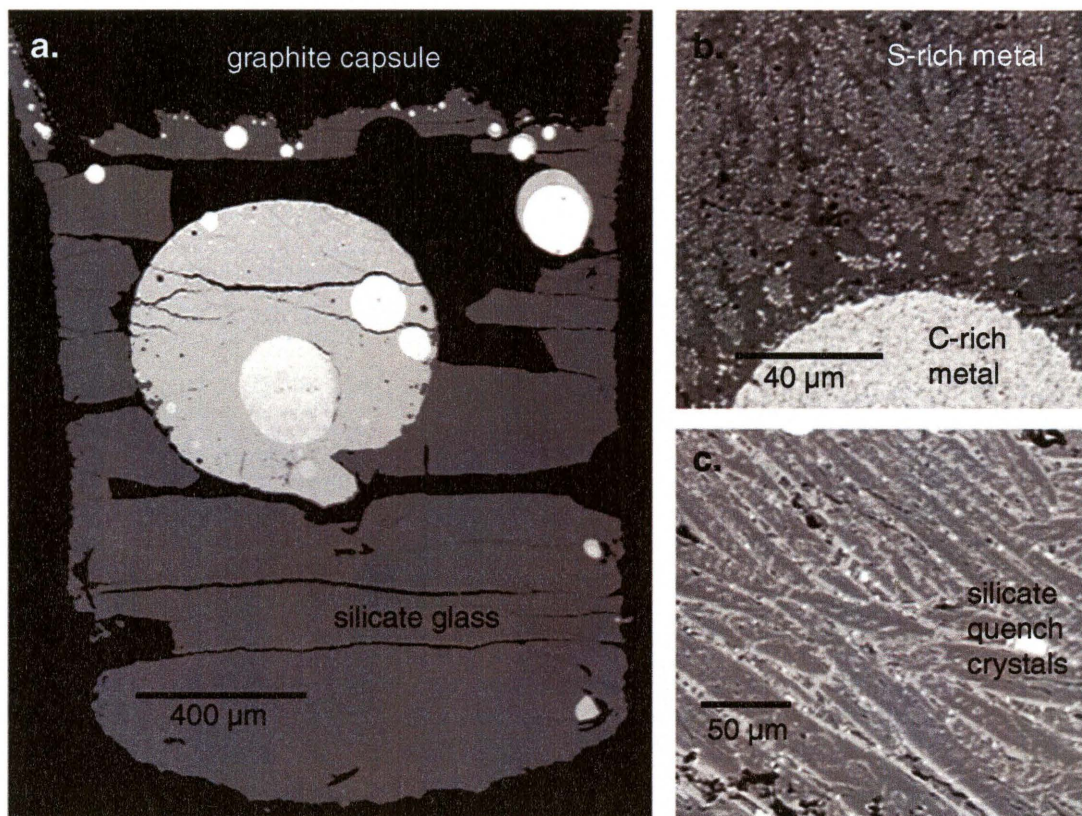
FIG. 3.2. BSE images of experiments which examined the effect of silicate composition on K solubility in metal are shown. **(a)** Experiment 55 began with a K-rich basalt and a mixture of Fe and FeS contained in a graphite capsule. In this case, the silicate liquid quenched to a homogenous glass, like runs from the first set of experiments. The run product contained two metallic phases, one S-rich and one C-rich. **(b)** The S-rich metal did not quench to a single phase, but rather formed large areas of FeS surrounded by regions which were mixtures of submicron-sized Fe and FeS. The C-rich metal also appeared to have a non-homogenous texture, but on a much smaller scale than the S-rich quench texture. **(c)** The silicate liquid did not quench to a glass in the more depolymerized experiments. Rather, the silicate melts formed olivine quench crystals surrounded by interstitial glass, as is shown in the BSE image from run 58.

TABLE 3.2. Set 2: Examining the effect of silicate composition.

Run:	36	55	54	61	59	62	63	58	39	41
Duration (min.)	20	30	40	60	50	70	80	50	50	270
S-rich metal										
Fe (wt%)	71.6±1.1	70.0±1.2	70.1±0.8	71.4±0.3	71.4±0.4	70.8±0.3	71.2±0.2	69.8±0.8	69.1±0.6	67.6±0.5
S (wt%)	27.7±1.3	29.3±1.2	29.6±1.0	28.4±0.14	28.1±0.2	28.5±0.2	28.2±0.16	28.0±0.9	27.3±0.9	26.8±1.0
Ni (wt%)									0.8±0.17	0.5±0.14
K (ppm)	50±20	30±12	66±26	50±20	40±16	36±14	30±12	270±110	130±50	150±60
C-rich metal										
Fe (wt%)	94.7±1.2	95.2±0.9	93.7±1.3	95.6±1.1	95.5±0.8	94.6±0.7	94.1±0.6	96.0±2.2	93.3±1.0	92.8±1.8
S (wt%)	1.5±0.4	1.0±0.2	1.6±0.8	1.6±0.6	1.4±0.4	1.4±0.14	1.6±0.2	1.5±0.15	1.2±0.4	0.9±0.3
Ni (wt%)									1.4±0.6	1.2±0.3
P (wt%)	0.7±0.1	0.23±0.18	0.5±0.16	0.4±0.2	0.19±0.13					
C (wt%)	3.1±1.3	3.6±0.9	4.2±1.5	2.4±1.3	2.9±0.9	4.0±0.7	4.3±0.6	2.5±2.2	4.1±1.2	5.1±1.9
Silicate										
Si (wt%)	27.9±0.2	19.0±0.3	20.5±0.4	20.6±0.4	20.1±0.3	19.5±0.4	18.6±0.15	18.2±0.3	15.9±1.0	16.3±0.5
Ti (wt%)		0.77±0.03	0.87±0.03	0.60±0.03	0.48±0.02					
Al (wt%)	9.3±0.1	5.5±0.13	6.0±0.1	4.7±0.1	4.3±0.09	3.3±0.24	2.0±0.8	0.8±0.3	1.2±0.6	0.9±0.4
Fe (wt%)	4.8±0.2	20.8±1.0	11.3±0.5	12.8±1.0	12.6±1.0	12.8±1.9	12.0±0.8	13.4±1.1	25.6±3.1	23.6±2.2
Mg (wt%)	0.8±0.1	2.8±0.2	7.6±0.2	9.8±0.14	12.6±0.2	16.3±0.8	21.2±3.1	23.9±1.7	17.3±2.1	18.2±1.7
Ca (wt%)		3.4±0.3	4.7±0.1	3.4±0.1	2.9±0.12	1.7±0.14	1.8±0.7	1.2±0.57	0.9±0.4	1.1±0.4
Na (wt%)	2.1±0.1	1.9±0.3	1.8±0.07	1.38±0.05	1.12±0.04	0.5±0.1	0.3±0.15			
K (wt%)	10.0±0.1	3.9±0.5	4.2±0.13	2.92±0.05	2.19±0.06	1.6±0.2	0.5±0.2	0.73±0.31	0.9±0.5	0.8±0.44
P (wt%)		0.4±0.18	0.27±0.04	0.23±0.05	0.21±0.02				0.09±0.03	0.08±0.01
S (wt%)	0.14±0.016	0.6±0.2	0.4±0.09	0.4±0.16	0.5±0.2	0.6±0.25	0.7±0.15	0.8±0.17	0.9±0.2	0.9±0.13
Calculated										
nbo/t	0.18±0.02	1.24±0.11	1.26±0.06	1.50±0.07	1.8±0.1	2.2±0.2	3.0±0.5	3.7±0.4	3.9±0.7	3.9±0.5
D_K ($*10^{-3}$)	0.5±0.2	0.8±0.3	1.6±0.6	1.7±0.7	1.8±0.7	2.3±0.9	6.0±3.4	37±22	14±10	19±13
D_S(S-rich/silicate)	200±24	50±16	70±17	60±26	70±25	50±20	40±9	35±8	30±7	29±4
D_S(C-rich/silicate)	11±3	1.7±0.7	4.2±2.7	3.0±1.5	4.0±2.2	2.3±1.0	2.3±0.6	1.9±0.4	1.3±0.5	1.0±0.4
log(fO$_2$/IW)	-2.3	-1	-1.6	-1.6	-1.6	-1.6	-1.7	-1.7	-1	-1

Reported errors are ±2σ. Aside from K, S, and P, for which special analytical procedures were used , concentrations below 0.2 wt% are not reported.

rich and one C-rich. The BSE image in Fig. 3.2b shows the two metallic phases in detail. The S-rich metallic phase formed a non-homogenous texture upon quenching, with large regions of FeS surrounded by areas which are a mixture of Fe and FeS down to the sub-micron scale. The quench texture of the C-rich metallic phase also appears non-homogenous in Fig. 3.2b, but on a much smaller scale than the texture of the S-rich metal. For most of the runs, the silicate phase quenched to a homogeneous glass, as shown in Fig. 3.2a. However, when the silicate material was more depolymerized, which was the case for runs 63, 58, 39, and 41, the silicate phase consisted of olivine quench crystals with interstitial glass, shown in detail in Fig. 3.2c.

3.2.3. Exploratory Experiments

In contrast to the two sets of systematic experiments just described, additional experiments were conducted at pressures between 15-80 kbars and temperatures between 1400-1900°C. Experiments at pressures greater than 15 kbars were conducted in the multi-anvil while experiments at 15 kbars were conducted in a piston cylinder apparatus. Starting compositions also varied but consisted of metal and silicate in approximately a 1:1 ratio.

Figure 3.3 shows a BSE image of run 7, which was conducted at 50 kbars and 1400°C in the multi-anvil. Frequently, at higher pressures and lower temperatures, the silicate would not be completely liquid and crystals would be stable. As an example, Fig. 3.3b shows some garnet crystals which were stable at run conditions. The starting
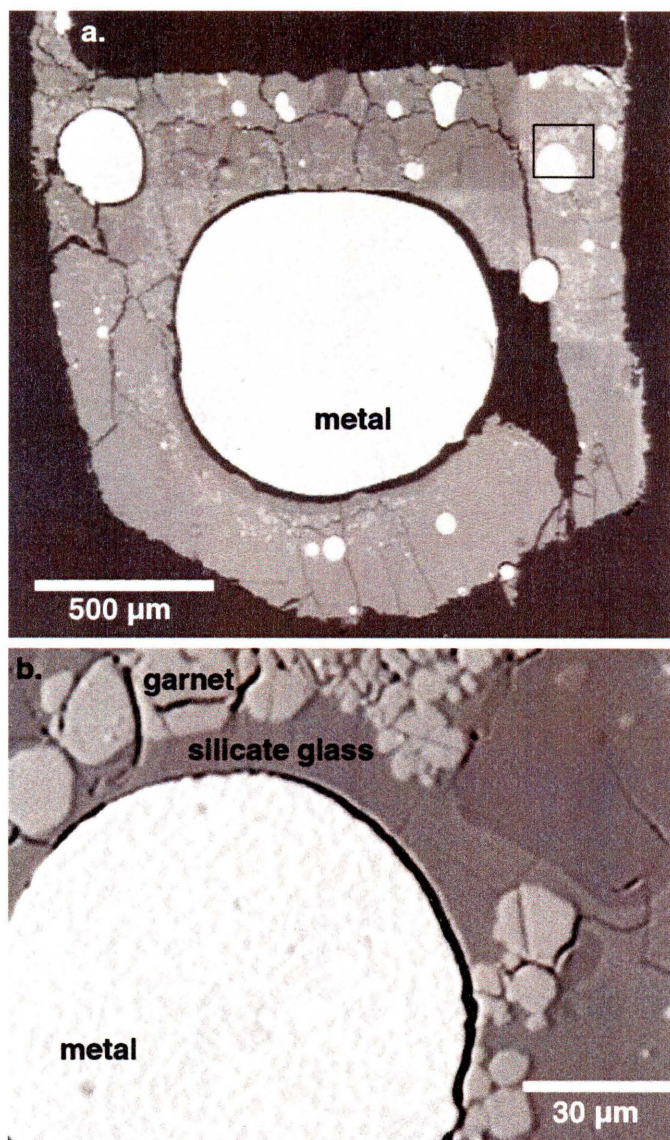
FIG. 3.3. BSE images of run 7 are shown. (**a**) The experiment was conducted in an alumina capsule in the multi-anvil. (**b**) The metal quenched to a dendritic texture, while the silicate formed crystals and a glass phase. With lower temperatures and higher pressures, the formation of crystals was common. In this example, the garnet identified has the composition of $Al_2Fe_3Si_3O_{12}$.

TABLE 3.3. Preliminary results from exploratory experiments.

Run	P (kbars)	T (°C)	$D_K(10^{-4})$	nbo/t	metal*
7	50	1400	5	0.3	26 wt% S
27	15	1700	0	0.02	3 wt% S
47	15	1700	9	1.1	29 wt% S
47	15	1700	0	1.1	4 wt% C
45	15	1700	60	3.9	27 wt% S
45	15	1700	0	3.9	5 wt% C
9	80	1700	10	0.14	25 wt% S
49	15	1800	10	1.7	29 wt% S
49	15	1800	0	1.7	5 wt% C
15	15	1900	0	0	Ni
32	15	1900	0	0	Ni, 5 wt% S
40	45	1900	1	0.16	25 wt% S
40	45	1900	0	0.16	5 wt% C
46	50	1900	20	1.0	28 wt% S
46	50	1900	0	1.0	5 wt% C
44	50	1900	70	3.9	25 wt% S
44	50	1900	0	3.9	5 wt% C
31	60	1900	1	0.14	21 wt% S
35	60	1900	1	0.19	19 wt% S

* The metal was dominantly Fe, unless indicated otherwise.

silicate and metallic compositions both influence which crystals will grow. However, all experiments still contained a silicate phase which was liquid at run conditions and quenched to a glass. The metal/silicate partition coefficient for K was determined using the concentration of K in the silicate glass, not in the crystals.

3.3. Analytical Techniques

All experimental run products were analyzed with the electron microprobe. Analysis of the silicate phase used a defocused beam of 10 μm to minimize loss of K and Na by volatilization. Operating conditions were 15 kV and 20 nA with a counting time of 20 sec. When it was necessary to measure low concentrations of S or P in the silicate, the beam current was raised to 200 nA and the counting time increased to 60 sec.

For the major elements in the metallic phases, operating conditions of 25 kV and 20 nA with a counting time of 20 sec. were used. A 10 μm raster beam was used for all measurements of the metallic phases due to the dendritic texture of the S-rich phase and the desire to measure the C-rich metallic phase using the exact same method. A raster beam of this size has been shown through image processing to accurately measure bulk compositions of similar dendritic textures (Chabot and Drake, 1997).

Low concentrations complicated the analysis of K in the metallic phases. To measure concentrations of K as low as 20 ppm reliably, operating conditions of 25 kV and 300 nA with a counting time of 500 sec. were necessary. The proximity of the K-rich silicate phase to the metallic phases further complicated the analysis. Secondary fluorescence effects from the neighboring K-rich glass interfered with measurements of

the metallic composition if the measurements were made within 50 μm of the K-rich phase. This effect was quantified by creating three test samples. Each test sample consisted of a slice of natural K-feldspar pressed up against a piece of either iron sulfide, Ni metal, or stainless steel. A series of measurements was then made across the interface of the K-feldspar and the other component. Even though there was no K in the iron sulfide, Ni metal, or stainless steel, a non-zero K measurement was made unless the measurement was conducted more than 50 μm from the K-feldspar. This result is shown in Fig. 3.4 and is a serious effect that must be considered any time a low concentration is being measured next to a phase with a high concentration of the same element. Capobianco and Amelin (1994) reported a similar effect when measuring the concentrations of trace elements in the silicate near the interface with the metal.

To further test the K measurements of the metallic phase, an experiment consisting of ground SiO_2 with an Fe, FeS mixture was run at 15 kbars and 1900°C in an alumina capsule. In this K-free experiment, the S-rich metallic phase contained about 10 wt% S and quenched to a dendritic texture exactly like the run products from the first set of experiments which varied S. Repeated analysis of the metallic phase using the same analytical technique as used on the K-bearing experiments yielded K measurements of 10 ppm or less.

For the analysis of each run product, measurements of the K concentration in the metallic phase were interspersed with measurements of the K-free experiment and a previously analyzed sample. Before the K measurement for the new run was considered valid, the K-free experiment had to report 10 ppm K or less in the metallic phase and
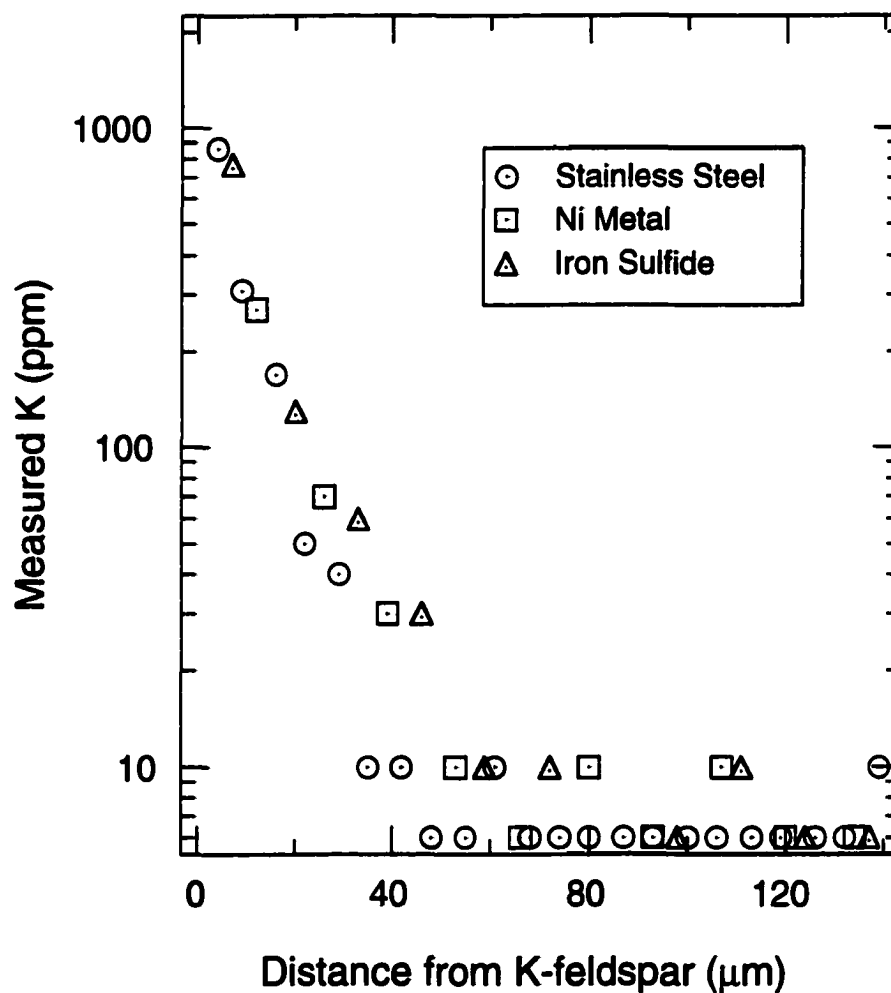
FIG. 3.4. A slice of K-feldspar was pressed up against a piece of stainless steel, Ni metal, or iron sulfide and analyzed by the same microprobe techniques as the metallic phases of the experimental runs. Even though there was no K in these materials, a non-zero K measurement was made unless the K-feldspar was at least 50 μm away.
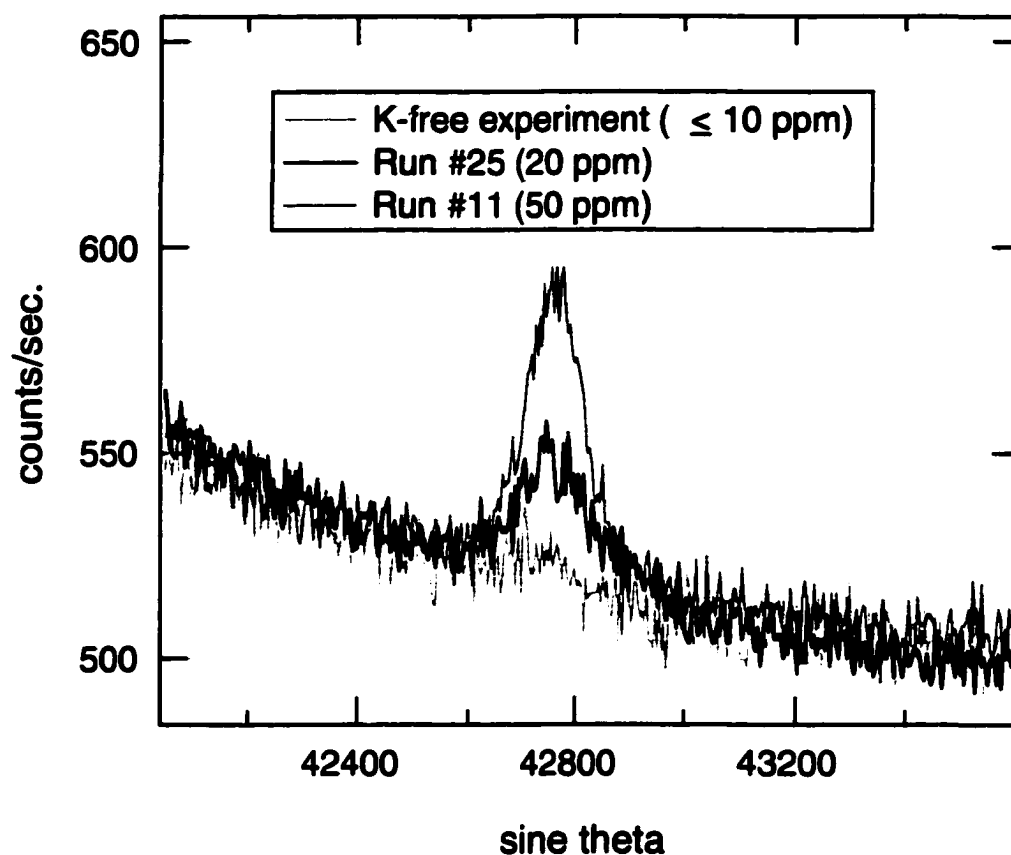
FIG. 3.5. The electron microprobe spectrometer, using a PET crystal, was scanned over the wavelengths of the K peak for the K-free experiment, run 25, and run 11. I measure 20 ppm K in run 25, the lowest level of K I claim to be able to measure reliably. The 20 ppm peak is clearly distinguishable from the K-free experiment, which I measure to contain 10 ppm or less. Concentrations of 50 ppm K, as in run 11, are significantly above background and different from a 20 ppm K peak. The scans were made using the same beam current of 300 nA, voltage of 25 kV, and beam size of 10 μm as are used to determine the K concentration in the metallic phase of the run products. However, the counting time was only 30 sec. rather than 500 sec.

the previously measured sample had to give a K concentration consistent with previous measurements. Using this strict analysis procedure and taking all cautions to avoid secondary fluorescence effects, I have confidence that K concentrations of 20 ppm or higher are due to the solubility of K in the metal during the experiment. Figure 3.5 shows a 20 ppm K microprobe peak which is clearly distinguishable from the K-free experiment and a 50 ppm K peak.

Table 3.1 and Table 3.2 list the microprobe measurements for each run along with the errors. The lack of any compositional gradients in the run products and the agreement between runs 39 and 41, which were prepared with the same starting composition but conducted for very different run durations, suggest the experiments attained equilibrium. Preliminary results in Table 3.3 have not been as rigorously determined as the measurements made on the systematic experiments and are consequently listed without errors. Though the amount of K in each experiment is well above the estimated primitive mantle abundance for the Earth of ~100 ppm (Wänke, 1981), variations in D_K are not correlated with either the concentration of K in the silicate or in the metal, suggesting the partitioning results are not significantly influenced by the concentration of K in the sample.

The second set of experiments, which were run in graphite capsules, contained two metallic phases, one S-rich and one S-poor. The microprobe spectrometer, using a PC2 crystal, was scanned over the wavelengths of the C peak for each of the metallic phases. Though all scans showed a C peak due to the carbon coat applied for microprobe analysis, a larger C peak was always detected in the S-poor metallic phases than in the
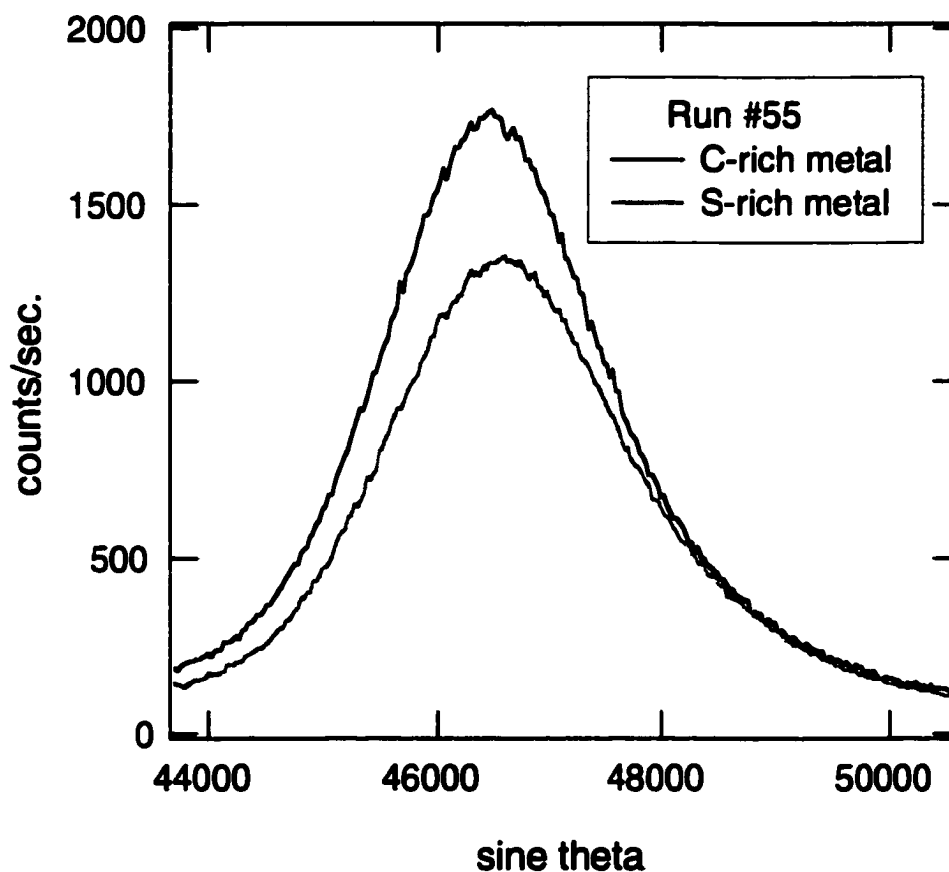
FIG. 3.6. For all of the runs investigating the effect of silicate melt composition, the electron microprobe spectrometer, using a PC2 crystal, was scanned over the wavelengths of the C peak in both of the metallic phases. Both phases showed a C peak from the carbon coat applied for microprobe analysis. However, the S-rich metallic phase always had a significantly lower peak than the S-poor metallic phase, as shown here for run 55. The larger C peak along with the low totals for the S-poor metallic phase and the consistency of the compositions of the two metallic phases with the C-Fe-S phase diagram, lead me to believe the S-poor metallic phase is indeed C-rich.

closely neighboring S-rich metallic phases. A pair of such scans is shown in Fig. 3.6 for the experiment depicted in Fig. 3.2a. Also, analysis of the S-poor metallic phases consistently yielded low totals. If the totals were assumed to be low due to C present in the S-poor metallic phase, the inferred compositions of the two immiscible metallic liquids are consistent with the C-Fe-S phase diagram (Raghavan, 1988). I thus concluded that in the second set of experiments, the S-poor metallic phase is C-rich.

3.3.1 Determining Errors

For homogeneous phases, such as quenched silicate glass or pure Fe-metal, errors shown on Table 3.1 and Table 3.2 were computed as twice the standard deviation of multiple microprobe measurements. The C-rich metallic phase displayed inhomogeneities when examined at high magnification, but the scale of this texture was small when compared to the 10 μm raster beam used for the analysis. Thus, twice the standard deviation of multiple measurements was also used to represent the error for measurements of the C-rich metal. The C-content of the C-rich metal was calculated by assuming the microprobe total would be 100, and the error shown in Table 3.2 is the $\pm 2\sigma$ uncertainty in the sum of the measured elements, Fe, S, Ni, and P, assuming the error in each element is independent of each other.

For the silicate and metallic textures that were molten at run conditions but did not quench to a single phase, individual measurements may vary significantly due to the amount of each quenched phase which is analyzed. Twice the standard deviation of multiple measurements represents the error between each measurement but by

averaging multiple measurements, the bulk composition can be determined more accurately than the difference between individual measurements would suggest. Thus, twice the standard deviation of the mean was used to represent the error in these cases. For calculated quantities, such as D_K or nbo/t, the $\pm 2\sigma$ errors are computed assuming the errors for each element are independent of each other.

Determining the error for the K-content of the S-rich metal was less straight-forward. As noted by Hillgren et al. (1996), for elements present in extremely low concentrations, the standard deviation of the mean can yield unreasonably small errors. However, the measured K-content was found to vary significantly from measurement to measurement in some run products, due to the size of the quenched phases present. Table 3.4 lists the measured K-content of the S-rich metal in each run, as determined from the average of multiple electron microprobe measurements. The number of analyses, twice the standard deviation, and twice the standard deviation of the mean are also given. Simply using twice the standard deviation of multiple measurements to represent the errors results in large errors, over 100% in one case. Figure 3.5 and repeated analyses of the K-free experiment show that 20 ppm K or higher is distinguishable from background, but using twice the standard deviation results in an error so large as to suggest otherwise. Twice the standard deviation of the mean has the opposite problem, suggesting errors of only a few ppm. The concentrations of K being measured are distinguishable from background, but they are still extremely low for measurements made with the electron microprobe. Errors less than 10%, as suggested by twice the standard deviation of the mean in some cases, are unrealistically low.

To examine the error inherent in measuring low concentrations of K without the added complication of a non-homogenous quench texture, run 25 offers some insight. Run 25 contains just 2.3 wt% S in the S-rich metal, and thus the quench texture is identifiable but dominated by large Fe dendrites. Using a 10 μm raster beam, the S-content determined from measurement to measurement does not vary as much as for runs which contain more S, suggesting twice the standard deviation of multiple measurements is a reasonable representation of the error. For run 25, twice the standard deviation of multiple measurements of the K-content results in a 40% error. Thus, perhaps estimating the error for each run as 40% of the measured K concentration could represent the error associated with measuring a low K concentration using the electron microprobe. Run 25 also has the lowest reported K-content, only 20 ppm, and it seems higher K-contents would be less difficult to measure. Thus, the 40% error may be overestimating the difficulty of measuring K for the other runs. The last column in Table 3.4 contains the 40% error for each run, which is larger than twice the standard deviation of the mean and usually less than twice the standard deviation. Tables 3.1 and 3.2, as well as Fig. 3.7 and Fig. 3.8, use 40% errors for the K-content as a most basic way of estimating the error in the K measurements.

3.4. Results

3.4.1 Effect of S

The measured metal/silicate weight partition coefficients for K from Table 3.1 are plotted in Fig. 3.7 as a function of the wt% S in the metallic phase. The $\pm 2\sigma$ error bars

TABLE 3.4. Determining the error for the K-content of the S-rich metal.

Run	K (ppm)	# analyses	2*std	2*std mean	40% error
25	20	20	8	1.8	8
11	50	27	34	6.5	20
24	40	31	36	6.5	16
13	70	22	46	10	28
36	50	8	12	4	20
55	30	12	16	4.6	12
54	66	12	34	10	26
61	50	11	40	12	20
59	40	14	16	4	16
62	36	10	22	7	14
63	30	14	34	9	12
58	270	12	240	70	110
39	130	16	110	28	50
41	150	9	140	50	60

are quite large, due to the heterogeneous nature of the dendritic metallic phase and the low concentrations (20-70 ppm) of K being measured. However, when no S was present and the metallic phase was just pure Fe, no detectable amount of K was measured in the metal. The error bars may be too large to define a definite trend between D_K and wt% S, but even as little as 2.5 wt% S increases the K concentration in the metallic phase to a detectable level. This suggests the presence of S increases the solubility of K in metal, possibly through the formation of K_2S complexes.

As shown in Fig. 3.7, the metallic composition ranged from pure Fe to a mixture of Fe with 23 wt% S. All experiments were run at the same pressure, 15 kbars, and temperature, 1900°C, but the silicate composition and the oxygen fugacity varied slightly between experiments. The starting silicate composition was K-feldspar but 5-10 wt% Fe was measured in the quenched silicate glass, as listed in Table 3.1. Estimating the activities of Fe in the metal and FeO in the silicate as their mole fractions (Hillgren et al., 1994), the oxygen fugacity relative to iron-wüstite (IW) was calculated for each experiment and found to vary from 1.6-2.4 orders of magnitude below the IW buffer.

3.4.2 Effect of C

The second set of experiments, which were run in graphite capsules, produced two metallic phases, one S-rich and one C-rich. The C-rich phases contained 3-5 wt% C. Analysis of the C-rich metallic phases showed that K concentrations were below detection limits, 10 ppm or less, in all experiments. Even as the silicate composition varied, the solubility of K in the C-rich metal remained lower than could be measured.

FIG. 3.7. Results from experiments which examined the effect of S on K solubility in metal are plotted as the metal/silicate weight partition coefficient, D_K, against the wt% S in the metallic phase. Error bars of $\pm 2\sigma$ are large due to the low concentrations of K being measured and the dendritic texture of the metal. However, a S-free experiment with pure Fe-metal does not contain detectable amounts of K in the metallic phase, while as little as 2.5 wt% S increases the K concentration in the metal to a detectable level. The presence of S appears to increase K solubility in metal, though the maximum D_K measured in the first set of experiments is still only $9*10^{-4}$.

However, in all the experiments, the neighboring S-rich metallic phase contained detectable concentrations of K. Thus, the presence of C, unlike the presence of S, does not increase K solubility in metal to detectable levels. Potassium sulfide minerals have been observed in natural systems (e.g., djerfisherite in enstatite chondrites, Fuchs, 1966) while I am unaware of any natural K-carbide minerals. Intuitively, K-carbides might be more difficult to form than K-sulfides due to the large ionic radius of K and the need for four large K atoms to charge balance a single smaller C atom.

3.4.3 Effect of Silicate Composition

Unlike the C-rich metallic phases, the S-rich metallic phases in the second set of experiments contained measurable concentrations of K, as listed in Table 3.2. The S-rich metallic phases contained 27-29 wt% S, and Fig. 3.8 shows D_K, determined from the S-rich metal and the silicate, plotted against the molecular quantity of nbo/t, the ratio of non-bridging oxygens over tetrahedral cations in the silicate melt (Mysen, 1991). The quantity nbo/t has been shown to be a useful parameter by which to quantify the silicate melt composition and is a rough measure of the network modifiers to the network formers in the silicate melt. Larger nbo/t values represent silicate melts which have a more depolymerized structure, with an nbo/t of 0 corresponding to a fully polymerized melt and an nbo/t of 4 corresponding to a completely depolymerized melt. Over the range of silicate compositions covered by the experiments, D_K varies by almost two orders of magnitude, showing that silicate composition can significantly affect the solubility of K in metal.

My experimentally-determined D_K can be fit by the following expression:

$$\log(D_K) = -3.5 + 0.46(nbo/t) \qquad\qquad \textbf{Eq. 3.2}$$

As nbo/t increases, the silicate melt becomes increasingly depolymerized and D_K increases. In a silicate melt structure, K tends to act as a network former, charge balancing Al. As the silicate melt becomes increasingly depolymerized, the network is broken down and the reduction of charge balancing Al may make the silicate melt less energetically favorable for K.

Like the first set of experiments which examined the effect of S, all experiments in the second set were run at a pressure of 15 kbars and temperature of 1900°C. The S-content of the metallic phase varied by a few wt% between the experiments, but as Fig. 3.7 shows, this variation should not significantly affect the observed partitioning behavior. The approximate oxygen fugacity of each experiment was calculated using the Fe concentration in the C-rich metallic phase and the FeO-content of the silicate melt, as was done for the first set of experiments. Calculated oxygen fugacities were comparable to those of the first set of experiments and varied between 1.0 to 2.2 orders of magnitude below the IW value.

Murrell and Burnett (1986) ran an experiment at 15 kbars and 1450°C and reported a D_K of 0.0027. Unfortunately, they did not report their final silicate composition, only their starting material, which was Juan de Fuca glass with an nbo/t of 0.9. However, in my experiments, the final silicate composition is always significantly different from the

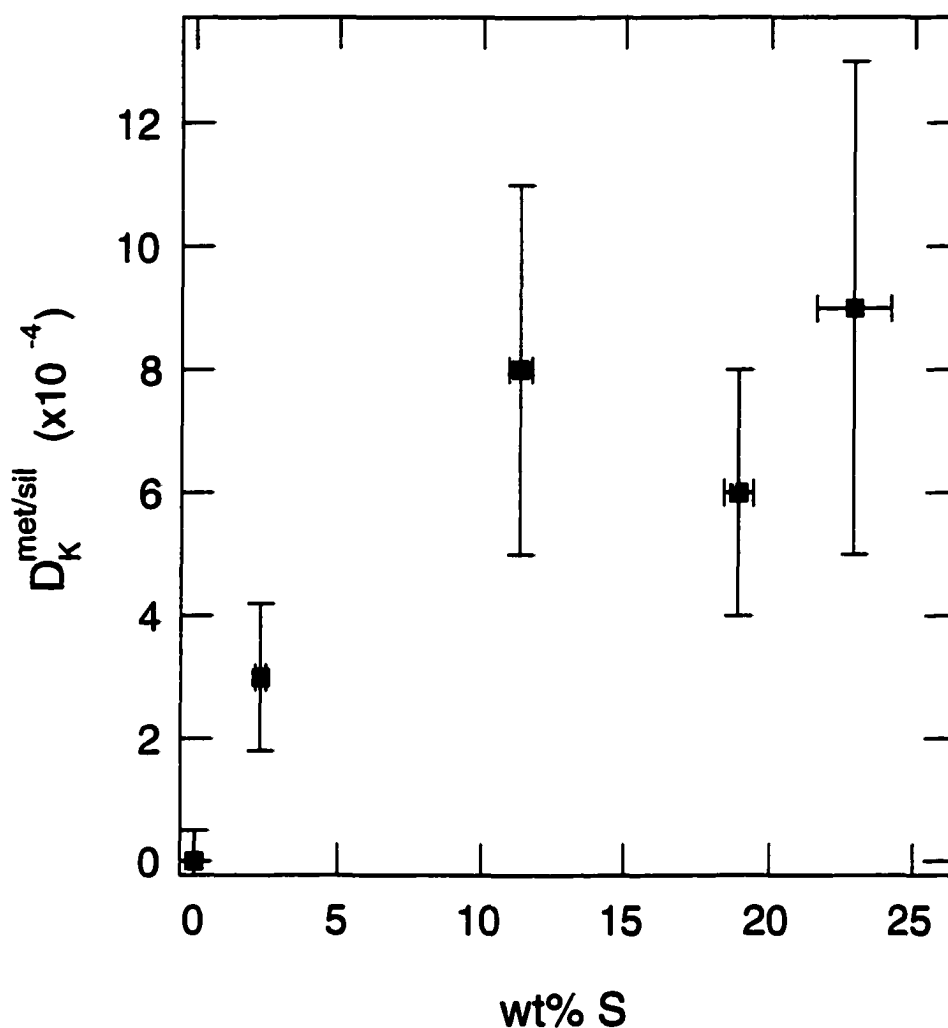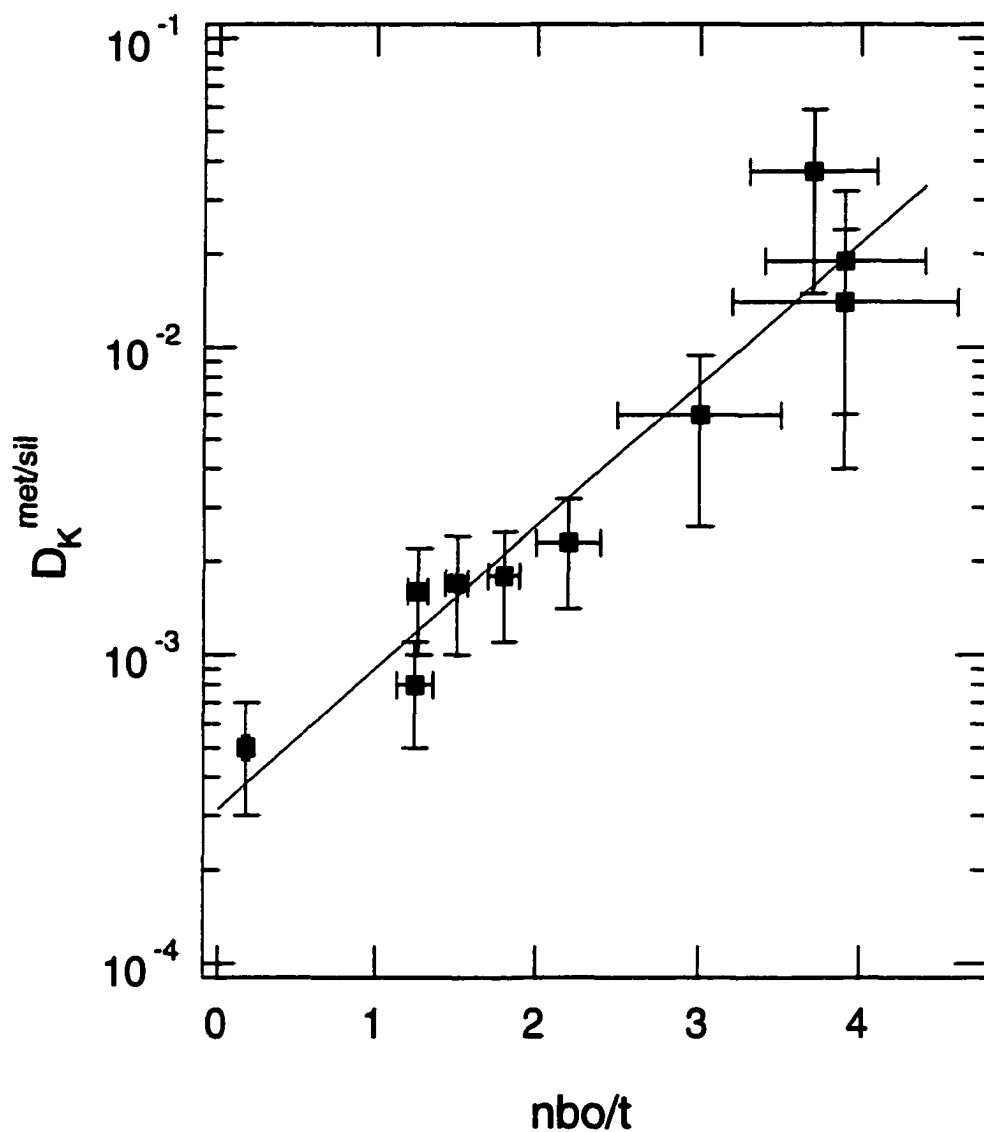**FIG. 3.8.** Results from experiments which examined the effect of silicate composition on K solubility in metal are plotted as the metal/silicate weight partition coefficient, D_K, against the nbo/t, non-bridging oxygens/ tetrahedral cations, of the silicate phase. As the silicate becomes more depolymerized, D_K increases by nearly two orders of magnitude. The trend can be fit within error by a straight line.

starting material, due largely to the increase in the FeO-content of the silicate melt. If the effect of the temperature difference between their experiment and my experiments is negligible, their reported D_K is consistent with a final silicate composition having an nbo/t of 2.

3.4.4 Effect of Pressure and Temperature

Exploratory experiments were conducted at a variety of pressures and temperatures using different starting compositions. Table 3.3 lists the preliminary results from some of those experiments. Two experiments were conducted using Ni instead of Fe as the metallic phase, and in both experiments, no K was detected in the metallic phase. Even when the metallic phase was Ni-rich with 5 wt% S, the K-content of the metal was still lower than could be detected with the electron microprobe. In the first set of systematic experiments, as little as 2.5 wt% S was enough to increase the solubility of K in Fe-rich metal to a detectable level.

Many of the experiments listed in Table 3.3 were run in graphite capsules and produced two metallic phases, one S-rich and one C-rich. In all cases, the C-rich metallic phase contained no detectable K. The second set of systematic experiments found that S, but not C, was necessary to produce a K concentration in the metallic phase at a high enough level to be detected with the electron microprobe. The results of the exploratory experiments are consistent with that conclusion.

Experiments listed in Table 3.3 which contained an Fe-rich metallic phase with at least 19 wt% S are plotted in Fig. 3.9. Figure 3.9a shows D_K plotted against the pressure

of the experiment, while Fig. 3.9b plots D_K versus temperature. In both graphs there is

no correlation between the metal/silicate partition coefficient and either pressure or

temperature. In fact, the scatter in the D_K data is consistent with the different final

silicate compositions, regardless of the pressure and temperature of each experiment, as

shown on Fig. 3.9c. Figure 3.9c plots D_K versus nbo/t, just as Fig. 3.8 does. Experiments

which produced more depolymerized silicate melts also produced a higher D_K, just as

was found by the second set of systematic experiments. My experiments show no

evidence for changes in pressure or temperature to increase the solubility of K in metal.

However, a higher pressure and temperature than covered by my experiments are

believed to be relevant to core formation in the Earth, and K solubility in metal remains

to be thoroughly investigated at those conditions.

3.4.5 Partitioning of S, P, and Ni

In most of the experiments, S was present. The majority of the S created a S-rich

metallic phase, but concentrations of S in the silicate phase were still detectable. Table

3.1 and Table 3.2 list the measured S-contents of the metallic and silicate phases as well

as the calculated metal/silicate weight ratio partition coefficients for S, D_S. Figure 3.10a

plots D_S against the wt% S in the metallic phase, as determined from the first set of

experiments listed in Table 3.1. As more S is present in the metal, the concentration of

S in the silicate does not increase as quickly, resulting in an increase in D_S as a function

of the wt% S in the metallic phase. This result suggests one must be cautious before
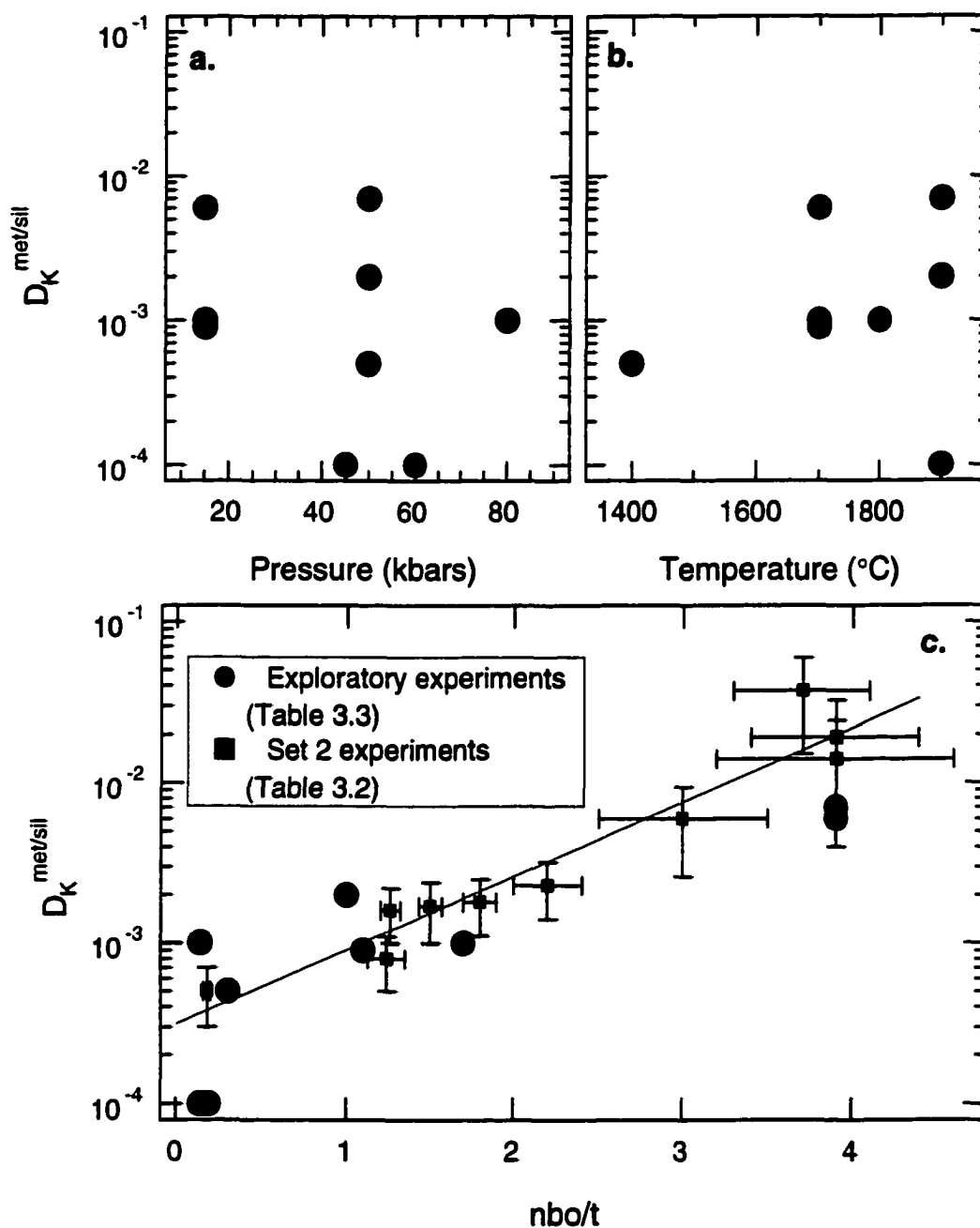
FIG. 3.9. Results from the exploratory experiments listed in Table 3.3 which contained an Fe-rich metallic phase with at least 19 wt% S are plotted against (a) pressure, (b) temperature, and (c) silicate composition represented by nbo/t. The scatter in the experiments is consistent with the different silicate compositions in the experiments. There is no evidence for pressure and temperature to increase the solubility of K in metal.
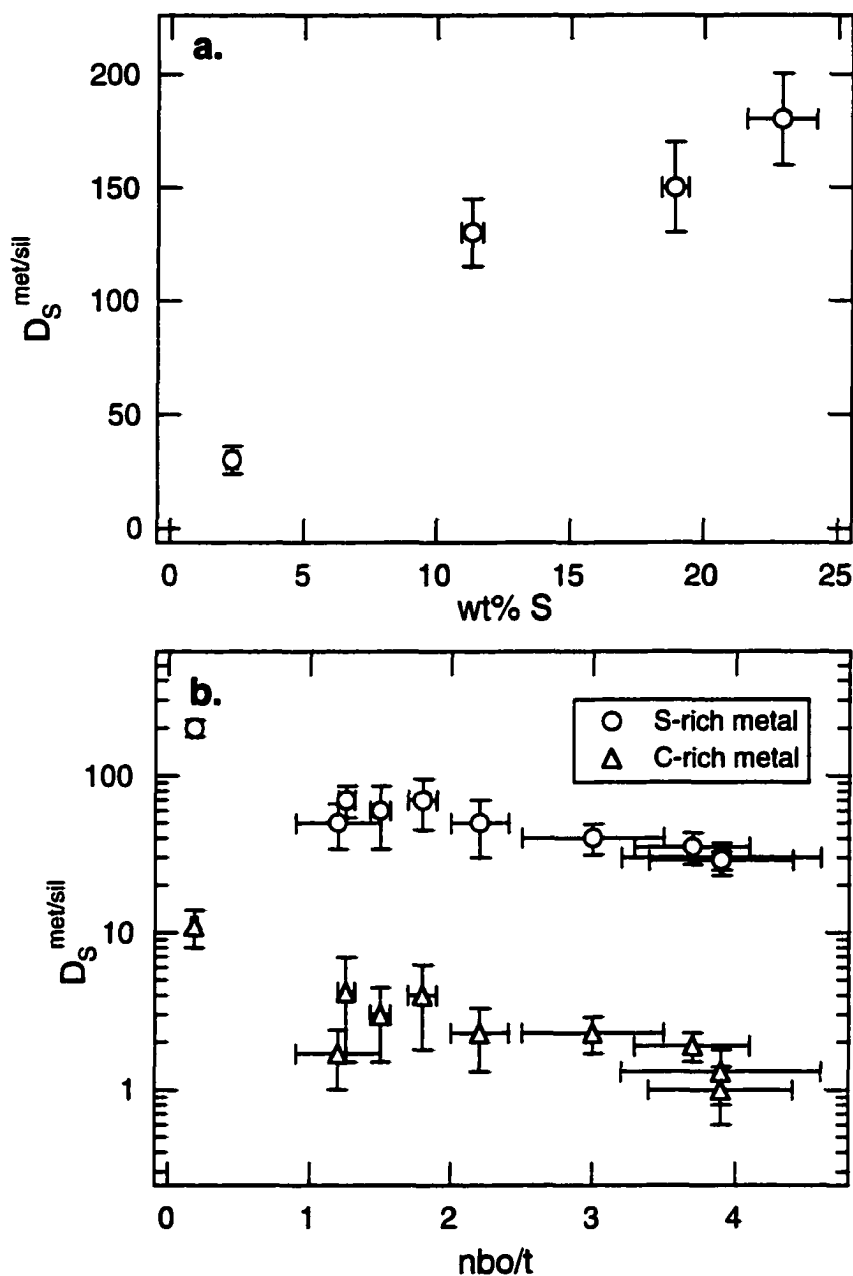
FIG. 3.10. The metal/silicate weight partition coefficient for S, D_S, is plotted as a function of the metallic and silicate compositions. (a) As the wt% S in the metallic phase increases, so does D_S. The S solubility in the silicate melt does not increase as quickly as the S in the metallic phase, causing D_S to increase. (b) As the silicate melt becomes more depolymerized, and the nbo/t value increases, D_S decreases slightly, though the $\pm 2\sigma$ errors are large. The effect of silicate composition seems to be the same for partitioning between S-rich metal and silicate and C-rich metal and silicate.

applying any results from metal/silicate partitioning experiments for S conducted with large amounts of S to the observed S abundance in the Earth's mantle. Figure 3.10b displays the results of the second set of experiments, plotting D_S as determined for both the S-rich and C-rich metals against nbo/t. The dependence of D_S on nbo/t is similar for both the S-rich and C-rich metallic phases, decreasing slightly with increasing depolymerization of the silicate melt. The dependence of the solubility of S in silicates on the silicate composition has been previously observed and modeled (Haughton et al, 1974; Wallace and Carmichael, 1992; Li and Naldrett, 1993).

For the second set of experiments, where the starting silicate compositions were mixtures of natural materials, trace amounts of P were present in some of the runs. Table 3.2 shows the solubility of P in metal is greatly affected by the silicate composition. For run 36, which has an nbo/t value of 0.18, a significant amount of P was measured in the C-rich metal, while the P-content of the silicate was below the detection limit. However, for runs 39 and 41, which both have an nbo/t value of 3.9, the opposite behavior was observed, with P being detected in the silicate but not in the metal. A similar decrease in the metal/silicate partitioning of P with increasing nbo/t and depolymerization of the silicate melt was noted in the experiments of Jana and Walker (1997). Table 3.2 also shows the preference of P for the C-rich metal over the S-rich metal; phosphorus was not detected in the S-rich metal, only in the C-rich metal and the silicate. Solid metal/liquid metal experiments (Jones and Drake, 1983) also suggest S decreases the affinity for P in the metallic phase, but no such experiments examining the effect of C on P partitioning exist.

Experiments which began with Allende contained traces of Ni in the final run product. The concentration of Ni in the silicate was undetectable, but Ni was detected in both the C-rich and S-rich metallic phases. Solid metal/liquid metal experiments which examined the effects of C (Willis and Goldstein, 1982; Lauer and Jones, 1999) and S (Jones and Drake, 1983; Jones and Malvin, 1990) on the partitioning behavior of Ni suggest the C-rich metal would have the higher concentration of Ni. From these previous solid metal/liquid metal experiments, the predicted ratio for my experiments of the concentration of Ni in the C-rich metal to that in the S-rich metal is about 1.2. The measured partitioning ratio of the concentration of Ni in the C-rich metal to that in the S-rich metal in my experiments is about 2 ±0.9, which is within error of the value predicted by previous solid metal/liquid metal experiments.

3.5. Implications

If the mantle peridotite KLB-1 is taken to represent the silicate involved in core formation (Takahashi, 1986), a value for nbo/t of 2.8 is calculated for the early, differentiating Earth. If S is a significant light element in the Earth's core, such a value of nbo/t suggests, by equation 3.2, a D_K of $6*10^{-3}$. Using a primitive mantle abundance for K from Wänke (1981) of ~100 ppm, a D_K of $6*10^{-3}$ yields a concentration of less than 1 ppm K in the Earth's core. This level of K would generate a present day heat production of about 10^{10} W.

Calculating the amount of power required to drive convection and run the Earth's geodynamo depends on the exact nature of the power source. For radioactive heating

alone, Gubbins et al. (1979) determined 10^{13} W would be necessary to drive the Earth's geodynamo. Stacey (1992) estimated $4*10^{12}$ W is the current day heat loss from the core, and using this heat flux, Buffett et al. (1996) calculated that thermal and compositional convection processes would contribute $4*10^{11}$ W and $5*10^{11}$ W respectively to driving the geodynamo. Thus, the presence of 10^{10} W from the decay of less than 1 ppm K in the Earth's core is small compared to the power necessary for radioactive heating to power the geodynamo and to estimates of the other sources present in the Earth's core to drive convection.

However, the above calculation is based on experiments conducted only at 15 kbars and 1900°C and does not consider the possible effects of pressure and temperature, which could be important when discussing core formation in the Earth. The effect of oxygen fugacity has also been ignored. However, my preliminary results show no indication that either pressure or temperature will increase the solubility of K in metal. Murrell and Burnett (1986) concluded that if radioactive heating is an important heat source in planetary cores, heating from U and Th would be more significant than heating from K. Further studies are needed before the importance of all types of radioactive heating in planetary cores can be determined.

CHAPTER 4

PARTITIONING OF ELEMENT PAIRS USED AS CHRONOMETERS

The effects of light elements, such as S and P, on solid metal/liquid metal partition coefficients can significantly influence the behavior of elements during core crystallization. For Ag and Pd, Re and Os, two element pairs used to date iron meteorite processes, the effects of S and P on their partitioning behavior were incompletely known. I have experimentally determined the solid metal/liquid metal partition coefficients of these important element pairs as a function of the S and P concentrations in the metallic liquid.

Silver is incompatible in solid metal and strongly sensitive to the S-content of the metallic liquid; partition coefficients for Ag decrease more than an order of magnitude with increasing S-content of the metallic liquid. The partition coefficient of Pd is less variable than Ag and increases with increasing S-content of the metallic liquid, changing from modestly incompatible to modestly compatible in solid metal. Phosphorus has no effect on the partition coefficient of either Ag or Pd, which are incompatible and identical within experimental error. With these new partition coefficients, the distribution of Ag and Pd in magmatic iron meteorites can be better understood.

The solid metal/liquid metal partition coefficients of Re and Os were previously known to increase significantly with increasing S-content of the metallic liquid, but the effect of P on their partitioning behavior was unknown. Within experimental error, I have shown that Re and Os have identical partitioning behavior as a function of the P concentration and show increasing compatibility in the solid metal with increasing P-content of the metallic liquid.

4.1 Introduction

The distribution of trace elements in iron meteorites can be used to interpret the formation and evolution of the metallic cores of asteroids, their presumed parent bodies. Silver and Pd are of particular interest because radioactive ^{107}Pd decays to ^{107}Ag with a geologically short half life of 6.5 Ma. Thus, if iron meteorites crystallized in the presence of live ^{107}Pd, the distribution of the radiogenic daughter, ^{107}Ag, potentially can be used to constrain formation processes (Kaiser and Wasserburg, 1983; Chen and Wasserburg, 1983, 1990, 1996). Despite the interest in this pair of isotopes for chronometry, experimental determinations of the partitioning behavior of Ag or Pd are few (Jones and Drake, 1986; Fleet and Stone, 1991; Jones et al., 1993) and seem inconsistent with some geochemical observations of iron meteorites.

Within iron meteorite groups, Pd concentrations correlate linearly and positively with Ni concentrations. If these correlations are due to the crystallization history of the meteorite parent body, as is generally assumed (Scott, 1972), then Pd, like Ni, should exhibit slightly incompatible behavior in solid metal. However, the only previous experimental studies reporting on the partitioning of Pd between solid metal and liquid metal find slight solid metal compatibility (Fleet and Stone, 1991; Jones et al., 1993).

Kaiser and Wasserburg (1983) and Chen and Wasserburg (1983,1990) measured Ag and Pd concentrations in troilite-rich nodules of iron meteorites. The distribution of Ag and Pd between metal and nodules in these meteorites is not well understood in that it matches predictions from neither solid metal/liquid metal nor metal/troilite partitioning experiments. The observed metal/nodule distributions of both Ag and Pd exhibit a wide range of values which also has not been well explained.

Willis and Goldstein (1982) and Jones and Drake (1983) have shown that solid metal/liquid metal partition coefficients (D) are sensitive to the S-content and P-content of the metallic liquid. However, only for compositions near the eutectic in the Fe-FeS

system are Ag and Pd partition coefficients known. To better understand Ag and Pd partitioning in iron meteorites, a systematic study of Ag and Pd partitioning between solid Fe-metal and S-rich or P-rich metallic liquid was conducted as a function of the S-content and P-content of the metallic liquid. These new measurements quantify the partitioning behavior of Ag and Pd as a function of the S-content and P-content of the metallic liquid and reconcile some, but not all, of the inconsistencies between iron meteorite observations and laboratory experiments.

In contrast to the short-lived Ag-Pd system, ^{187}Re decays to ^{187}Os with the geologically long half life of 41 Ga. The long-lived Re-Os system has been used to constrain the time of core formation and core crystallization of the iron meteorite parent bodies (Smoliar et al., 1996; Shen et al., 1996). The effect of S on the partitioning behavior of Re and Os has been previously quantified (Jones and Jurewicz, 1989). The solid metal/liquid metal partition coefficients of both Re and Os increase significantly with increasing S-content of the metallic liquid, changing by over two orders of magnitude between the S-free system and an Fe-FeS eutectic composition. The effect of P on the partitioning behavior could also be significant but has not been determined. With this motivation and due to the ease of adding Re and Os to the experiments, I have determined the partitioning behavior of Re and Os as a function of the P-content of the metallic liquid.

4.2 Experimental and Analytical Procedures

Two sets of systematic experiments were conducted. The first involved the determination of the effect of S on the partitioning behavior of Ag and Pd (Chabot and Drake, 1997). The second set of experiments examined the effect of P on the partitioning of Re and Os in addition to Ag and Pd (Chabot and Drake, 1999b). Because the S-bearing experiments were conducted first, the experimental and analytical procedures were tested with these experiments and then simply used to conduct the P-bearing runs.

4.2.1 Examining the Effect of S

Experimental methods were similar to those used by Jones and Drake (1983). Approximately 200 mg mixtures of Fe and FeS, with Pd or Ag at the few wt% level, were loaded into alumina crucibles approximately 5 mm in diameter and 2 cm in length. Silver and Pd were run in separate experiments to avoid interferences between their X-ray lines. The crucibles were inserted in high purity silica glass tubes that were 9 mm in inner diameter with 2 mm thick walls. The tubes were then evacuated and heated in a Deltech vertical tube furnace. Runs were made at temperatures between 1455°C and 1150°C. At the higher temperatures it was important to flow fresh laboratory air through the furnace tube to prevent devitrification of the silica glass. Charges were held at temperature for 3 hours to 7 days, depending on temperature. Temperature was monitored continuously with $Pt-Pt_{90}Rh_{10}$ thermocouples calibrated against the melting point of Au. Experimental conditions for individual runs are summarized in Table 4.1. Runs were quenched in water. Sulfur-bearing liquid metal did not quench to a single homogeneous phase but to Fe dendrites surrounded by FeS, as shown in a back scattered electron image in Fig. 4.1.

Solid metal/liquid metal partition coefficients were measured by standard CAMECA SX50 electron microprobe analysis techniques. Operating conditions were 15 kV accelerating potential and 20 nA sample current in the faraday cup, with counting times of 20 sec. for Fe and S and 60 sec. for Ag and Pd. To measure the low Ag-content of the solid metal, settings of 200 nA sample current in the faraday cup and 120 sec. counting times were used. A point beam was used for analysis of the solid metal and a 16 μm raster was used on the two-phase quenched liquid. Typically, 50-100 raster analyses were averaged to calculate bulk compositions for the metallic liquids. Reported errors in Table 4.1 are dominated by the uncertainty in determining the composition of the metallic
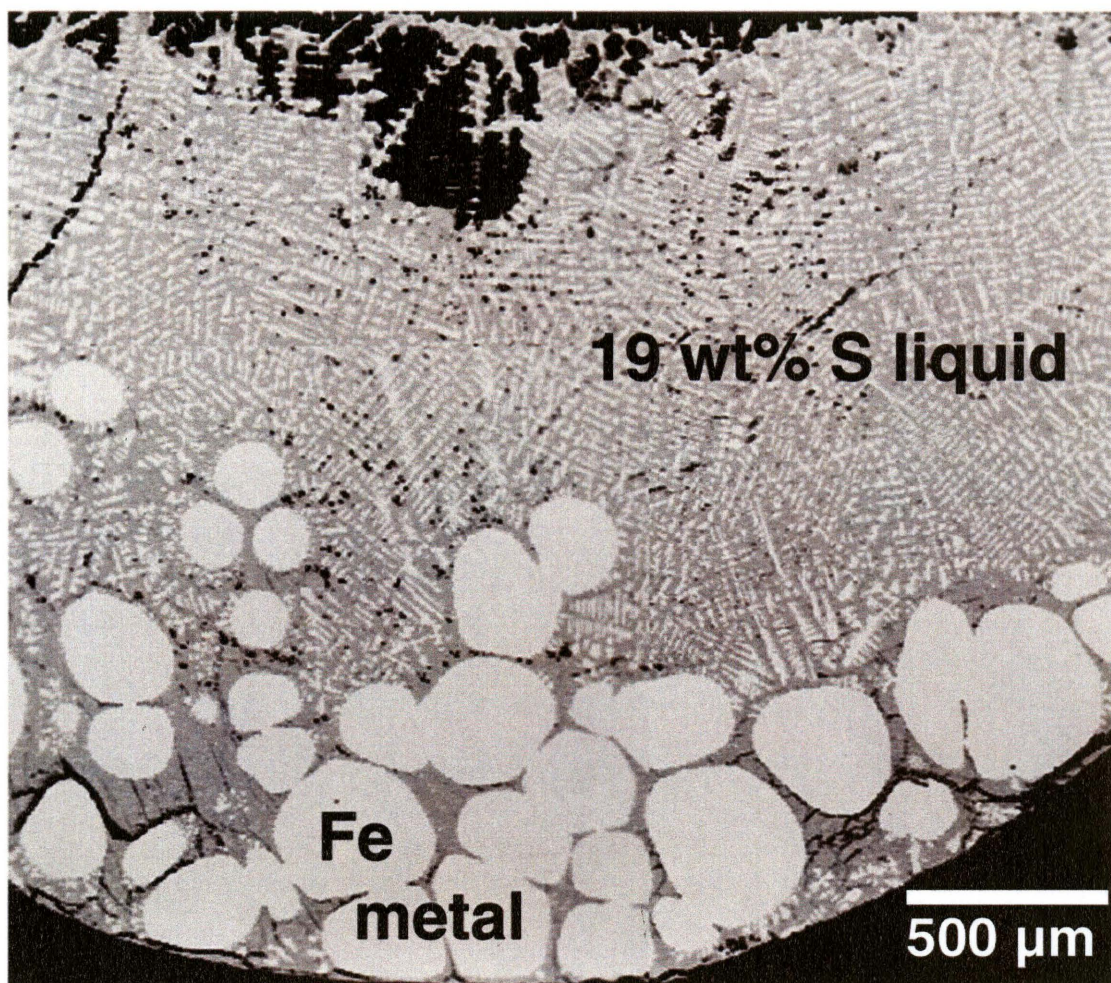
FIG. 4.1. A BSE image of a typical quenched run product from a S-bearing experiment is shown. Solid metal is homogeneous Fe, but the S-bearing liquid did not quench to a single phase. The S-bearing liquid is composed of Fe dendrites surrounded by FeS.

TABLE 4.1. Runs examining the effect of S on partitioning.

T (°C)	Duration	Ag, Pd (wt%)	S (wt%)	D(met./liq.)
Ag				
1150	7 days	1.3±0.8	31.4±1.0	0.01±0.01
1270	3 days	1.1±0.4	28.4±1.2	0.02±0.01
1350*	24 hrs	1.9±0.7	28.9±1.2	0.03±0.01
1350	36 hrs	2.4±0.5	26.5±1.1	0.02±0.01
1375*	22 hrs	1.4±0.5	18.9±1.2	0.04±0.02
1400*	12 hrs	0.8±0.3	7.9±1.4	0.09±0.03
1430*	6 hrs	0.6±0.2	5.7±1.0	0.13±0.04
1455*	3 hrs	0.5±0.2	3.4±0.7	0.21±0.06
Pd				
1150	7 days	2.1±0.3	31.0±1.1	1.7±0.3
1150	10 days	0.18±0.04	31.2±1.2	2.0±0.5
1150	10 days	0.02±0.01	32.3±1.2	2.1±0.4
1270	3 days	2.4±0.2	25.4±0.9	1.1±0.1
1350	24 hrs	2.7±0.1	19.0±1.0	0.80±0.09
1350	36 hrs	2.9±0.1	17.3±0.9	0.64±0.08
1375	22 hrs	3.3±0.1	9.5±1.2	0.52±0.02
1400	12 hrs	2.8±0.1	5.4±1.0	0.48±0.02
1400	14 hrs	0.30±0.02	7.2±1.4	0.47±0.04
1400	14 hrs	0.03±0.01	9.3±1.6	0.49±0.07
1450	3 hrs	3.5±0.1	2.9±0.6	0.50±0.02

Metallic liquids contained wt% S and wt% Ag or Pd as tabulated. The remainder of the metallic liquid was composed of Fe. A * denotes the run product consisted of Fe metal, S-bearing metallic liquid, and Ag liquid. All other runs contained only Fe metal and S-bearing metallic liquid.
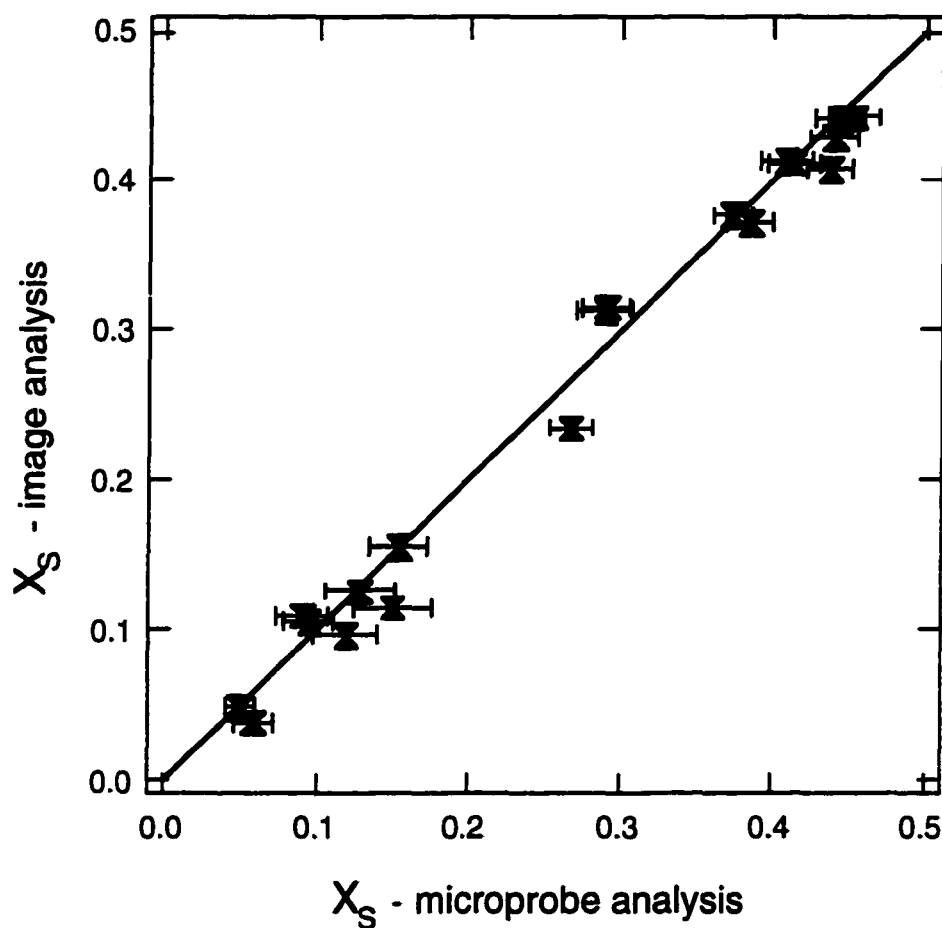
FIG. 4.2. The molar concentration of S in the two-phase quenched liquid (X_S) was determined by two independent methods. In one method, 50-100 16 μm raster beam electron microprobe measurements were averaged, giving a bulk S concentration for the liquid. In the second method, a BSE image of the liquid was processed to determine the ratio of dendrites to interstitial material and calculate the S-content of the liquid. The methods produced similar results, as shown by the one-to-one agreement on the graph.

liquid and are derived from twice the standard deviation of the mean of the microprobe analysis of the metallic liquid and twice the standard deviation of the solid metal analysis.

Using low magnification BSE images of the two-phase quenched liquid, the S-content of the metallic liquid was independently confirmed by an image processing technique. Each pixel of the image was classified as either Fe dendrite or interstitial FeS. By calculating the percentage of the image composed of dendrites and by using a molar volume ratio of FeS/Fe of 2.6, the molar concentration of S in the metallic liquid (X_S) was determined. Results from this image analysis technique and the electron microprobe raster scan agree, as shown in Fig. 4.2. This result confirms that the raster scan method of microprobe analysis accurately measures the S concentration in the two-phase quenched liquid.

4.2.2 Examining the Effect of P

The effect of the P-content of the metallic liquid on the solid metal/liquid metal weight ratio partition coefficient of Ag, Pd, Re, and Os was examined using similar experimental and analytical techniques as were used to conduct the S-bearing experiments. Around 200 mg of mixtures of Fe and P doped with either Ag and Os or Pd and Re at a few weight percent level were contained in alumina crucibles. The parent-daughter isotope elements were not both contained in the same experiments to avoid interferences between their peaks during microprobe analysis. The alumina crucibles were sealed in evacuated silica tubes and run at temperatures of 1150°C-1350°C in a vertical Deltech furnace. Run durations varied from one to nine days, depending on the temperature, and runs were quenched in water. Table 4.2 lists the experiments and the run conditions.

Figure 4.3 shows a BSE image of a typical run product. The solid metal formed many large rounded shapes while the metallic liquid quenched to Fe dendrites surrounded by Fe_3P. Due to the dendritic texture, a 16 μm raster beam was used for all electron
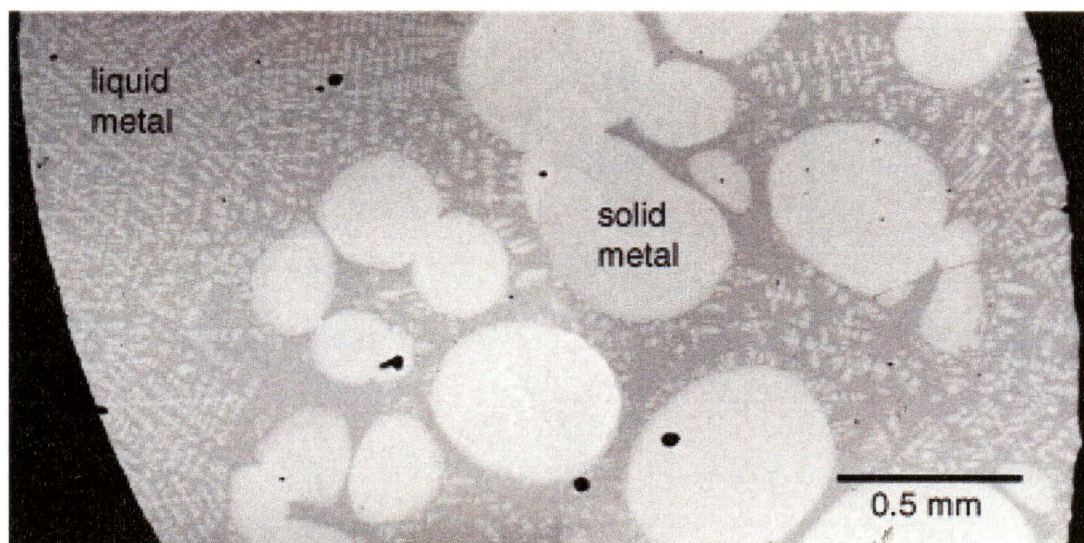
FIG. 4.3. A BSE image of run #P11 shows the solid metal phase and liquid metal phase produced by the experiments examining the effect of P on partitioning behavior. The metallic liquid did not quench to a homogeneous phase, and instead Fe dendrites surrounded by Fe_3P were formed.

TABLE 4.2. Experimental conditions, resulting compositions, and solid metal/liquid metal partition coefficients for the experiments examining the effect of P on partitioning behavior.

Run #	P5	P9	P11		P6	P10	P12
Temp. (°C)	1400	1250	1150		1400	1250	1150
Duration	15 hrs	4 days	8 days		15 hrs	4 days	8 days
Solid (wt%)							
Fe	95.6 ±1.5	94.5 ±0.7	94.6 ±1.2	Fe	97.3 ±1.3	94.6 ±1.0	94.6 ±1.0
P	0.7 ±0.11	1.4 ±0.09	1.9 ±0.1	P	0.7 ±0.17	1.4 ±0.18	1.8 ±0.16
Pd	1.29 ±0.07	0.86 ±0.07	0.77 ±0.05	Ag	0.06 ±0.01	0.027 ±0.006	0.017 ±0.006
Re	2.55 ±0.07	2.4 ±0.18	2.8 ±0.24	Os	2.4 ±0.3	3.4 ±0.4	3.7 ±0.3
Liquid (wt%)							
Fe	92.7 ±0.6	91.0 ±0.6	89.7 ±0.5	Fe	94.7 ±0.5	91.5 ±0.6	90.5 ±0.5
P	3.3 ±0.5	6.0 ±0.6	7.5 ±0.5	P	4.3 ±0.5	6.8 ±0.6	8.7 ±0.6
Pd	2.4 ±0.18	1.56 ±0.09	1.53 ±0.06	Ag	0.2 ±0.15	0.05 ±0.02	0.05 ±0.015
Re	1.2 ±0.13	0.9 ±0.11	0.9 ±0.11	Os	0.9±0.1	1.1 ±0.15	0.8 ±0.15
D_{Pd} (solid/liq.)	0.54 ±0.05	0.55 ±0.05	0.50 ±0.04	D_{Ag}	0.3 ±0.23	0.5 ±0.23	0.3 ±0.14
D_{Re} (solid/liq.)	2.1 ±0.23	2.7 ±0.4	3.1 ±0.5	D_{Os}	2.7 ±0.5	3.1 ±0.6	4.6 ±0.9

microprobe measurements. Measurements of Fe and P were made using a 20 nA, 15 kV beam and counting for 20 sec. The trace elements of Ag, Pd, Re, and Os were measured with a 200 nA, 15 kV beam and a counting time of 60 sec. The compositions given in Table 4.2 represent the average of multiple microprobe measurements. The error for the solid metal is twice the standard deviation of multiple measurements, while the error for the metallic liquid, due to its dendritic quench texture, is twice the standard deviation of the mean of multiple microprobe analyses.

4.3 Experimental Results

4.3.1 Partition Coefficients

Solid metal/liquid metal weight ratio partition coefficients for Ag and Pd from the S-bearing experiments are summarized in Table 4.1 and shown in Fig. 4.4. The *weight* partition coefficient, D, reported in Table 4.1 and Fig. 4.4, should not be confused with the *molar* partition coefficient, denoted by k. These partition coefficient values are in good agreement with the four previous experimental results (Jones and Drake, 1986; Fleet and Stone, 1991; Jones et al., 1993), which are also plotted on Fig. 4.4. Silver shows the expected chalcophile behavior of a decreasing partition coefficient with increasing S concentration in the metallic liquid. The partition coefficient of Pd increases by a factor of 3 with increasing S concentration, and it changes from incompatible to compatible in solid metal.

There are several reasons for believing my experiments have attained equilibrium. Using point beam electron microprobe analysis, the solid metal of each run was examined for evidence of compositional gradients, but none were detected. My measured partition coefficients are also in good agreement with those reported previously. Experiments at 1150°C and 1400°C with approximately 3, 0.3, and 0.03 wt% Pd were conducted to

check that Henry's Law was obeyed. The results are plotted in Fig. 4.5, indicating Henry's Law was indeed followed and implying that equilibrium was reached.

The calculated solid metal/liquid metal partition coefficients for Ag, Pd, Re, and Os with ±2σ errors are listed in Table 4.2 and plotted against the wt% P in the metallic liquid in Fig. 4.6. Also shown in Fig. 4.6 are the predicted partition coefficients for each of the elements in the P-free system from experimental studies which have examined the partitioning as a function of the S-content of the metallic liquid (Chabot and Drake, 1997; Jones and Jurewicz, 1994).

The partition coefficients for Re and Os vary in a similar way with the P-content of the metallic liquid, both increasing with increasing P concentrations. Jones and Jurewicz (1994) determined the effect of S on the partitioning behavior of Re and Os and found the two elements behaved similarly to Ir, with the partition coefficients for both elements increasing significantly with increasing S-content of the metallic liquid. For comparison, previous experimental determinations of D_{Ir} are also plotted on Fig. 4.6 with ±2σ errors when reported (Willis and Goldstein, 1982; Malvin et al., 1986; Jones and Jurewicz, 1994), and as was noted when studying the effect of S, the partitioning behavior of Re and Os as a function of the P-content of the metallic liquid is very similar to that of Ir. However, Jones and Jurewicz (1994) were able to determine a different dependency on the S-content of the metallic liquid for Re than for Os, while, within error, the behavior of the two elements as a function of the P-content of the metallic liquid is indistinguishable.

Unlike Re and Os, the solid metal/liquid metal partition coefficients for Ag and Pd exhibit no dependency on the P-content of the metallic liquid, as shown in Fig. 4.6. The similar effect of P on the behavior of Ag and Pd is in contrast to the effect S has on the partitioning of these two elements, since increasing S-content of the metallic liquid causes
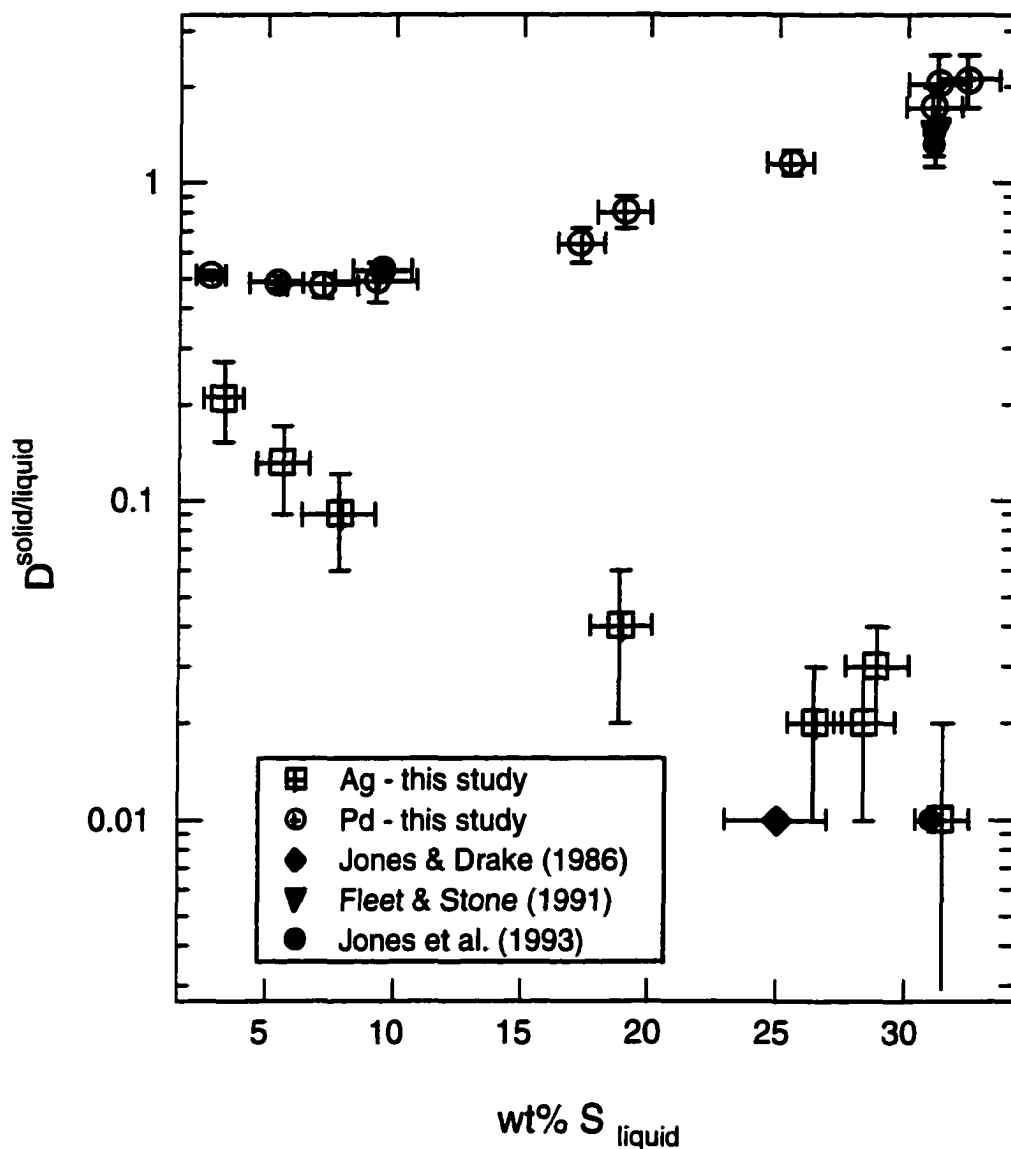
FIG. 4.4. Experimental solid metal/liquid metal weight ratio partitioning results (D) as a function of the S-content of the metallic liquid for Ag and Pd are plotted along with previous results. The partition coefficient for Ag decreases by over an order of magnitude with increasing S concentrations in the liquid. The partition coefficient for Pd increases with increasing S-content of the metallic liquid and changes from incompatible to compatible in solid Fe-metal. Errors are derived from twice the standard deviation of the mean of the microprobe analysis.
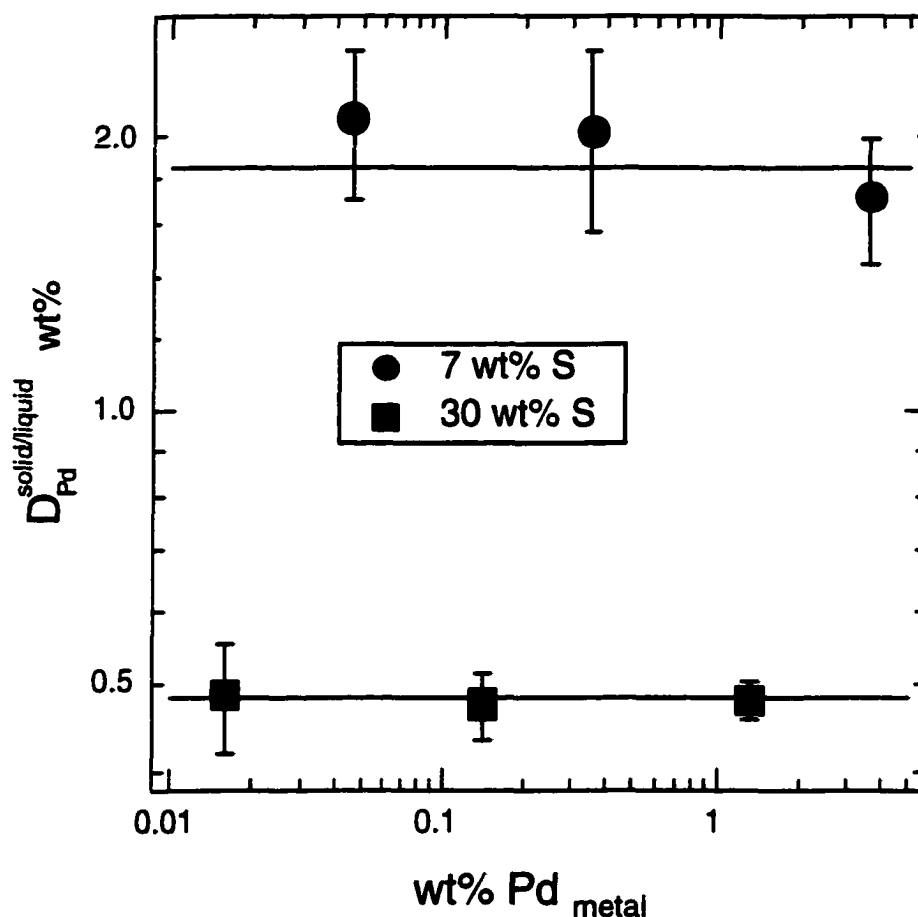
FIG. 4.5. Two sets of experiments with three runs each indicate Henry's Law was obeyed. The plot shows the repeatability of the weight ratio partition coefficient for Pd (D_{Pd}) despite the Pd concentration in the solid metal varying by two orders of magnitude. The two sets of experiments were also conducted at substantially different S concentrations of the metallic liquid. Compliance with Henry's Law, the lack of observed compositional gradients in the solid metal, and the agreement between my results and previous studies all suggest run products represent equilibrium conditions.
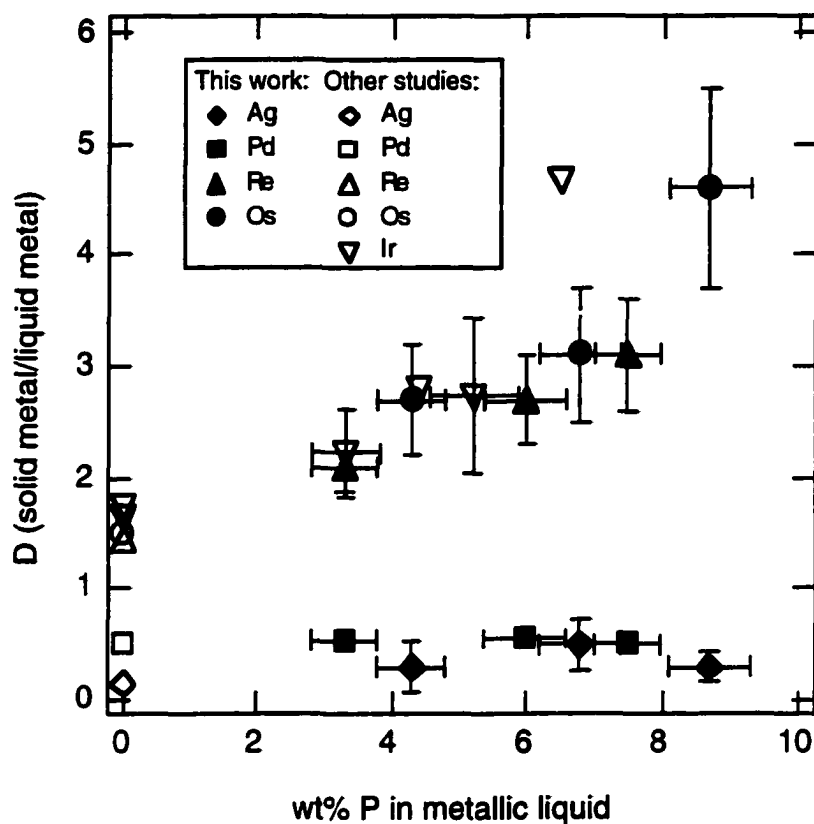
FIG. 4.6. The solid metal, liquid metal partition coefficients for Ag, Pd, Re and Os are plotted against the wt% P in the metallic liquid. Predictions of the partitioning behavior in the P-free system from other experimental studies are also shown (Jones and Jurewicz, 1994; Chabot and Drake, 1997). Both Re and Os exhibit partitioning behavior similar to that of Ir (Willis and Goldstein, 1982; Malvin et al., 1986; Jones and Jurewicz, 1994), increasing their compatibility in solid metal with increasing P-content of the metallic liquid. Silver and Pd show no change in their partitioning behavior with changing P-content of the metallic liquid.

D_{Pd} to increase but D_{Ag} to decrease. The partition coefficient for Pd in all the experiments is about 0.5, which is the same value predicted in the S-free, P-free system shown by the intercept on Fig. 4.4. The partition coefficient calculated for Ag has larger error bars than D_{Pd} due to the low concentration of Ag in the experiments. Starting mixtures contained a few wt% Ag, but because Ag is slightly volatile, significant Ag loss was experienced during the experiments. Within the error bars, D_{Ag} also shows no variation with the P concentration in the metallic liquid. Extrapolating a non-linear fit to the Ag data of Fig. 4.4, a value of D_{Ag} in the P-free, S-free system of about 0.3 is in good agreement with the value obtained in the P-bearing experiments.

4.3.2 Parameterization of Partition Coefficients

Jones and Malvin (1990) formulated a model for the effect of S and P on solid metal/liquid metal trace element partitioning. They found solid metal/liquid metal partitioning behavior to be a weak function of temperature and a strong function of the composition of the metallic liquid. They also assumed that changes in the activity coefficient of the solid were negligible compared to changes in the activity coefficient of the liquid. Thus, they were able to express the molar solid metal/liquid metal partition coefficient (k(E)) for a trace element E as a function of only the activity coefficient (γ_{Eliq}) of the partitioning element in the liquid phase:

$$\ln[k(E)] = \ln[\gamma_{Eliq}] + C \qquad\qquad \text{Eq. 4.1}$$

For eight elements exhibiting distinctly different chemical behavior in metallic systems, good fits to the experimental partitioning data were obtained when the activity coefficient in the Fe-Ni-S system was expressed as follows:

$$\ln[\gamma_{Eliq}] = \beta_S \ln[1 - 2(1.09)X_S] \qquad\qquad \textbf{Eq. 4.2}$$

where X_S is the molar concentration of S in the metallic liquid, and if FeS is assumed to be the nonmetal species, the quantity $[1 - 2 X_S]$ is the free Fe in the system. The factor of 1.09 was obtained through empirical linear regressions on the experimental data, and the constant, β_S, is specific to the element of interest.

Similarly, good fits to the experimental partitioning data of four elements were obtained when the activity coefficient in the Fe-Ni-P system was expressed as follows:

$$\ln[\gamma_{Eliq}] = \beta_P \ln[1 - 4(1.36)X_P] \qquad\qquad \textbf{Eq. 4.3}$$

where X_P is the molar concentration of P in the metallic liquid. The factor of 4 arises from assuming Fe_3P is the nonmetal species, and the factor of 1.36 was obtained through linear regressions on the experimental data of the four elements. The quantity β_P is specific to the element E.

Using this parameterization, the partitioning results are plotted in Fig. 4.7 for Ag and Pd and Fig. 4.8 for Re and Os. Both figures define linear trends, as predicted by the equations of Jones and Malvin (1990). Thus, the molar value partition coefficients may be expressed mathematically as a function of the molar concentration of S and P in the metallic liquid:

$$\ln k(Ag) = 0.772 \ln[1 - 2(1.09)X_S] - 1.917 \qquad\qquad \textbf{Eq. 4.4}$$

$$\ln k(Pd) = -0.506 \ln[1 - 2(1.09)X_S] - 0.723 \qquad\qquad \textbf{Eq. 4.5}$$
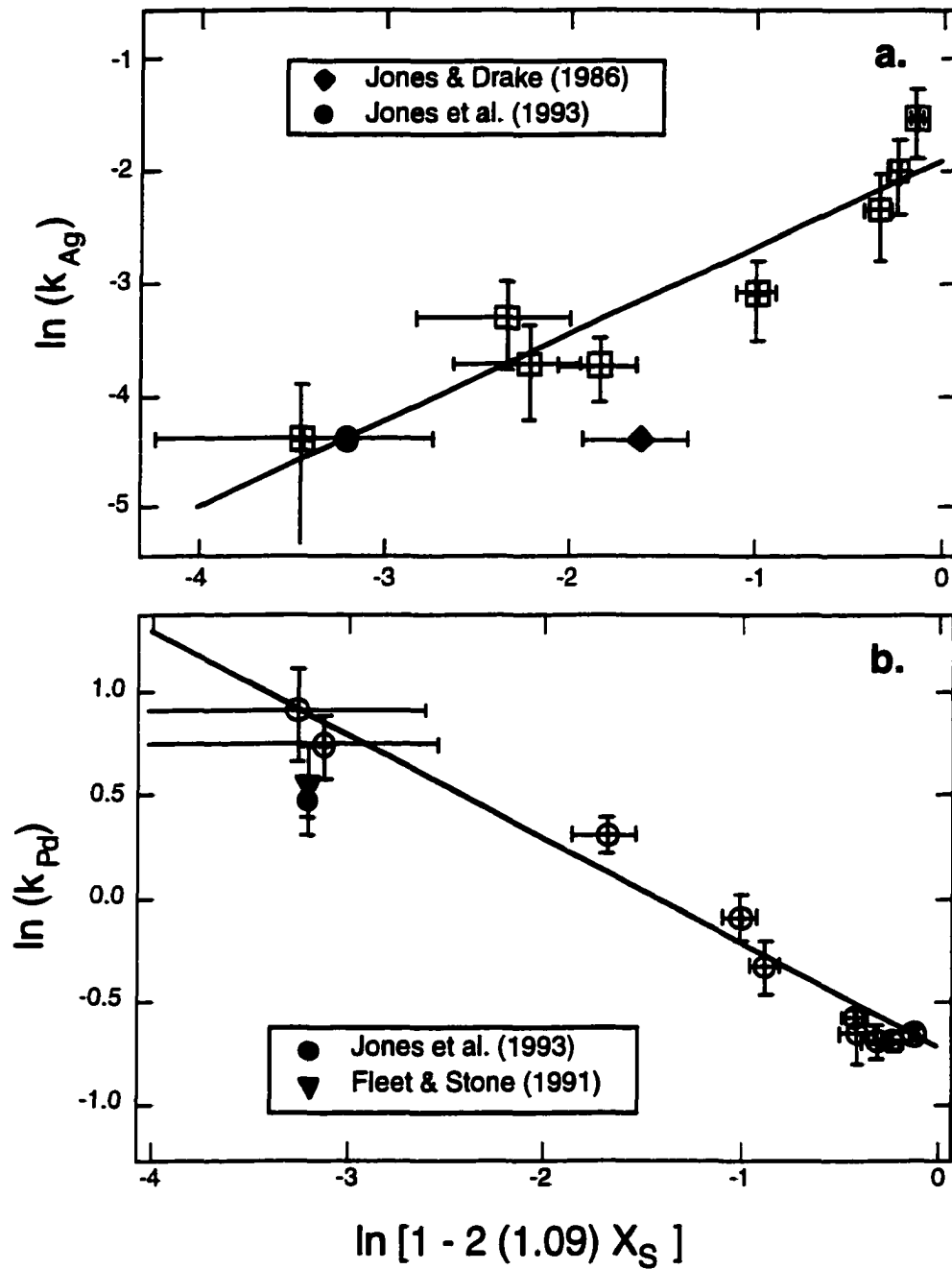
FIG. 4.7. (a) The molar solid metal/liquid metal partition coefficient for Ag (k(Ag)) is given as a function of the molar S concentration in the metallic liquid (X_S) by the equation: ln k(Ag) = 0.772 ln [1 - 2 (1.09) X_S] - 1.917. (b) The solid metal/liquid metal molar partition coefficient for Pd (k(Pd)) is given as a function of the molar S concentration in the liquid (X_S) by the equation: ln k(Pd) = -0.506 ln [1 - 2 (1.09) X_S] - 0.723.
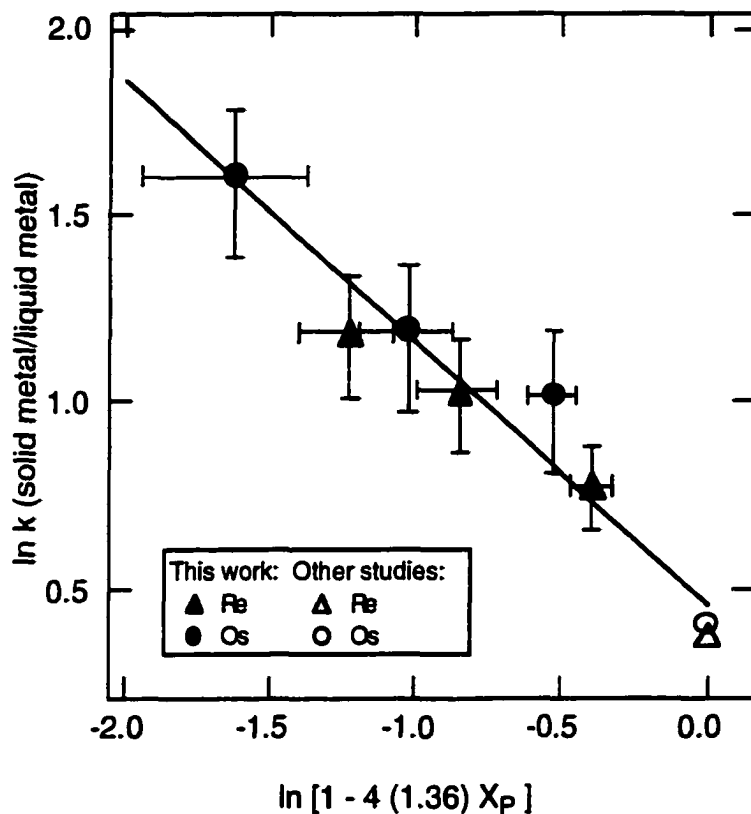
FIG. 4.8. The molar solid metal, liquid metal partition coefficients for Re and Os, k, are plotted as functions of the molar concentration of P in the metallic liquid, X_P. Using the parameterization of Jones and Malvin (1990), the experimental data for both Re and Os can be fit by the same expression: $\ln k = -0.7\ln[1-4(1.36)X_P]+0.46$.

$$\ln k(\text{Re}) = \ln k(Os) = -0.7\ln[1 - 4(1.36)X_P] + 0.46 \qquad \textbf{Eq. 4.6}$$

Using Eq. 4.4, the value predicted for Ag in the S-free, P-free system is 0.15, about a factor of 2 lower than the measured partition coefficient in the P-bearing experiments. However, a non-linear fit on the graph of D_{Ag} versus wt% S shown in Fig. 4.4 suggests the intercept at 0 wt% S appears to be closer to 0.3, in good agreement with the partitioning values obtained in the P-bearing experiments. This, perhaps, suggests the parameterization method of Jones and Malvin (1990), though useful for expressing the general solid metal/liquid metal partitioning behavior, may have difficulties fully capturing the dependency of the partition coefficient on the S and P concentrations in the metallic liquid.

4.3.3 Silver Immiscibility

In some of the Ag-bearing runs, quenched products included not only solid Fe-metal and metallic S-bearing liquid but also small amounts of a second liquid. This liquid was determined from microprobe analysis to be over 99% pure Ag. Experiments in which Ag liquid was observed are noted on Table 4.1, and a BSE image is shown in Fig. 4.9.

My experimental compositions presented here differ substantially from predictions of the published Ag-Fe-S phase diagrams (Schmid, 1988; Raghavan, 1988; Taylor 1970b), as shown in Fig. 4.10. Though the Ag-Fe-S system has been studied (Taylor, 1970a; 1970b), few previous experiments have been conducted at high temperatures with Ag-poor bulk compositions. The data that are available in this region of the system are attributed to Lüder (1924), and all of the mentioned phase diagrams are based on this work.
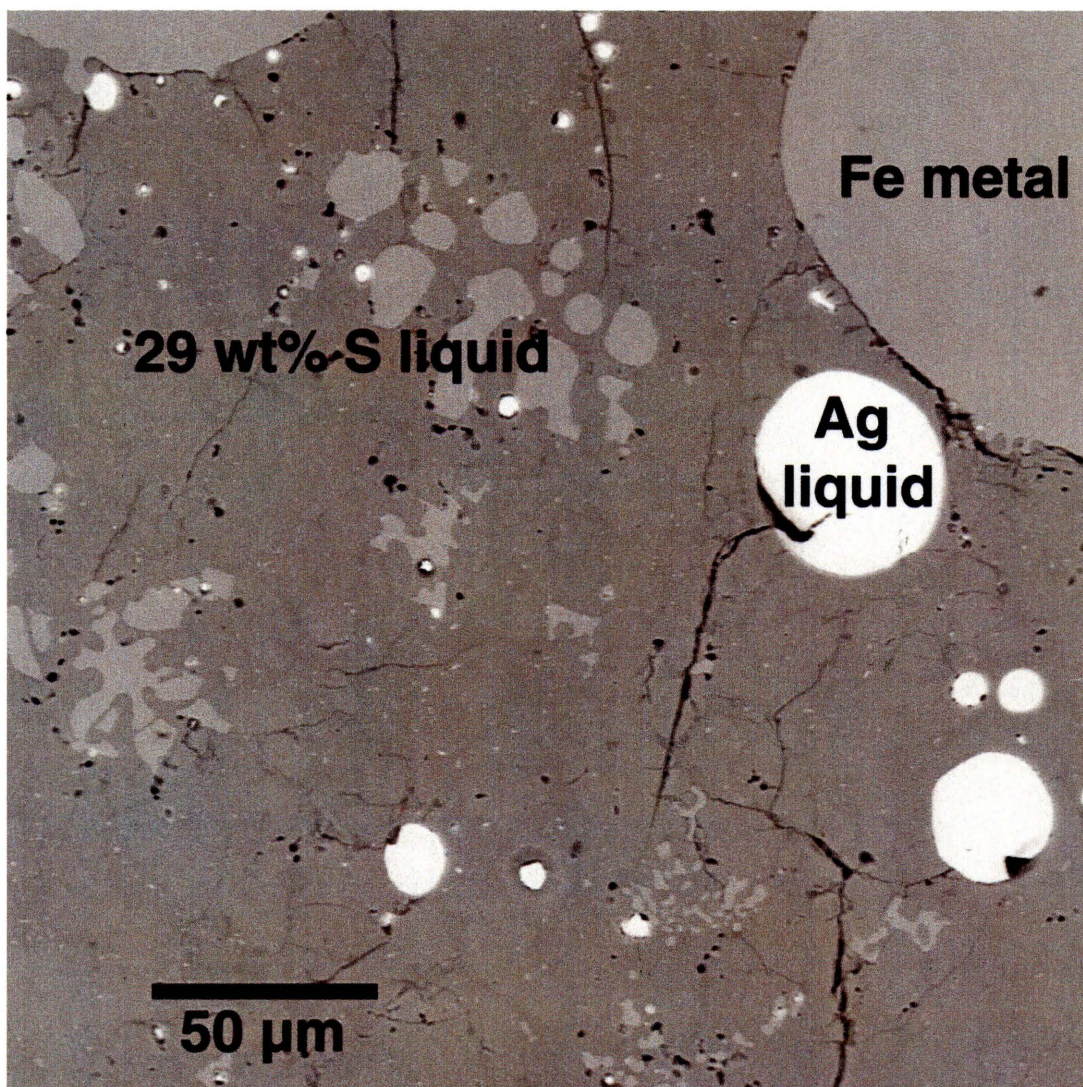
FIG. 4.9. A BSE image illustrates the three phase field of Fe-metal, S-bearing liquid, and Ag liquid. A bulk composition of only a few wt% Ag resulted in a three phase run product, and such experiments are marked on Table 4.1. Published Ag-Fe-S ternary diagrams are not consistent with this result.
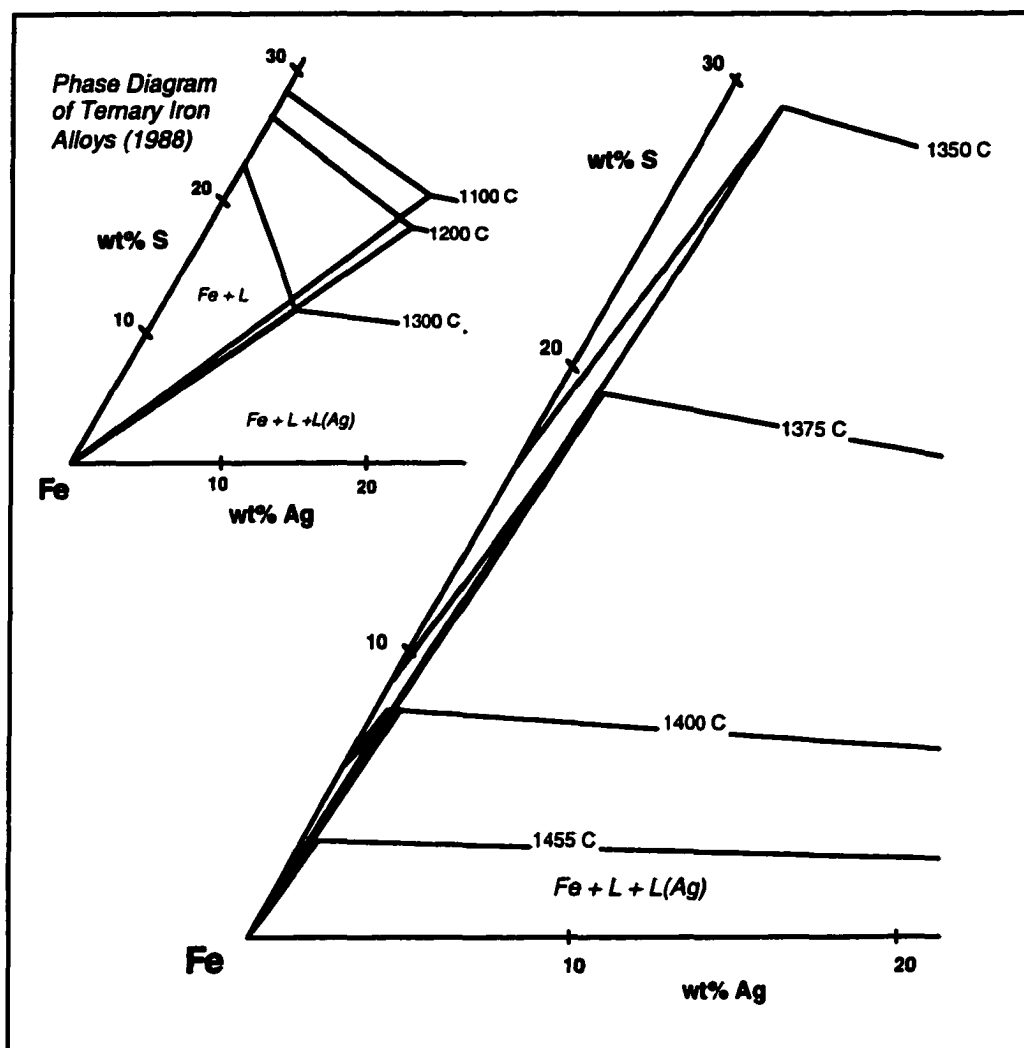
FIG. 4.10. The Ag-poor corners of two ternary diagrams are shown. The upper smaller diagram shows three isotherms from Raghavan (1988). Raghavan attributes the shape of the solid Fe and S-bearing liquid two phase field to the experiments conducted by Lüder (1924). The larger ternary diagram plots four isotherms from my Ag partitioning experiments. My results show a significantly smaller solid Fe and S-bearing liquid two phase field, with only a few wt% Ag driving the equilibrium product into the three phase field of solid Fe, S-bearing liquid, and Ag liquid. The S-content of the S-bearing liquid produced in my experimental three phase field is also very different from that of Raghavan (1988); I find the S-content of the liquid is increased over the value in the Ag-free binary system while Raghavan (1988) illustrates the opposite.

Specifically, I find the two phase field of Fe metal and S-bearing liquid is much smaller than previously reported. A bulk composition with only a few wt% Ag is enough to produce a three phase field of Fe metal, S-bearing liquid, and Ag liquid. This point is illustrated on the ternary diagrams of Fig. 4.10. Three previously predicted isotherms (1100, 1200, and 1300°C) are shown as well as four isotherms derived from my Ag partitioning experiments.

The other major difference between my Ag experimental results and those reported previously is the S concentration of the S-bearing liquid in the three phase field. I find the S concentration of the S-bearing liquid is considerably higher than in the Ag-free Fe-S binary system. This is shown on Fig. 4.11, and could make thermodynamic sense due to the highly incompatible behavior of Ag in Fe. If the amount of Ag is increased in the S-bearing liquid, more S could also be needed to effectively "screen" Ag from Fe and allow the increased amount of Ag to "fit" in the liquid. Such reasoning is consistent with my results but inconsistent with currently published diagrams which show the opposite effect, a lower S-content in the S-bearing liquid in the three phase field than in the Ag-free binary system.

The experiments of Lüder, on which the currently published phase diagrams are based, used much larger samples and compositional analysis was determined through visual inspection. I have strong evidence, such as the lack of compositional gradients in the solid metal and the Henrien behavior previously discussed, that equilibrium was obtained in my experiments. Attaining equilibrium may have been more difficult with large samples. Also visual analysis is almost certainly subject to greater uncertainty than microprobe analysis.

Along with the difficulties of attaining equilibrium with large samples and determining compositions through visual analysis, Lüder's experiments were conducted in tightly closed crucibles at atmospheric pressure. The actually oxygen fugacity during Lüder's

experiments is not well-defined. Regardless, this experimental method most likely produced a higher oxygen fugacity than my experiments run in evacuated and sealed silica tubes. At the interface between my alumina crucibles and my samples, pure hercynite was observed. The oxygen fugacity of my experiments is thus defined by the following reaction:

$$2Al_2O_3 + 2Fe + O_2 \rightarrow 2FeAl_2O_4$$
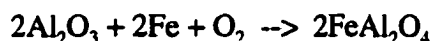
Malvin et al. (1986) conducted similar experiments in sealed silica tubes which, by phase diagram predictions, should have contained immiscible liquids, but the experiments showed no signs of immiscibility. When the same experiments were run under flowing Ar-H$_2$, immiscible liquids were evident in the run products, and Malvin et al. concluded that even an oxygen fugacity near the iron-wüstite buffer can suppress liquid immiscibility. If the experiments of Lüder were indeed conducted at a higher oxygen fugacity than my experiments, this could explain the much larger two phase field of solid Fe-metal and S-bearing liquid attained from Lüder's work than from my experimental results, as shown in Fig. 4.10. A higher oxygen fugacity could increase the solubility of Ag in the S-bearing liquid and suppress any liquid immiscibility until higher concentrations of Ag.

Thus, though it is surprising to find that a low concentration of Ag has such a significant effect, I have good agreement between multiple Ag partitioning experiments on the shape and composition of the fields, strong evidence that equilibrium was obtained in my experiments, and a good indication of the oxygen fugacity of my experiments. My experiments show that published Ag-Fe-S ternary diagrams do not accurately display the Fe-metal and S-bearing liquid field; the ternary diagram should be refined as shown in Fig. 4.10.
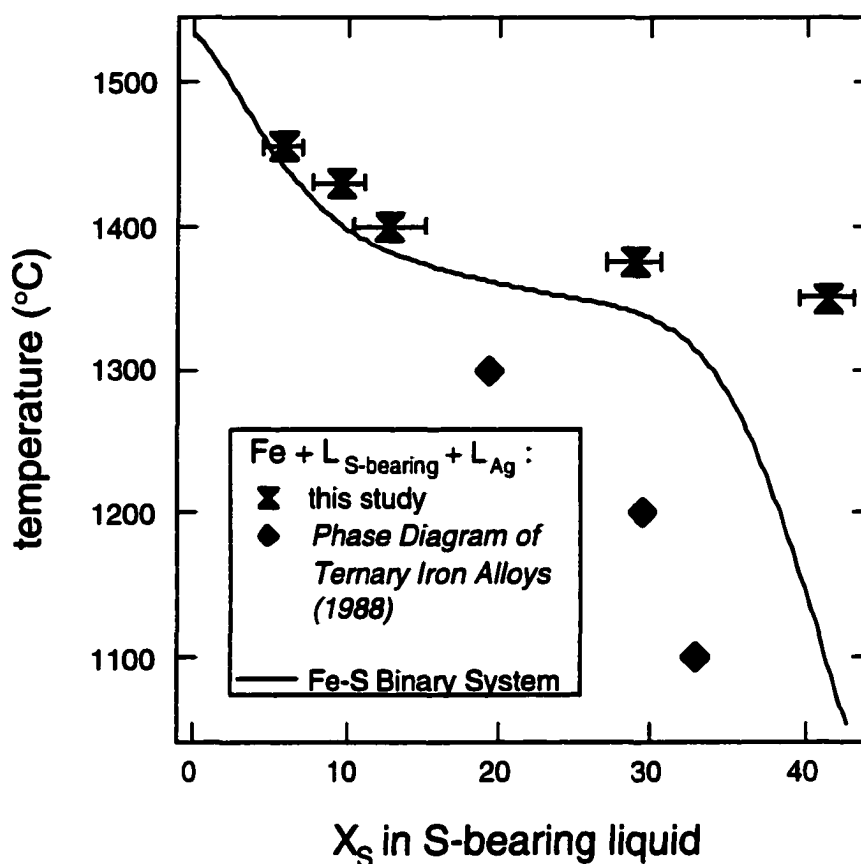
FIG. 4.11. The molar concentration of S in the liquid (X_S) is plotted against the run temperature for my experiments which contained three phases. For reference, the binary Fe-S system is shown as a solid line in the diagram, and in all cases, the S-bearing liquid produced in my experiments in the three phase field has a higher S-content than the Ag-free system for a given temperature. Due to the highly incompatible behavior of Ag in Fe metal, such an increase in the S-content of the liquid could be expected; if the amount of Ag is increased in the liquid, more S could also be needed to "screen" that Ag from Fe. Published diagrams, based on Lüder (1924), show the opposite, that lower S concentrations are present in the liquid from the three phase field than in the S-bearing liquid in the Ag-free binary system.

4.4 Discussion

4.4.1 Meteorite Crystallization Trends

Chen and Wasserburg (1996) found no correlation between Ag and Ni abundances in iron meteorites, though they did find, for all iron meteorite groups, the concentration of Ag relative to Ni was significantly depleted compared to the solar abundance ratio. Therefore, the Ag concentrations in only a few iron meteorites have been measured due to these low concentration levels (ppb or lower values).

However, there is a positive correlation between Pd and Ni abundances for many groups of iron meteorites. These trends are commonly attributed to the crystallization history of a metallic core in the meteorite parent body (Scott, 1972). The positive correlation suggests that Pd, like Ni, is enriched in the metallic liquid as the solid Fe-Ni core crystallizes. This correlation is inconsistent with the limited previous experimental Pd solid metal/liquid metal partitioning results (Fleet and Stone, 1991; Jones et al., 1993) which suggest Pd is slightly compatible in the crystallizing solid metal.

As I have shown, solid metal/liquid metal partition coefficients for Pd are sensitive to the S-content of the metallic liquid and P has no effect on the partitioning behavior. It has been illustrated experimentally that the C content of the metallic liquid can also affect the partitioning behavior (Willis and Goldstein, 1982; Narayan and Goldstein, 1982), but the amount of C in crystallizing asteroidal cores is believed to be much less than the concentration of S or P. Thus, only considering the influence of S on Pd partitioning in iron meteorites is probably a very minor approximation. By taking into account the changing partitioning behavior of Pd with the changing S-content of the metallic liquid, Pd crystallization trends can now be modeled successfully, suggesting my approximation is acceptable for the simple model I'm using.

Simple fractional crystallization was modeled numerically as equilibrium crystallization in small discrete steps. The equations for equilibrium crystallization are derived from the principle of mass balance and the definition of the partition coefficient:

$$C_{lf} = \frac{C_{li}}{[1 - F_L + DF_L]}$$

Eq. 4.7

$$C_S = \frac{C_{li}D}{[1 - F_L + DF_L]}$$

Eq. 4.8

where C_{li} is the initial concentration of an element in the liquid at the beginning of a crystallization step, C_{lf} is the final concentration of that element in the liquid after a crystallization step, and C_S is the resulting concentration of the element in the solid metal phase for each crystallization step. D is the solid metal/liquid metal partition coefficient, and F_L is the mass fraction of the liquid that crystallizes to solid metal in each step. The initial liquid concentration, C_{li}, should not be confused with the original, starting concentration, C_{Lo}. Since simple fractional crystallization was modeled as equilibrium crystallization in small steps, C_{li} is updated before each crystallization step while C_{Lo} is a constant referring just to the starting composition.

Calculations were carried out in equal mass steps, with an average value for F_L of approximately 10^{-4}. To model simple fractional crystallization, after C_{lf} and C_S are calculated for each crystallization step according to the equations just given, the resulting C_{lf} becomes the C_{li} for the next step.

The partitioning behavior of Pd parameterized in Eq. 4.5 and converted from a molar to a weight value was used as D_{Pd}. The expression for D_{Ni} is taken from Jones and Malvin (1990):

$$\ln k(Ni) = -0.339 \ln[1 - 2(1.09)Xs] - 0.101 \qquad \text{Eq. 4.9}$$

and was also converted to a weight value. A solid metal/liquid metal weight partition coefficient for S of 0.01 was used. This value is the average value observed in my experimental runs.

The initial concentrations of Ni and S in the model affect the resulting trends. Jones and Drake (1983), Haack and Scott (1993), and Scott et al. (1996) have previously optimized the starting values of Ni and S for the IIAB, IIIAB, IVA, and IVB magmatic iron meteorite groups. These starting concentrations for each meteorite group were determined by matching the crystallization trends of many elements. Because any model of Pd crystallization trends must also be consistent with the trends observed for other elements of the same group, all modeling calculations began with these previously reported starting concentrations for S and Ni.

Thus, with this simple fractional crystallization model, the abundances of Pd relative to Ni for the IIAB, IIIAB, IVA, and IVB magmatic iron meteorite groups are, in general, modeled successfully, as shown in Fig. 4.12. Starting and final liquid concentrations of S, Ni, and Pd for each iron meteorite group are given in Table 4.3. The percentage of the original liquid which crystallizes to produce the trends seen in Fig. 4.12, referred to as the degree of crystallization, is also given in Table 4.3.

However, only examining abundance correlations relative to Ni can be deceiving because, throughout the crystallization process, the solid metal/liquid metal partition coefficient of Ni is very nearly unity. The resulting lack of a large dynamical range of Ni concentration values effectively hides smaller changes in the general element correlation trends. Fig. 4.13 shows Pd abundances for the IIIAB iron meteorite group plotted against Ir abundances, instead of Ni abundances. In contrast to the behavior of Ni, the solid
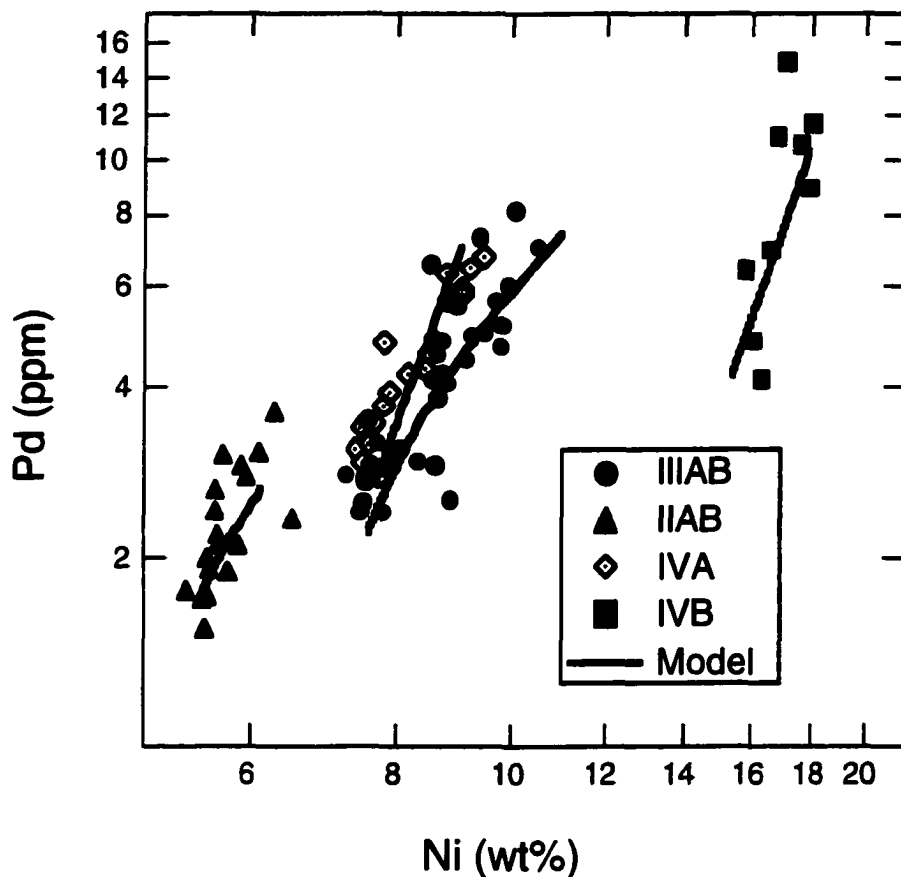
FIG. 4.12. IIIAB, IIAB, IVA, and IVB iron meteorite groups show a definite correlation between Pd and Ni abundances. A simple fractional crystallization model which uses partition coefficients dependent on the S-content of the metallic liquid reproduces the correlations for each iron meteorite group. Model calculations are shown as a solid line. Palladium abundance data are from Chen and Wasserburg (1996), Hoashi et al. (1993), Mermelengas et al. (1979), Nichiporuk and Brown (1965), and Smales et al. (1967). Nickel abundance data are from Graham et al. (1985), Hoashi et al. (1993), Jarosewich (1990), Kracher et al. (1980), Malvin et al. (1984),Scott et al. (1973), and Scott and Wasson (1976).

TABLE 4.3. Model starting conditions and results for fractional crystallization calculations.

Iron Group		Ir * (ppm)	Ni * (wt%)	P * (wt%)	Pd (ppm)	S * (wt%)	Degree of crystallization
IIIAB	starting	3.5	7.6	0.3	4.0	12.0	59%
	final	0	6.6	0.4	4.9	29.1	
IIAB	starting		5.1		2.7	17.0	29%
	final		4.8		2.9	23.9	
IVA	starting		8.4		6.0	2.5	78%
	final		9.2		13.0	11.0	
IVB	starting		17.0		9.6	0	79%
	final		20.0		23.9	0	

* Conditions were from Jones and Drake (1983), Haack and Scott (1993), and Scott et al. (1996).
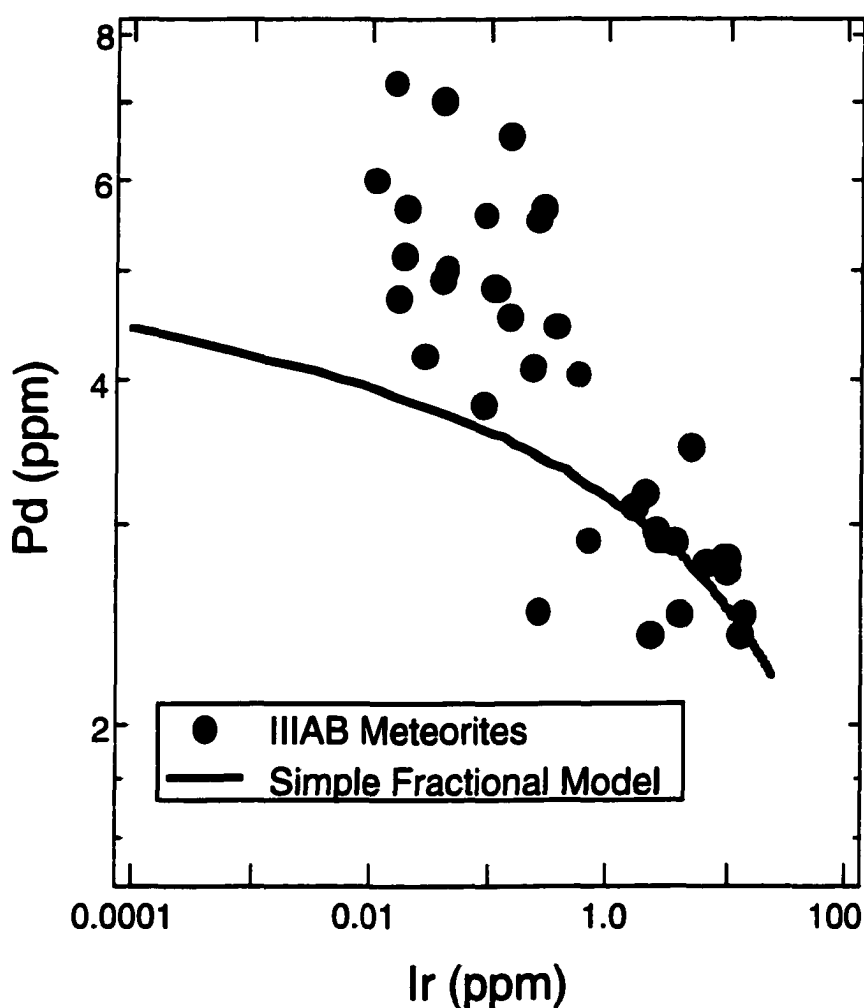
FIG. 4.13. The abundances of Pd relative to Ir are plotted for the IIIAB iron meteorite group. The simple fractional crystallization model which fit Pd vs. Ni trends well in Fig. 4.12, shown as a solid line, fails to match the more complex Pd vs. Ir trend. This lack of agreement illustrates that only examining elemental trends relative to Ni abundances can be deceiving. It also suggests a more complex formation history than just simple fractional crystallization for at least the IIIAB group. Iridium abundance data are from Kracher et al. (1980), Malvin et al. (1984), Scott et al. (1973), and Scott and Wasson (1976).

metal/liquid metal partition coefficient of Ir varies considerably during the crystallization process and most often has a value far from unity. Consequently, as seen in Fig. 4.13, Ir abundances for the IIIAB group range over three orders of magnitude, showing a more complex correlation between the two elements than seen in Fig. 4.12.

The general IIIAB trend of Fig. 4.12 is modeled fairly well by simple fractional crystallization, but simple fractional crystallization fails to match the more detailed and complex correlation between Ir and Pd shown in Fig. 4.13. The simple fractional crystallization trend in Fig. 4.13 was calculated using the numeric model described previously, the partition coefficients for Ir and P from the parameterizations of Jones and Malvin (1990), and the starting concentrations given in Table 4.3. While Pd abundance data in meteorites is not as diagnostic as Ga, Ge, or Ir abundances for comparing models, Fig. 4.13 does serve to show the danger of only comparing modeling results by examining element trends relative to Ni. The next chapter, Chapter 5, deals with this issue in more details and presents a crystallization model I have developed which can reproduce the trend observed in Fig. 4.13.

4.4.2 Troilite-rich Nodules

The abundances of Ag and Pd have been measured not only in the Fe-Ni metal of iron meteorites but also in troilite-rich nodules of iron meteorites; metal/bulk troilite-rich nodule partition coefficients have been determined for Ag and Pd through analysis of the composition of the troilite-rich nodule and adjacent Fe-Ni metal samples (Kaiser and Wasserburg, 1983; Chen and Wasserburg, 1983, 1990). Troilite-rich nodules are believed to represent metallic S-bearing liquid trapped during the crystallization process (Kracher and Wasson, 1982), so these observed partition coefficients should be related to experimentally determined values of solid metal/liquid metal partition coefficients.

Table 4.4 lists the available data on Ag and Pd abundances in troilite-rich nodules. If these abundances are a record of the S-bearing metallic liquid trapped during iron meteorite formation, then the observed partition coefficient should be a function of the S-content of the metallic liquid when each particular meteorite crystallized.

As discussed in the previous section, the general trends produced by the crystallization process for the IIAB, IIIAB, IVA, and IVB iron meteorite groups have been modeled fairly well by a simple fractional crystallization model and the starting compositions given on Table 4.3. Using this model, the S-content of the liquid at the time when each meteorite formed can be deduced. This is done by matching the Ni-content of each meteorite to the appropriate "step" in the model calculations for the relevant iron meteorite group. This deduced S-content represents the composition of the metallic liquid that coexisted with the crystallizing metal that has the Ni-content of interest. If troilite-rich nodules do represent liquid trapped during the crystallization process, this deduced S-content refers to the composition of the troilite-rich nodule.

This deduced S-content from the simple fractional crystallization model is shown on Table 4.4 for the five meteorites which are part of the IIAB, IIIAB, IVA, or IVB groups. The Derrick Peak meteorite has an unusually high Ni content for a IIAB (Jarosewich, 1990), which is beyond the range covered by my model calculations. Therefore, the S-content of the liquid which would result in such a high Ni value could not be determined from my simple fractional crystallization model. However, as can be seen in Fig. 4.12, the IIAB group has been well modeled. Thus, the S-content applicable to Derrick Peak is taken to be somewhere in the total range used to model the IIAB group.

Figure 4.14 shows my experimental data presented in Fig. 4.4; the solid metal/liquid metal partition coefficient of Ag is displayed against the S-content of the metallic liquid. For the five meteorites which have been modeled, the observed partition coefficient for Ag between metal/troilite-rich nodule is also plotted versus the S-content of the liquid at

the time when it was "trapped." As Fig. 4.14 shows, there is a good correlation between the observed metal/nodule and experimental metal/liquid partition coefficients for Ag. This agreement indicates that Ag abundances measured in troilite-rich nodules represent "trapped" S-bearing liquid and also explains the wide range of metal/nodule partition values observed.

However, observed metal/nodule partition coefficients for Pd do not match experimental metal/liquid values. Instead, the observed metal/nodule partition coefficients for Pd are very large and appear to be in better agreement with metal/troilite partitioning experiments (Jones et al., 1993), as shown on Table 4.4. The agreement with experimental metal/liquid partition coefficients for Ag suggests that the troilite-rich nodules did not equilibrate with the surrounding metal after being trapped, yet somehow the Pd abundances imply metal/troilite equilibrium.

Jones et al. (1993) suggested that perhaps the metal nodule wall acts as a "semipermeable membrane, allowing Pd to equilibrate with the metal while simultaneously trapping Ag." Such a theory is supported by the agreement between metal/nodule and experimental metal/liquid partition coefficients for Ag and the lack of agreement for Pd. Measured metal/nodule partition coefficients for Pd are also quite large, which is in agreement with the experimentally determined metal/troilite partition coefficient for Pd. Such a theory does not, however, offer an explanation for the range of metal/nodule partition coefficients observed for Pd; if Pd did equilibrate between metal and troilite, one partitioning value would be expected, yet multiple are observed. However, with only a few measurements for metal/nodule partitioning of Pd in iron meteorites, one measurement of the experimental metal/troilite Pd partition coefficient, and incomplete knowledge of the host phase of Pd in troilite-rich nodules, any conclusions are difficult to draw. It is clear that Pd abundances in troilite-rich nodules, unlike Ag abundances, cannot be explained by solid metal/liquid metal partitioning.

TABLE 4.4. Distribution of Ag and Pd in iron meteorite troilite-rich nodules and in experiments.

Meteorite name	Metal Ni (wt%)	Model S (wt%)	Troilite-rich nodule*	
			Ag (met/nod)	Pd (met/nod)
Cape York (IIIAB)	7.6	12	0.065	
Derrick Peak (IIAB)	6.5	17 - 24	0.024	880
Grant (IIIAB)	9.2	25	0.022	
Santa Clara (IVB)	17.9	0	0.28	
Gibeon (IVA)	7.8	3.0	0.019 - 0.175	336 - 1350
Mundrabilla			0.13	3900
Experimental				
D(met/liq)			0.01 - 0.3	0.5 - 2.0
D(met/troi)**			1.8	>110

* From Kaiser and Wasserburg (1983), Chen and Wasserburg (1983,1990).
** From Jones et al. (1993).
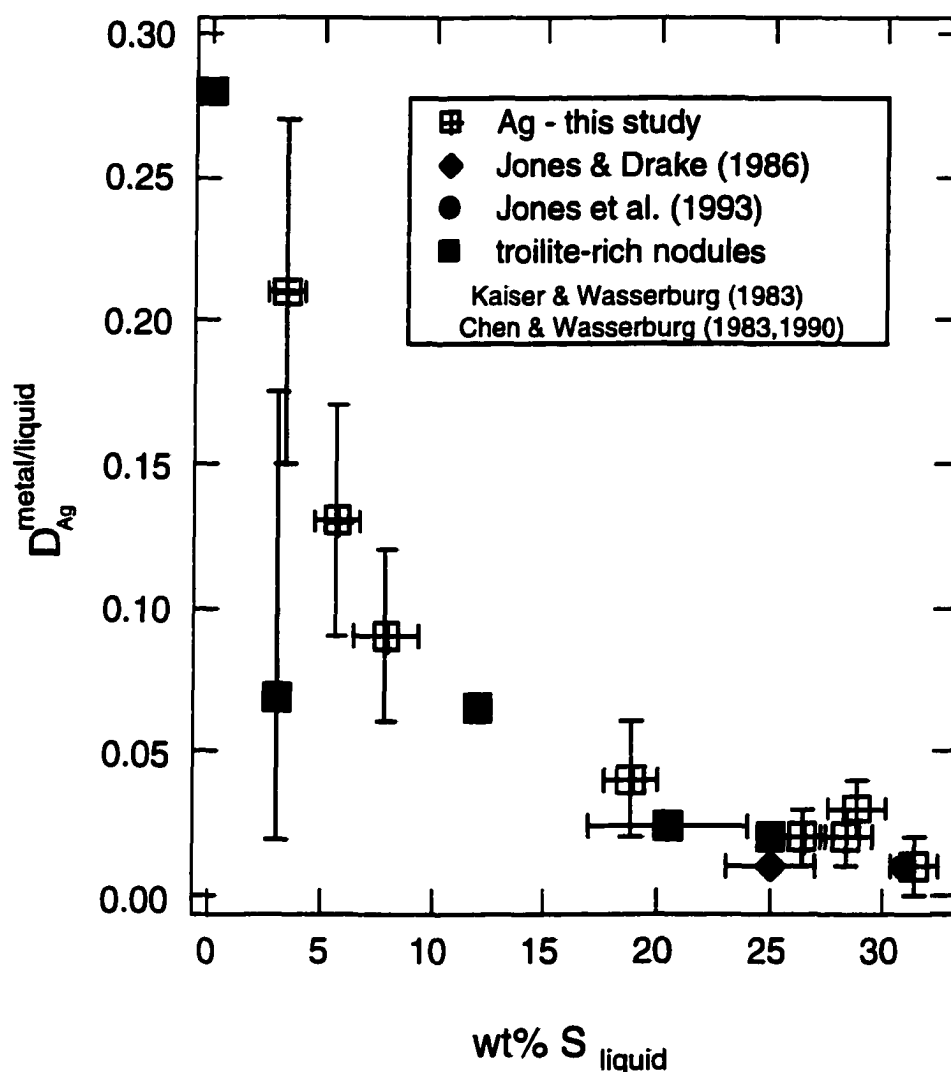
FIG. 4.14. Considerable variation is observed in measured iron meteorite metal/troilite-rich nodule Ag partitioning values. Knowing the Ni-content of each meteorite and using a simple fractional crystallization model, the S-content of the liquid at the time each nodule was "trapped" was deduced for five meteorites (shown as solid squares in the diagram) whose troilite-rich nodules have been analyzed. As can be seen on the graph, the measured metal/nodule value for Ag is consistent with experimental metal/liquid partition coefficients (shown as open squares), suggesting troilite-rich nodule abundances do represent liquid "trapped" during the crystallization process. The different S concentrations at the time of crystallization of each meteorite thus explain the observed variation in measured metal/nodule partition coefficients for Ag. However, Pd metal/nodule partition values resemble troilite/metal partitioning more closely than metal/liquid partitioning.

4.5 Summary

The S-content of the metallic liquid affects the partitioning behavior of both Ag and Pd. The solid metal/liquid metal partition coefficient of Ag decreases by over an order of magnitude with increasing S-content of the liquid, and Ag always remains incompatible in solid metal. The partition coefficient of Pd, unlike Ag, increases with increasing S-content of the liquid, changing the partitioning behavior from slightly incompatible to slightly compatible in solid metal. The behavior of both elements is consistent with Ag being chalcophile and Pd being siderophile. Phosphorus has no effect on the solid metal/liquid metal partitioning of either element. However, solid metal, liquid metal experiments show the partition coefficients for Re and Os increase with increasing P-content of the metallic liquid, a behavior very similar to that of Ir.

A simple fractional crystallization model which accounts for the changing partitioning behavior of Pd between solid metal and liquid metal as a function of the S-content of the metallic liquid explains the observed correlations in Pd and Ni abundances in iron meteorites. Such observed Pd and Ni trends are modeled successfully for the IIAB, IIIAB, IVA, and IVB iron meteorite groups. However, when Pd abundances are examined relative to an element with a larger range of concentrations, such as Ir, a more complex crystallization history than simple fractional crystallization is necessary to reproduce the observed element correlations.

Experimental solid metal/liquid metal partitioning values and observed iron meteorite metal/troilite-rich nodule abundances for Ag agree well. Fractional crystallization thus offers a natural explanation for the wide range of observed Ag metal/nodule partition coefficients. Palladium abundances, however, resemble metal/troilite partitioning values more closely than they do experimental solid metal/liquid metal partitioning experiments. A question, which still needs to be more thoroughly addressed, is how does one element

(Ag) preserve abundances in agreement with solid metal/liquid metal partitioning while the other element (Pd) does not.

CHAPTER 5

MAGMATIC IRON METEORITES AND MIXING IN THE MOLTEN CORE

As mentioned in Chapter 1, the IIIAB group is the largest of the magmatic iron meteorite groups and consequently is commonly used to test models of asteroid core crystallization. Simple fractional crystallization calculations appear to reproduce the general shape of the elemental trends observed in the IIIAB group when these trends are plotted versus Ni, as is traditionally done. However, when the elemental trends are examined versus another element, such as Ge versus Ir, simple fractional crystallization fails to match a significant portion of the trend, specifically meteorites formed during the final stages of crystallization. My simple mixing model which attempts to account for the possibility of inhomogeneities in the molten metallic core is able to reproduce the entire IIIAB trend observed. This model is a variant of simple fractional crystallization and involves mixing between a zone of liquid involved in the crystallization process and a second zone too far from the crystallizing solid to be actively involved in crystallization. This model does not suggest one unique solution for the method by which an asteroidal core crystallizes; rather it demonstrates that including the effects of mixing in the molten core can account for the observed IIIAB elemental trends, particularly the late stage crystallizing members, which other models have difficulty explaining.

5.1 Introduction and Past Work

For reasons discussed in Chapter 1, magmatic iron meteorites are believed to be pieces of metallic cores of asteroid-sized bodies that, after differentiation and solidification, were disrupted (Scott, 1972). These meteorites, when plotted by group, display well-defined trends on element versus element diagrams. The elemental trends are usually attributed to the solidification of the once molten metallic core; as the core cooled, Fe-Ni metal began to fractionally crystallize which created a range of concentrations for each element in the solid metal (Scott, 1972).

The elemental composition in the crystallizing metal depends on the partitioning behavior of each element between solid and liquid metal. The solid metal/liquid metal partition coefficient of an element E, D_E, has been found experimentally to vary as a function of the light element concentration in the metallic liquid (Willis and Goldstein, 1982; Jones and Drake, 1983). Specifically, S, P, and C can have drastic effects on the partitioning behavior. An example is D_{Ge} which increases by over two orders of magnitude from the S-free system to the Fe-FeS eutectic composition.

The magmatic iron meteorite group with the most members is the IIIAB group which is believed to contain samples from a metallic core with a radius of 10 km (Rasmussen, 1989). Consequently, this meteorite group is commonly used to test models of core crystallization in asteroid-sized bodies. Using partition coefficients from static, isothermal experiments (for reasons outlined in Malvin et al., 1986), the IIIAB elemental trends have been previously modeled by simple fractional crystallization (Willis and Goldstein, 1982; Jones and Drake, 1983; Haack and Scott, 1993;). Figure

5.1 shows the trends for Ge, Ir, and Ni resulting from a simple fractional crystallization calculation. The starting concentrations are given in Table 5.1, and the values for each D_E are listed in Table 5.2 as molar solid metal/liquid metal partition coefficients using the parameterization method of Jones and Malvin (1990). References for the IIIAB meteorite data are given in Table A1 of Haack and Scott (1993). The resulting simple fractional crystallization trends for the IIIAB iron meteorites are shown in Fig. 5.1a and Fig. 5.1b plotted against wt% Ni in the metal, as is traditionally done. Though not perfect, simple fractional crystallization is able to reproduce the range of Ir concentrations over 3 orders of magnitude as well as the characteristic turning over behavior of the Ge trend.

However, only examining meteorite trends versus Ni can be deceiving. Plots of elemental trends in iron meteorites have traditionally been plotted against Ni because of the large number of Ni measurements that have been made of iron meteorites; Ni is an easy element to measure due to its high concentration (wt% levels) in iron meteorites. Nevertheless, D_{Ni} is very close to unity throughout the crystallization process and consequently does not offer a large range of concentration values to plot against. This small dynamic range of D_{Ni} can de-emphasize changes in the shape of an elemental trend. An element such as Ir, on the other hand, has a very large dynamic range and consequently the crystallization trend is spread out in Ir concentrations over 3 orders of magnitude for the IIIAB group. Fig. 5.1c shows the same simple fractional crystallization calculations as Fig. 5.1a and Fig. 5.1b, but with Ge plotted against Ir. Though there is scatter in the trend and some meteorites classified as IIIAB differ
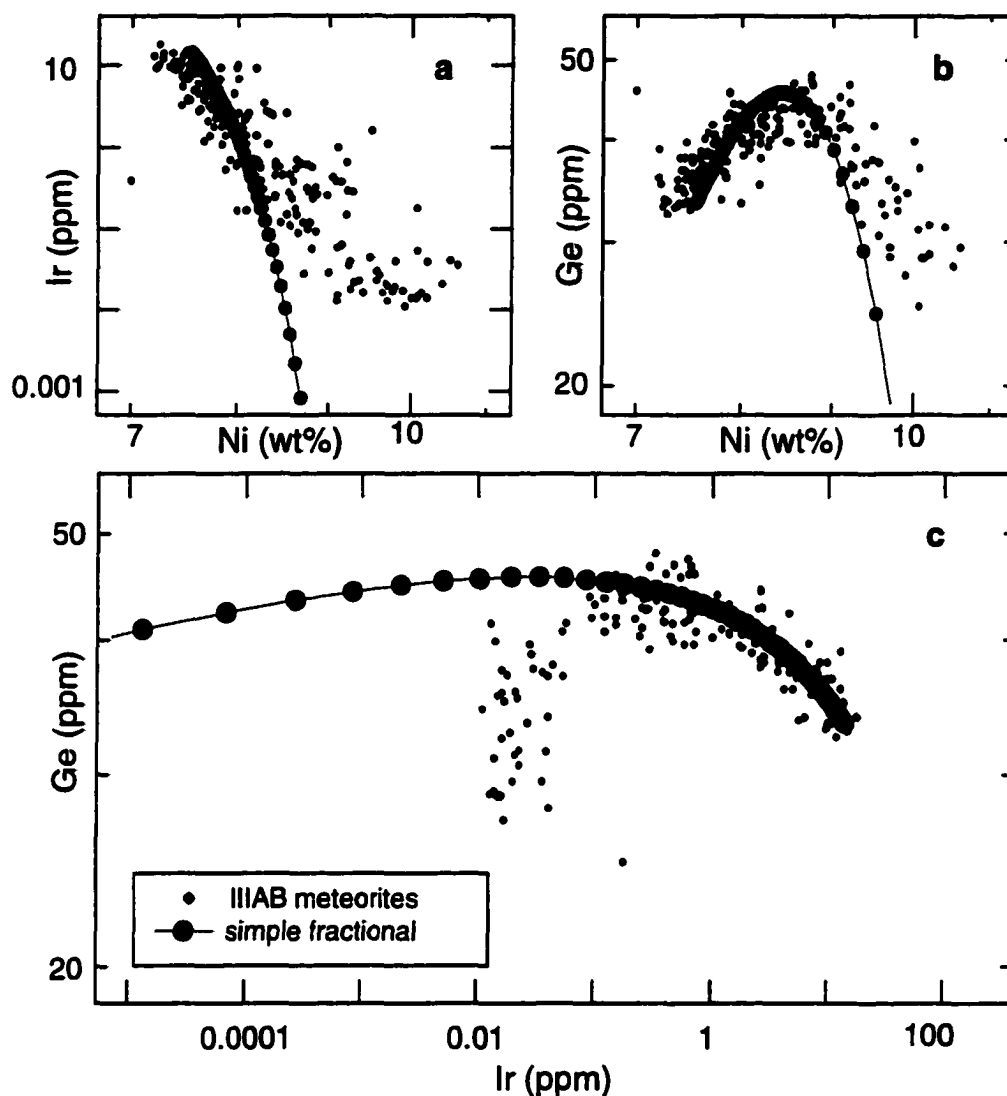
FIG. 5.1. The IIIAB iron meteorite group shows correlations on element versus element plots due to crystallization of a metallic core of the asteroid-sized parent body. Such element correlations are traditionally plotted versus Ni, as is done for (a) Ir and (b) Ge. Simple fractional crystallization calculations can reproduce the large range of Ir concentrations observed in the IIIAB iron meteorites as well as the distinctive curved trend of Ge. (c) However, when Ge is plotted versus Ir, simple fractional crystallization can not explain a significant portion of the crystallization trend, specifically the low Ir meteorites formed during the late stages of crystallization.

significantly from the general trend (e.g. the meteorite Ventura; Haack and Scott, 1993), the shape of the Ge versus Ir IIIAB trend is distinctly different from that predicted by simple fractional crystallization calculations. In Fig. 5.1c, it is evident that simple fractional crystallization cannot explain the late stage crystallization of IIIAB iron meteorites.

Previous studies have also suggested a more complex crystallization history than simple fractional crystallization for the metallic core of the IIIAB parent body. Pernicka and Wasson (1987) noticed the behavior of Re and Os in the IIIAB meteorite group is similar to the Ir behavior shown in Fig. 5.1. They attributed the leveling of the trends to small amounts of primitive metallic liquid draining through the mantle and being added to the molten core, a process which was modeled by Malvin (1988). Dendritic crystallization, instead of planar crystallization, has been argued to be the physical method by which the metallic core of an asteroid-sized body should solidify (Haack and Scott, 1992). Such a method of crystallization has been modeled to influence the IIIAB elemental trends (Narayan and Goldstein, 1982; Haack and Scott, 1993). Liquid immiscibility in the molten core has been suggested (Vogel, 1961) and quantitatively modeled (Ulff-Møller, 1998) to alter the resulting crystallization trends. Further evidence for a complex crystallization history of the IIIAB core comes from the Cape York meteorites which define elemental trends which are different from the main IIIAB trend (Esbensen et al., 1982). The apparent success of crystallization calculations using partitioning values from dynamic experiments (Sellamuthu and Goldstein, 1985), though Malvin et al. (1986) showed such partition coefficients to be unreliable, is still

TABLE 5.1. Starting model compositions.

Group	Au (ppm)	Ga (ppm)	Ge (ppm)	Ir (ppm)	Ni (wt%)	P (wt%)	Pd (ppm)	S (wt%)
IIIAB	1[a]	11.5[a]	22[a]	2[a]	7.6[a]	0.5[a]	4[a]	12[a]
IIAB			58[a]	1.3[b]		1[b]		17[b]
IVA			0.115[c]	2[c]		0.25[c]		2.5[c]
IVB			0.053[b]	22[b]		0.57[b]		0.0[b]
Den.								
IIIAB			36.25[d]	3.5[d]		0.56[d]		6[d]

References: (a) this work. (b) Jones and Drake (1983). (c) Scott et al. (1996). (d) Haack and Scott (1993).

TABLE 5.2. Parameters for the calculation of solid metal/liquid metal molar partition coefficients.

	Au[a]	Ga[a]	Ge[a]	Ir[a]	Ni[b]	P[b]	Pd[c]
C_{SP}	-1.099	-0.321	-0.543	0.505	-0.101	-2.443	-0.723
β_S	-0.939	-1.459	-1.752	-2.594	-0.339	-1.433	-0.506
β_P	-0.645	-0.956	-0.927	-0.937			

Parameterization method from Jones and Malvin (1990): $\ln k_E = C_{SP} + \{\beta_S[2X_S/(2X_S+4X_P)] + \beta_P[4X_P/(2X_S+4X_P)]\}\ln(1-2.18X_S -5.4X_P)$ where k_E is the molar solid metal/liquid metal partition coefficient of element E, and X_S and X_P are the mole fractions of S and P in the metallic liquid. All models use mass units, so it was necessary to convert k_E to a weight partition coefficient, D_E, before any calculations were completed.

References: (a) Haack and Scott (1993). (b) Jones and Malvin (1990). (c) Chabot and Drake (1997).

suggestive of a more complex crystallization history than just simple fractional crystallization to reproduce the IIIAB trends.

In this chapter, I introduce a simple model developed to examine the role of mixing in the molten portion of a crystallizing core (Chabot and Drake, 1999a). The possibility that the molten core could develop inhomogeneities which could affect the crystallizing metal has been previously suggested (Haack and Scott, 1993; Chabot and Drake, 1996; Scott et al., 1996) though not fully modeled. This mixing model is applied to four distinctly different crystallization scenarios, and the results are then compared to the results from other IIIAB crystallization models.

5.2 The Mixing Model

One of the fundamental assumptions of simple fractional crystallization is that the metallic liquid is well mixed and homogeneous. In simple fractional crystallization calculations, when solid metal begins to crystallize, the entire liquid composition consequently changes. The model presented here does not make this assumption. Rather, the liquid is considered to be composed of two reservoirs, *Zone 1* and *Zone 2*. *Zone 1* is the metallic liquid which is actively involved in the crystallization process, and whose composition consequently changes because of the crystallization of solid metal. *Zone 2* is the remaining metallic liquid which is too far from the actively crystallizing solid to be involved or affected by the process. These two zones are shown schematically in Fig. 5.2.
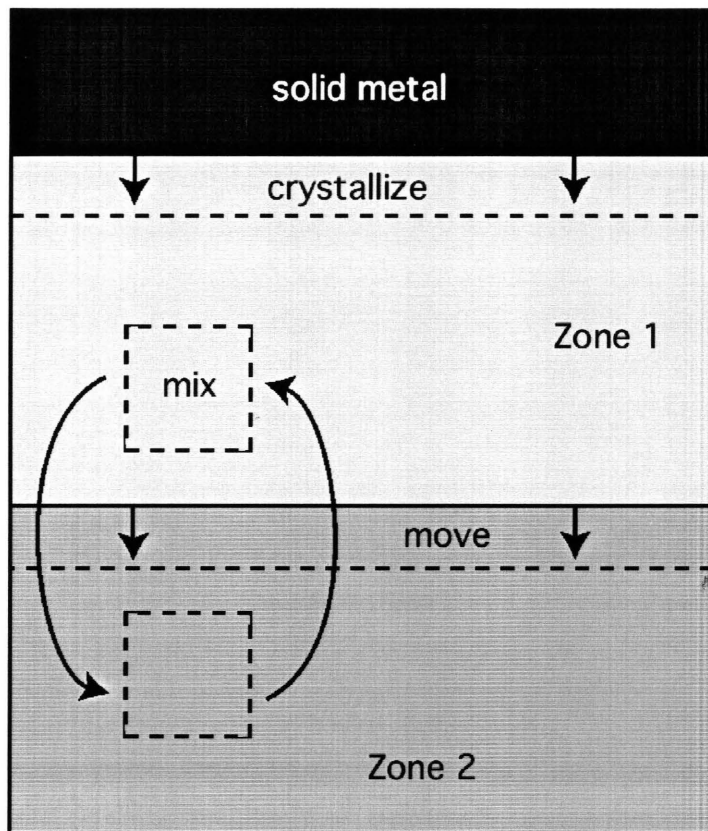
FIG. 5.2. A schematic illustration of the parameters of the mixing model are shown. *Zone 1* is the actively crystallizing region of the molten core, while *Zone 2* refers to the metallic liquid of the core which is too far removed from the crystallizing solid metal to be involved in the crystallization process. The two zones of liquid interact with each other through the parameters *move* and *mix*, both of which are rates relative to the rate of crystallization. *Mix* is a pure swapping of liquids between the two zones. *Move* controls the sizes of the zones and causes some liquid which was previously in one zone to be incorporated into the other zone.

Though only *Zone 1* is directly affected by crystallization, *Zone 1* and *Zone 2* are allowed to interact with each other. This interaction is accounted for with the model parameters of *move* and *mix*, also illustrated in Fig. 5.2. The parameters *move* and *mix* are rates of processes relative to the rate of crystallization.

The parameter *move* controls the relative sizes of *Zone 1* and *Zone 2* compared to their initial sizes. As solid metal crystallizes, the amount of liquid in *Zone 1*, the crystallizing liquid, decreases. This may force *Zone 1* to expand away from the crystallizing solid, into some liquid that was previously in *Zone 2*. The liquid it expands into is incorporated into *Zone 1*, changing the bulk composition of *Zone 1* slightly. The composition of *Zone 2* is unchanged by this process. The amount that *Zone 1* expands relative to the amount of solid that crystallizes is the parameter *move*. However, *move* can also be negative if *Zone 1* is not expanding away from the crystallizing metal but rather shrinking towards it. If *move* is negative, some liquid which was previously in *Zone 1* is left behind in *Zone 2*. In this case, the composition of *Zone 2* is altered slightly but the composition of *Zone 1* is unchanged by the process. Physically, *move* recognizes that there is probably a characteristic length scale over which the liquid senses the crystallization of the solid. That length is less than the radius of the molten core.

The parameter *mix* does not affect the sizes of the zones; *mix* is a pure swapping of liquid between *Zone 1* and *Zone 2*. This changes the composition of the liquid in both zones. If *mix* is set to a large value, the rate of mixing is much faster than the rate of crystallization. In this case, the resulting elemental trends are identical to those shown

in Fig. 5.1 for simple fractional crystallization calculations. Physically, *mix* might correspond to partial convective overturn.

The actual calculations for this mixing model are carried out in the same manner as for simple fractional crystallization calculations. The crystallization process is broken down into about 10,000 steps. For each step, some fraction f of the liquid in *Zone 1* crystallizes. The composition of the resulting solid and the remaining liquid in *Zone 1* are given simply using mass balance equations and the definition of the partition coefficient:

$$LZ1(E) = \frac{LZ1_i(E)}{(1 - f + fD_E)}$$ **Eq. 5.1**

$$S(E) = \frac{(D_E)LZ1_i(E)}{(1 - f + fD_E)}$$ **Eq. 5.2**

$LZ1_i(E)$ is the initial composition of element E in *Zone 1* before that crystallization step. $LZ1(E)$ is the resulting composition of element E in *Zone 1* after crystallization. $S(E)$ is the composition of the solid which crystallizes, D_E is the experimentally determined solid metal/liquid metal partition coefficient for an element E, and f is the mass fraction which solidifies from *Zone 1* at each step. The partition coefficients are given in Table 5.2 in molar form, though all calculations are carried out in mass units so it is necessary to convert the partitioning values in Table 5.2 to weight partition coefficients. D_E is a function of the S and P concentrations of the metallic liquid in *Zone 1* and is recalculated before each crystallization step. A value of 0.01 for D_S was used in

all calculations, and this value is in agreement with the partitioning behavior of S observed experimentally (Willis and Goldstein, 1982; Chabot and Drake, 1997). The variable f is chosen to crystallize equal fractions of the entire core mass for each calculation step. The variable f is consequently a function of the size of *Zone 1* and calculated as 1/10,000/*Zone 1*.

After a crystallization step, the parameters *move* and *mix* are applied, altering the sizes and compositions of *Zone 1* and *Zone 2*. The calculation then repeats, and *Zone 1* begins another crystallization step. This continues until the Fe-FeS eutectic composition is reached.

5.3 Mixing Scenarios and Model Results

Using the mixing model described, the metallic core of an asteroid-sized body can be envisioned to crystallize in a number of ways. Four crystallization scenarios, which span a range of possible physical conditions and were selected for purposes of illustration only, will be considered in detail. These scenarios are used to illustrate the effects of mixing; obviously, other crystallization conditions could also be considered. These four scenarios are illustrated in Fig. 5.3. The four crystallization scenarios are quite distinct from each other, yet all four scenarios reproduce the IIIAB elemental trends more accurately than simple fractional crystallization calculations because they include the effects of mixing. Two reservoirs of liquid in the molten core allow elemental concentrations to be buffered.

The starting liquid composition is given in Table 5.1 and was chosen by trial and error to best fit the trends being modeled. For the IIIAB group, a starting S-content of 12 wt% was chosen, which is similar to the value of 10.8 wt% preferred by Ulff-Møller (1998). The IIIAB starting composition given in Table 5.1 is also in good agreement with that used by Haack and Scott (1993) in their simple fractional crystallization model which began with 12 wt% S. It is also worth noting that a metallic core with a bulk S-content of 12 wt% S does not require an explanation such as "explosive volcanism" (Keil and Wilson, 1993) since such a core is not depleted in S relative to ordinary chondrites.

5.3.1 Mixing Scenario 1: A Boundary Layer

The first mixing scenario involves a small boundary layer of liquid that is not involved in the crystallization process. This boundary layer is thus *Zone 2* in the mixing model and is only 1% of the initial metallic liquid. Solid metal crystallizes from the majority of the liquid, *Zone 1*, and this changes the composition of *Zone 1* as crystallization proceeds. The composition of *Zone 1* is also changed because with each crystallization step, a small portion of the boundary layer is consumed into *Zone 1*. The consumption of the boundary layer happens at a rate that is only 1% of the rate of crystallization, and thus the parameter *move* is set to 0.01. The parameter *mix* is set to zero in this scenario, and consequently the composition of the boundary layer, *Zone 2*, does not change and is simply the original starting liquid composition.

The evolution of the metallic core in this scenario is shown schematically in Fig.
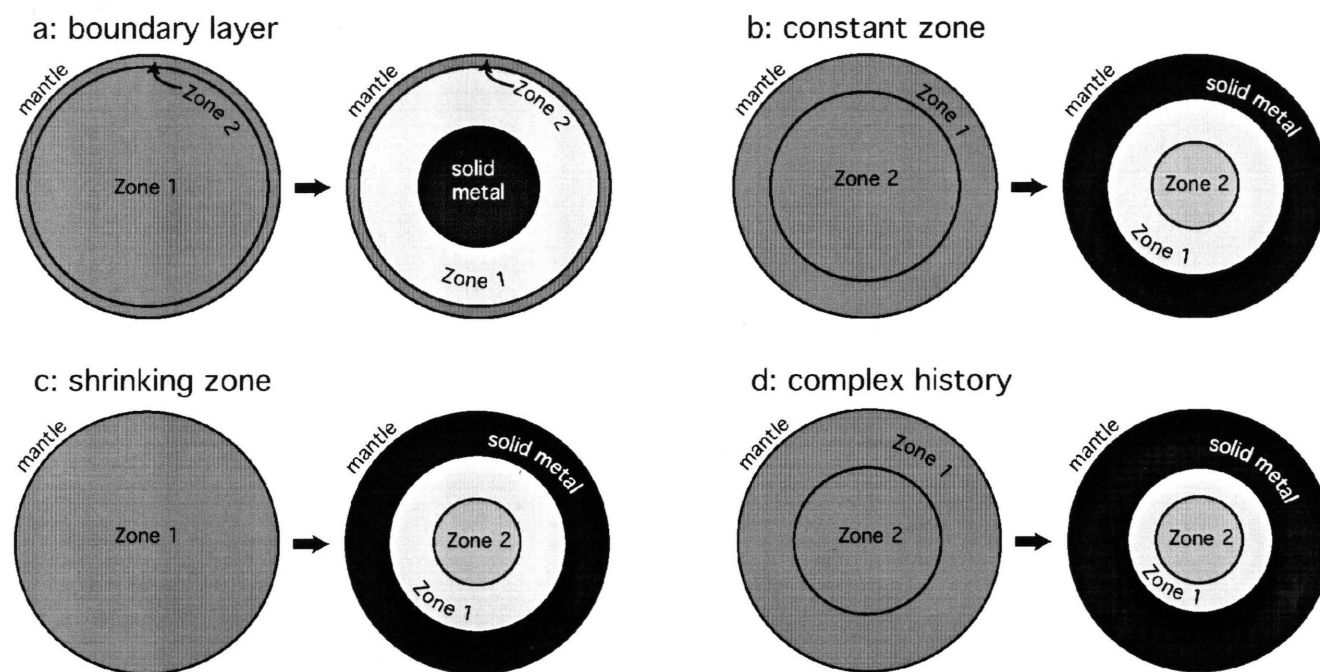
FIG. 5.3. The four mixing scenarios which were modeled are illustrated in the initial, fully molten state of the core and at some later time during crystallization. In each illustration, the level of gray refers to the amount of S in the metallic liquid; as a liquid crystallizes, it becomes enriched in S and is depicted as a lighter shade of gray. **(a)** The boundary layer scenario is depicted, where 1% of the liquid of the core remains at the core/mantle boundary and is not mixed with the majority of the molten core. This boundary layer retains its original composition throughout the crystallization process. **(b)** This mixing scenario envisions a constant zone of crystallization, where *Zone 1* remains the same size throughout the crystallization process. In this scenario, the compositions of both zones change. **(c)** This illustrates the shrinking zone of crystallization scenario. Initially the entire core is actively involved in crystallization, but as crystallization proceeds, all of the liquid cannot remain involved in crystallization. This causes *Zone 2* to be created and expand during the crystallization process. **(d)** The fourth mixing scenario is the most complex and involves non-constant mixing parameters, shown in Fig. 5.5. Specifically, in the beginning, mixing is very efficient, but as crystallization proceeds, the entire molten core becomes less well mixed.

TABLE 5.3. Mixing model parameters.

Mixing Scenario	$Zone\,1_o$	$Zone\,2_o$	mix	move
1: boundary layer	0.99	0.01	0	0.01
2: constant crystallization zone	0.20	0.80	10	1
3: shrinking crystallization zone	1.00	0.00	0.75	-0.25
4: complex history	0.40	0.60	Fig. 5a	Fig. 5b

$Zone1_o$ and $Zone2_o$ refer to the starting fraction of the molten core in each reservoir.

5.3a, and the starting parameters for the mixing model are given in Table 5.3. Figure 5.4a plots the evolution of the three reservoirs, *Zone 1*, *Zone 2*, and the solid metal, over the course of crystallization of the metallic core. As Fig. 5.4a shows, the total solid metal steadily increases over the crystallization process while *Zone 1* steadily decreases at nearly the same rate. *Zone 2* also decreases slightly as it gets incorporated into *Zone 1*. Figure 5.3a illustrates this scenario as involving outward crystallization of a solid metal core. The boundary layer, *Zone 2*, will have a lower S-content than the crystallizing liquid, *Zone 1*, so it is gravitationally unstable to have *Zone 2* above *Zone 1*. Nevertheless, because *Zone 2* is a small portion of the liquid and envisioned as a boundary layer between the core and mantle of an asteroid-sized body, perhaps an irregular shape of the core/mantle boundary can keep this small amount of liquid from mixing with the majority of the molten core.

5.3.2 Mixing Scenario 2: A Constant Zone of Crystallization

The second mixing scenario envisions a zone of liquid involved in the crystallization process, *Zone 1*, that is a constant size. *Zone 1* initially is 20% of the total mass of the liquid core and in order for *Zone 1* to remain this size, the rate of expansion of *Zone 1* must equal the rate it is being used up by crystallization. The parameter *move* must thus be set to 1.0. The parameter *mix* influences the compositions of both *Zone 1* and *Zone 2*, and a value of 10.0 was chosen to reproduce the IIIAB trends. The compositions of both zones consequently change throughout the crystallization of the solid metal core. Figure 5.3b illustrates the evolution of an initially homogeneous,
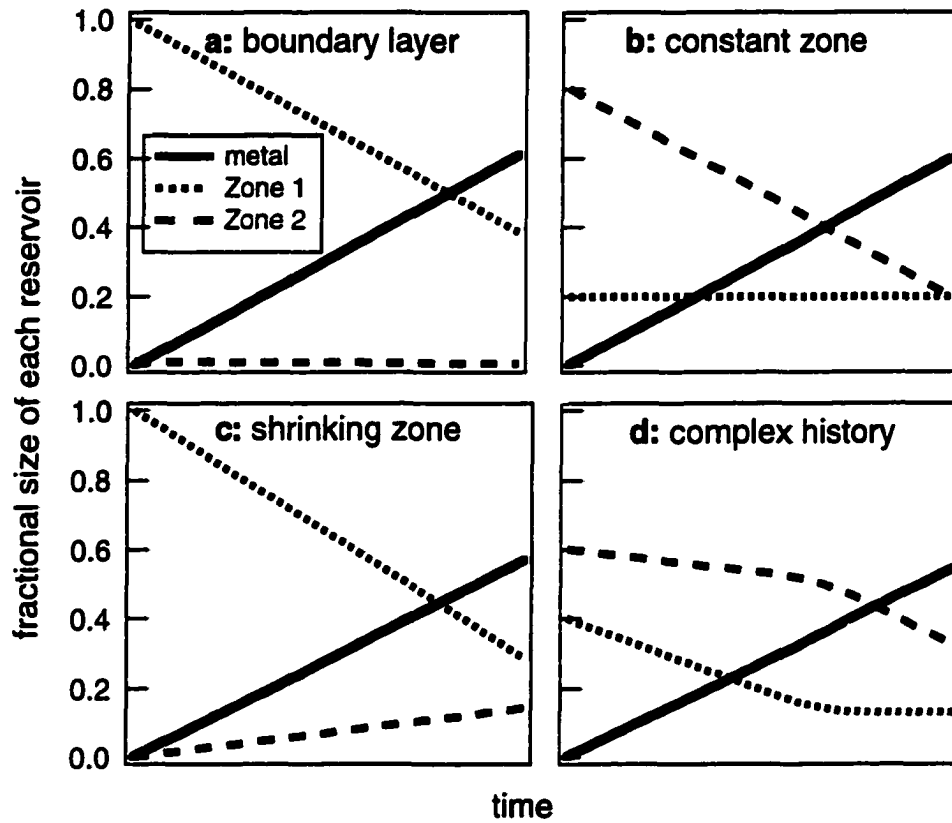
FIG. 5.4. The evolution of *Zone 1*, *Zone 2*, and the crystallizing solid metal is shown for each of the four mixing scenarios, (a) mixing scenario 1, the boundary layer case; (b) mixing scenario 2, the constant zone of crystallization; (c) mixing scenario 3, the shrinking zone of crystallization; (d) mixing scenario 4, the case with non-constant mixing parameters.

molten core by this mixing scenario. Table 5.3 gives the parameters used in the mixing model, while Fig. 5.4b shows the evolution of the three reservoirs over the crystallization process. As expected, Fig. 5.4b shows that the amount of solid metal increases with time; *Zone 2* decreases at the same rate the solid metal is increasing, and *Zone 1* keeps a fixed size. This scenario is shown in Fig. 5.3b as inward crystallization from the base of a solid mantle to keep the denser liquid of *Zone 2* below the S-rich, less dense liquid of *Zone 1*.

5.3.3 Mixing Scenario 3: A Shrinking Zone of Crystallization

The third scenario envisions a shrinking zone of liquid involved in the crystallization process. The scenario is initially identical to simple fractional crystallization; all of the liquid is involved in the crystallization process, so all of the liquid is in *Zone 1*. Initially, there is no *Zone 2*. As crystallization proceeds, not all of the liquid can remain actively involved in crystallization, and consequently, *Zone 2* is created. To model this shrinking of *Zone 1*, a negative value of the parameter *move* is necessary and a shrinking rate 25% of the rate of crystallization was used. The parameter *move* thus has a value of -0.25. This scenario also involves mixing between the two zones at a rate of 75% of that of crystallization, or a value for *mix* of 0.75. Table 5.3 lists all the starting mixing model parameters, and Fig. 5.3c illustrates the evolution of a crystallizing core with this mixing scenario. Figure 5.4c indicates that as the amount of total solid increases, the amount of liquid involved in the crystallization process, *Zone 1*, decreases while the amount of liquid not involved in crystallization,

Zone 2, increases. As in mixing scenario 2, an inward method of core crystallization is favored in order to keep the system gravitationally stable.

5.3.4 Mixing Scenario 4: A More Complex Crystallization History

The three previous mixing scenarios involved constant values for the parameters *move* and *mix*. There is, however, no physical reason why these parameters should be constant. As crystallization proceeds, the crystallizing liquid becomes increasingly S-rich, which could make mixing between the denser, underlying liquid not involved in crystallization and the lighter, crystallizing liquid increasingly difficult as more solid metal forms. The way the two zones of liquid interact would change, and, consequently, non-constant values for the parameters *move* and *mix* are necessary to model such a scenario.

Figure 5.3d illustrates the fourth mixing scenario, and Table 5.3 lists the model parameters for this case. At the onset of crystallization, the parameter *mix* is set to a high value, 30 times faster than the rate of crystallization. With such a fast rate of mixing between the two zones, the beginning stage of this scenario resembles simple fractional crystallization. As crystallization proceeds, mixing becomes increasingly difficult, and the mixing rate begins to decrease. Mixing continues to decrease until a minimum value of 3 times the rate of crystallization is reached. Figure 5.5a shows graphically how the parameter *mix* changes as the core crystallizes, beginning at 30 and dropping to 3. The parameter *move* is shown in Fig. 5.5b as a function of time. As crystallization proceeds, the size of *Zone 1* decreases. *Zone 1* does not shrink as in
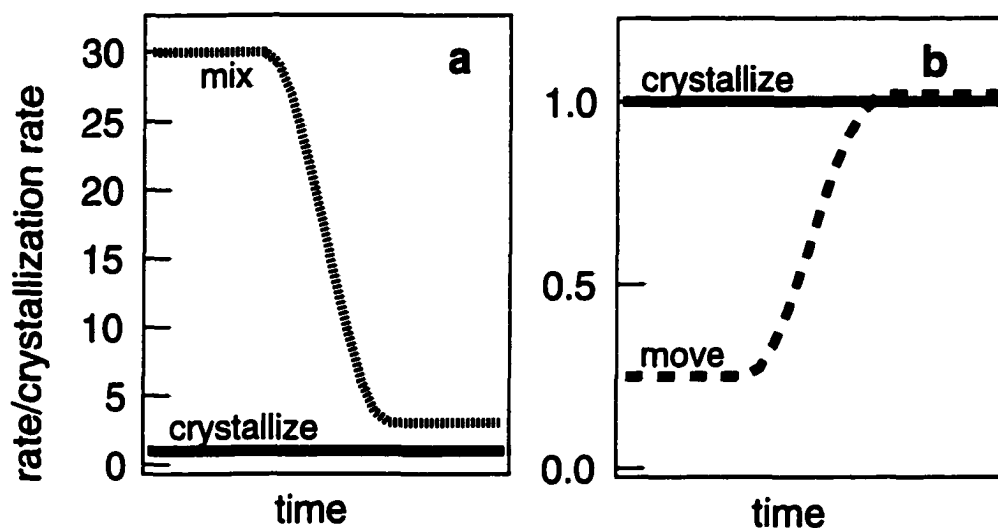
FIG. 5.5. The mixing model parameters of (a) *mix* and (b) *move* are illustrated for mixing scenario 4, the mixing scenario involving non-constant mixing parameters. The parameter *mix* has an initial value of 30, which means mixing is 30 times faster than crystallization. This creates a well-mixed molten core with crystallization trends that resemble simple fractional crystallization. As crystallization proceeds, mixing becomes less efficient, and the parameter *mix* drops to a value of 3. The parameter *move* controls the size of *Zone 1*. *Zone 1* decreases until it reaches a minimum size.

mixing scenario 3; the value of *move* is still positive, but it is less than the crystallization rate. Consequently, with each crystallization step, *Zone 1* expands into *Zone 2* more slowly than it gets used up by crystallization. This decreasing of *Zone 1* is only allowed to continue until *Zone 1* reaches a minimum size of slightly larger than 10% of the initial size of the completely molten core. At this point, *move* is set to a value of 1.0 so *Zone 1* will stay a constant size.

The evolution of the three reservoirs for this mixing scenario is shown in Fig. 5.4d. The sizes of *Zone 1* and *Zone 2* are no longer linear functions of time due to the non-constant parameters in the mixing model. *Zone 1* decreases and then levels off to a constant size, at which point the size of *Zone 2* begins to decrease more quickly. As always, the amount of solid metal increases throughout the process. Again, as in mixing scenarios 2 and 3, an inward method of core crystallization is favored in order to keep the system gravitationally stable.

5.3.5 Model Results

For each of the four mixing scenarios and simple fractional crystallization, the resulting iron meteorite elemental trends for the IIIAB group are plotted in Fig. 5.6 versus Ni. The elements Au, Ga, Ge, Ir, P, Pd, and Ni were all modeled. References for the IIIAB meteorite data are given in Haack and Scott (1993) and Chabot and Drake (1997). For some elements such as Au, P, and Pd, all five calculations produce the same trend, and all match the observed IIIAB iron meteorite trend well. Thus, elements
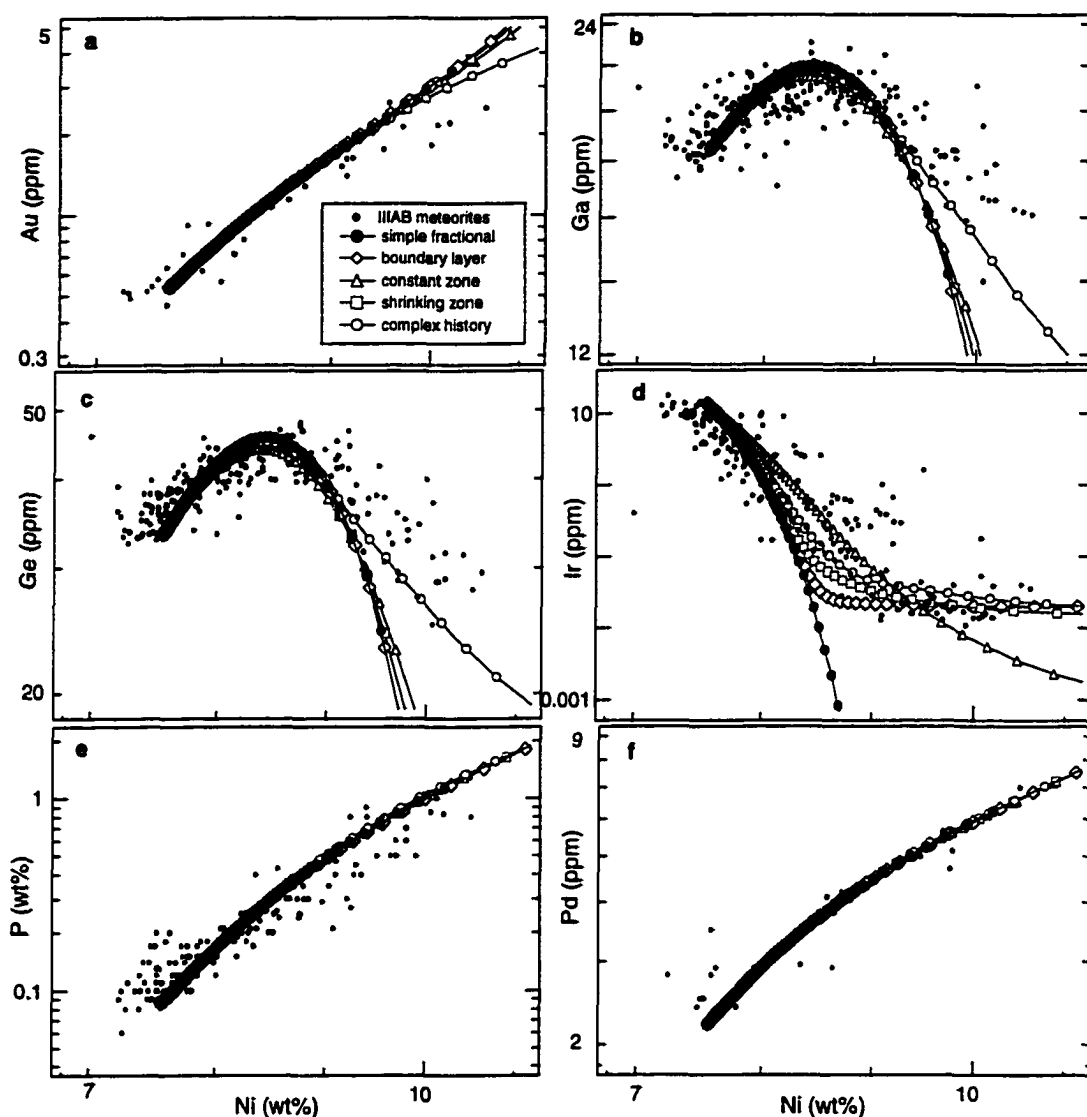
FIG. 5.6. The crystallization trends for simple fractional crystallization and the four mixing scenarios are shown for the elements (a) Au, (b) Ga, (c) Ge, (d) Ir, (e) P, and (f) Pd plotted versus Ni. Elements that were fit well by simple fractional crystallization, such as Au, P, and Pd, are fit equally well by the mixing scenarios. The Ir versus Ni trend for all four mixing scenarios is significantly different than the simple fractional crystallization model and shows a leveling off of Ir concentrations. The modeled trends for Ga and Ge are all similar to simple fractional crystallization except for mixing scenario 4, which appears to have a slightly improved fit to the observed IIIAB meteorites.

whose trends were explained well by simple fractional crystallization are explained equally well by any of the four mixing scenarios.

The elemental trend of Ir, on the other hand, is reproduced quite differently by the four mixing scenarios than by simple fractional crystallization calculations. Simple fractional crystallization and the mixing model calculations all reproduce the three orders of magnitude range in concentration values observed in the IIIAB meteorites. However, the predicted trend from simple fractional crystallization continues to drop to even lower Ir concentration levels while all four mixing scenarios show a significant leveling off of Ir concentrations.

The elements Ga and Ge have distinctive curved trends for the IIIAB group, and simple fractional crystallization as well as the four mixing scenarios also produce curved trends. However, the more complex mixing scenario which uses non-constant mixing parameters, scenario 4, predicts a slightly different shape for the late stage crystallizing portion of the Ga and Ge trends. The trend from mixing scenario 4 does not drop off in Ga or Ge concentrations as quickly as the other calculated trends. This is similar to the effect mixing had on the predicted Ir trend, causing concentrations to be buffered between *Zone 1* and *Zone 2* and not to drop off as quickly as would happen in simple fractional crystallization. The Ga and Ge trends from mixing scenario 4 do not level off as the Ir trend does, but it appears on Fig. 5.6 that if the trends for these two elements did level off, the observed IIIAB iron meteorites would be matched more accurately.

Figure 5.7 plots the same model calculations as shown in Fig. 5.6, but now Ge is

plotted versus Ir. As previously noted, on this type of graph, the inability of simple

fractional crystallization to fully explain the late stage crystallizing members of the

IIIAB group is clearly shown. However, all four mixing scenarios can reproduce the

observed trend in the IIIAB iron meteorites. The four mixing scenarios refer to

distinctly different modes of core crystallization, yet they all take into account the

effects of mixing. By including mixing in the model calculations, the concentrations of

elements can be effectively buffered between the two reservoirs of liquid, *Zone 1* and

Zone 2, and the Ge versus Ir trend shown in Fig. 5.7 can be reproduced.

The evolution of the Ni, S, and P compositions of *Zone 1* and *Zone 2* is shown for

each of the four mixing scenarios in Fig. 5.8. In the mixing calculations, it is assumed

that *Zone 1* is actively crystallizing and *Zone 2* is a reservoir of metallic liquid. *Zone 1*,

since it is the actively crystallizing region, is by definition at the liquidus temperature.

To remain a liquid, *Zone 2* must be at a temperature above the liquidus temperature,

which will depend on the composition of *Zone 2*. If the compositions of *Zone 1* and

Zone 2 vary significantly, the temperature of each zone must also vary significantly to

prevent *Zone 2* from crystallizing. In all four mixing scenarios, the Ni and P contents of

the two zones do not differ significantly. However, the S-contents of *Zone 1* and *Zone 2*

evolve differently with each mixing scenario. Scenario 1, the boundary layer scenario,

shows a considerable difference between the S-content of the two zones, making the

scenario physically implausible due to the temperature difference that would be

required to maintain *Zone 2* as a liquid. The other three scenarios, however, do not show
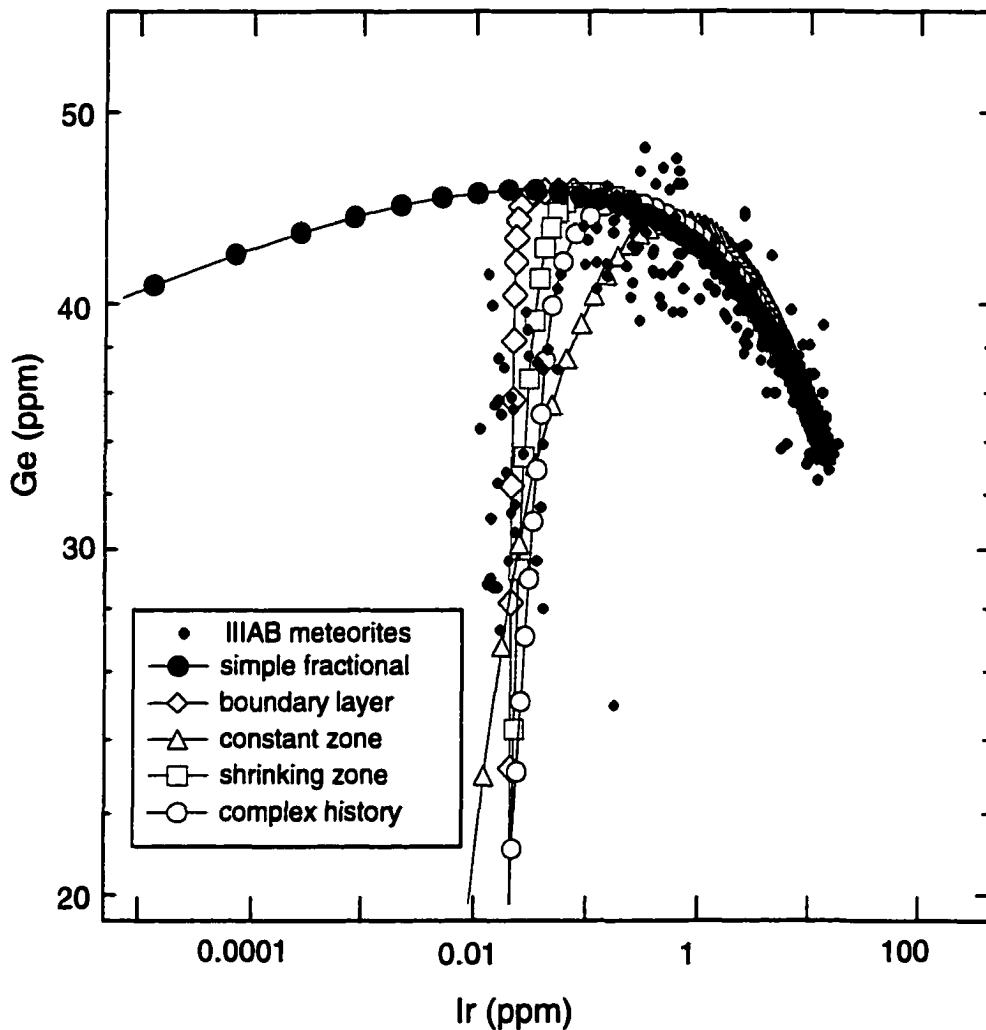
FIG. 5.7. On the Ge versus Ir plot shown, simple fractional crystallization can not explain the low Ir, late stage crystallizing portion of the IIIAB trend. All four of the mixing scenarios, even though the scenarios are quite distinct, can reproduce the entire IIIAB Ge versus Ir trend. Because all four mixing scenarios match the observed meteorite trend, a unique method of core crystallization is not suggested. The success of all four mixing scenarios shows that the presence of two reservoirs of liquid in the molten core allows element concentrations to be buffered and consequently reproduces the observed IIIAB trend.
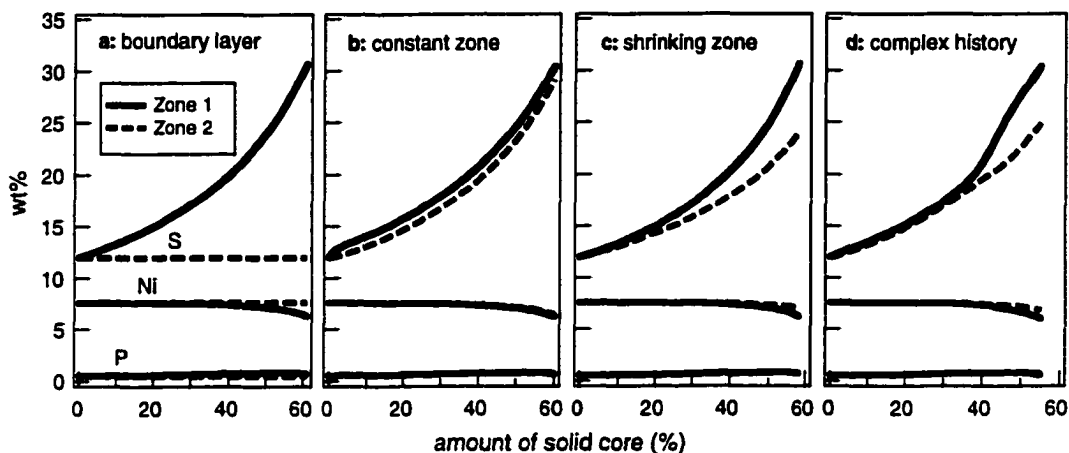
FIG. 5.8. The evolution of the Ni, S, and P compositions of *Zone 1* and *Zone 2* is shown for each of the four mixing scenarios, (a) mixing scenario 1, the boundary layer case; (b) mixing scenario 2, the constant zone of crystallization; (c) mixing scenario 3, the shrinking zone of crystallization; (d) mixing scenario 4, the case with non-constant mixing parameters. In all four mixing scenarios, the Ni-content and the P-content of the two zones do not differ significantly. However, since S is excluded from the crystallizing solid and will, consequently, become quickly enriched in the actively crystallizing region, *Zone 1*, the S-content of the two zones varies with each mixing scenario. The boundary layer scenario (a) shows a considerable difference between the S-content of the two zones and consequently is not physically plausible due to the temperature difference that would be required to maintain *Zone 2* as a liquid. The other 3 scenarios, however, do not show a considerable difference between the S-contents of the two zones during most of the crystallization period.

a considerable difference between the S-contents of the two zones during most of the crystallization period. The four scenarios which were considered are meant to illustrate the possible effects of mixing on the resulting chemical trends rather than suggest a specific method by which an asteroidal core crystallizes. Two reservoirs of liquid in the molten core, with only small compositional differences, can allow elemental concentrations to be buffered and reproduce IIIAB iron meteorite trends which simple fractional crystallization calculations cannot.

5.4 Comparison to Other IIIAB Crystallization Models

5.4.1 Assimilation-Fractional Crystallization

Pernicka and Wasson (1987) noticed that Re and Os concentrations in late stage IIIAB iron meteorites appeared to level off, rather than continue to decrease to low levels, as is seen also for Ir in Fig. 5.6. To explain this observation, they suggested that small amounts of primitive metallic liquid were being drained through the mantle and added to the molten core during the core crystallization process. Malvin (1988) modeled this process, calling it assimilation-fractional crystallization. Malvin found that the addition of an original composition liquid at a rate which was 1% of that of crystallization produced a leveling off trend for Ir which appeared to better fit the IIIAB data on an Ir versus Ni plot.

Though conceptually quite different, the assimilation-fractional crystallization model of Malvin is almost mathematically identical to mixing scenario 1, which
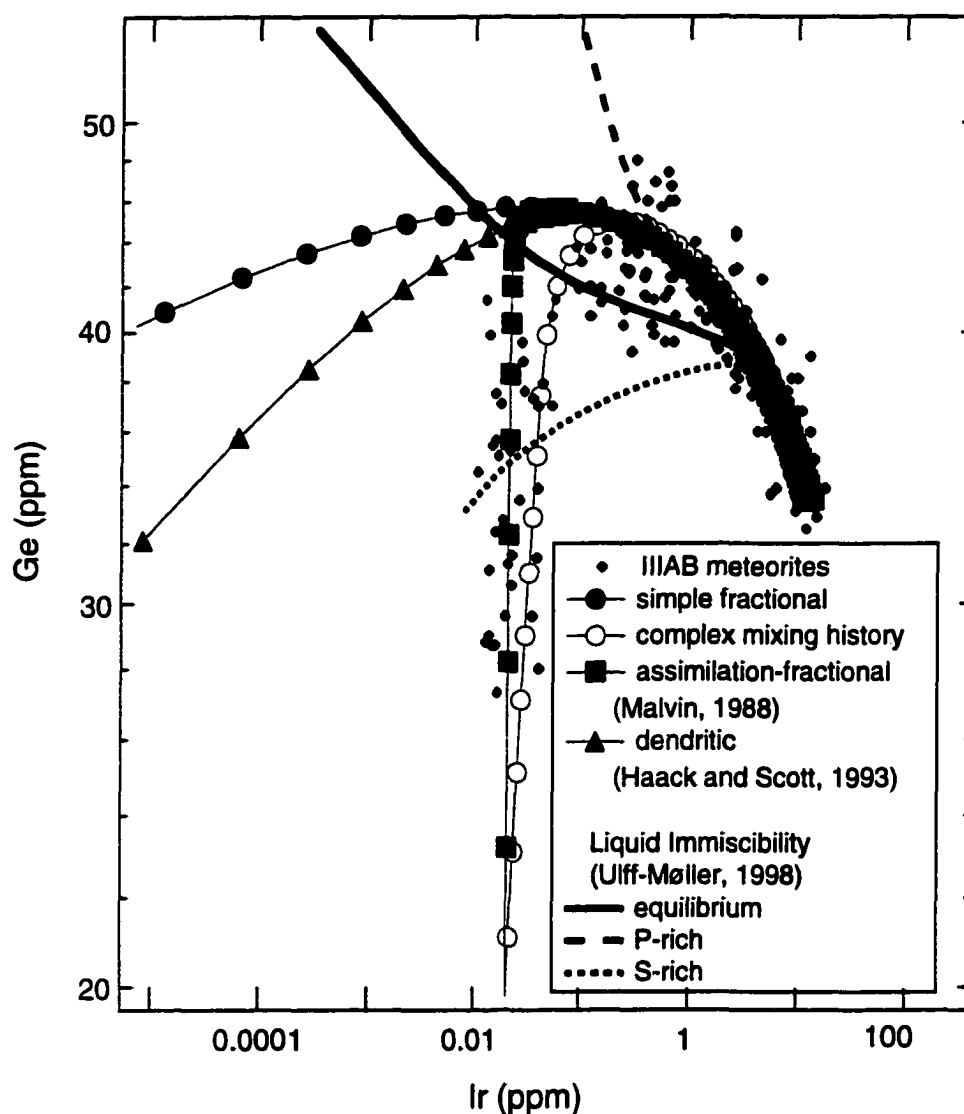
FIG. 5.9. Models of core crystallization for the IIIAB iron meteorite group are compared. An assimilation-fractional crystallization model by Malvin (1988) is mathematically similar to mixing scenario 1, the boundary layer scenario, and can reproduce the observed IIIAB Ge versus Ir trend. Though the core of an asteroid-sized body may crystallize in a dendritic manner, a dendritic crystallization model by Haack and Scott (1993) fails to reproduce the IIIAB trend. Three liquid immiscibility scenarios were examined by Ulff-Møller (1998) and produced crystallization trends quite different from one liquid models. However, none of the three liquid immiscibility scenarios can reproduce the observed IIIAB Ge versus Ir trend, suggesting the presence of another process even if liquid immiscibility did occur.

involves a boundary layer of original composition liquid. The only mathematical difference is that the mixing scenario describes a closed system while the Malvin model adds new material during the crystallization process. The resulting Ge versus Ir trend calculated from assimilation-fractional crystallization is shown on Fig. 5.9. Like mixing scenario 1, assimilation-fractional crystallization is able to reproduce the IIIAB trend.

Questions have been raised as to the physical plausibility of the model of Malvin. Haack and Scott (1993) commented that it would be difficult to add metal to the core during the final stages of crystallization because the base of the mantle would be almost entirely solid. Ulff-Møller (1998) also noted that it seemed unlikely that a liquid would survive unfractionated in the mantle of a cooling parent body. However, the model of Malvin does involve two sources of metallic liquid, one involved in crystallization, and one hidden in the mantle. With two reservoirs of liquid, Malvin is able to reproduce the IIIAB Ge versus Ir trend, suggesting that even if the physical setting has been questioned, the concept of having two reservoirs of metallic liquid can buffer element concentrations.

5.4.2 Dendritic Crystallization

Haack and Scott (1992), using physical arguments, concluded that metallic cores in asteroid-sized bodies crystallize by inward dendritic crystallization and, consequently, might produce different elemental trends than predicted by simple fractional crystallization. Dendritic crystallization, as compared to planar crystallization, can arise if the metallic liquid near the crystallization front does not remain well mixed, causing

the solid to grow in tree-like protuberances. In an attempt to model dendritic crystallization of a metallic core, Haack and Scott (1993) developed a simple model which was mathematically similar to fractional crystallization calculations but the amount of S in the metallic liquid was not allowed to increase as quickly. It was argued that during a dendritic crystallization process, the S would accumulate in S-rich pockets or boundary layers and thus be effectively removed from the crystallizing system.

As an approximation of this situation, Haack and Scott (1993) performed simple fractional crystallization calculations using a D_S of $0.5 + 0.025*wt\%S_{Liq}$ instead of the experimental determined value of ~0.01 (Willis and Goldstein, 1982; Chabot and Drake, 1997). Using this D_S, the amount of S in the metallic liquid was not allowed to increase as quickly as during simple fractional crystallization, perhaps mimicking what would occur during the process of dendritic crystallization. In Fig. 5.10a and Fig. 5.10b, two of the crystallization trends produced by the dendritic model of Haack and Scott (1993) are shown. The starting composition is given in Table 5.1. In their modeling, Haack and Scott used a value for D_{Ni} which is shown in Fig. 5.10c (personal communication) and differs noticeably from a parameterization of the experimental partitioning data (Jones and Malvin, 1990). Using a D_{Ni} which is consistent with experimentally determined partition coefficients, I recalculated the crystallization trends produced by the dendritic crystallization model of Haack and Scott (1993). As shown on Fig. 5.10a and Fig. 5.10b, when a D_{Ni} is used which is consistent with the experimentally determined partitioning data, the IIIAB trends versus Ni are reproduced

FIG. 5.10. The elemental trends of (a) P and (b) Ge plotted against Ni are shown for the IIIAB group, along with the results of simple fractional crystallization calculations. Two sets of trends which were both produced using the dendritic crystallization model of Haack and Scott (1993) but used different values for D_{Ni} are also plotted. (c) In their paper, Haack and Scott use a value for D_{Ni} which is inconsistent with the experimental partitioning data. Shown in this figure are the values for k(Ni) used by Haack and Scott, parameterized by Jones and Malvin (1990), and determined experimentally (compiled in Jones and Malvin, 1990). The quantity k(Ni), like D_{Ni}, is the solid metal/liquid metal partition coefficient of Ni, but expressed as a molar ratio rather than a weight ratio. The parameterization of k(Ni) by Jones and Malvin agrees well with the experimental data while the value used by Haack and Scott falls noticeably below the experimental determinations. As shown on (a) and (b), when a solid metal/liquid metal partition coefficient for Ni is used which is consistent with the experimentally determined partitioning data, the IIIAB trends versus Ni are reproduced much more poorly with the dendritic crystallization model than just by simple fractional crystallization.
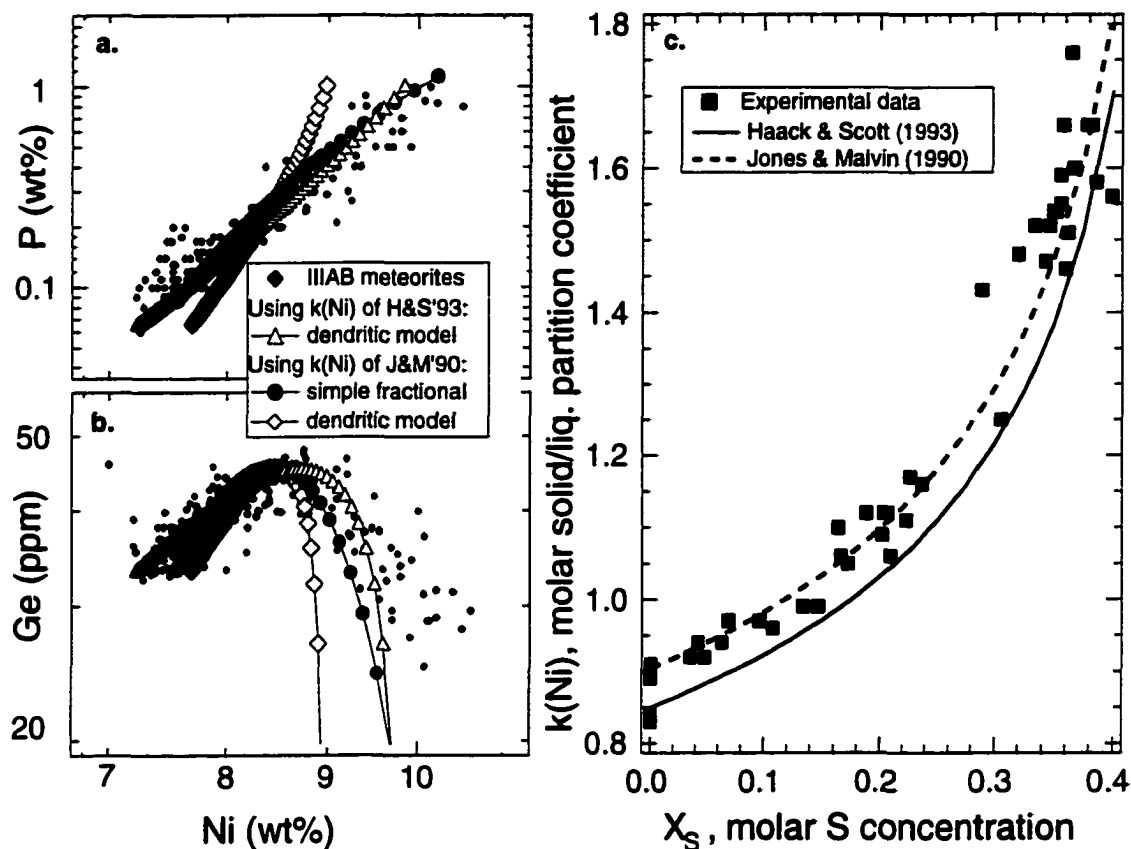
much more poorly with the dendritic crystallization model than just by simple fractional crystallization.

In their paper, Haack and Scott do not offer any comment about their choice of D_{Ni}, and Fig. 5.10a and Fig. 5.10b serve as illustrations of how sensitive the results of crystallization models can be to the partition coefficients used. However, Fig. 5.9 plots Ge versus Ir for the dendritic model, which is not affected by the choice of D_{Ni}. Figure 5.9 clearly shows that like simple fractional crystallization calculations, the dendritic crystallization model of Haack and Scott (1993) fails to match the observed late stage crystallizing portion of the IIAB trend. This result does not mean that the cores of asteroid-sized bodies did not crystallize in a dendritic process; it just means the method by which Haack and Scott attempted to model dendritic crystallization does not reproduce the observed elemental trends of the IIAB iron meteorite group. It should be noted that Fig. 5.3 shows all mixing scenarios as planar, concentric growth of the solid metal, but this is done only as a convenience to keep the illustrations simple. This mixing model does not favor dendritic over planar crystallization or vice versa since the model has no parameter to distinguish between the two methods. However, as noted by Haack and Scott (1993), if the molten core crystallized by growing very large dendrites, this could make complete homogenous mixing increasingly difficult, and consequently mixing effects as modeled in my work would become significant.

5.4.3 Liquid Immiscibility

When the modeled evolution of the IIIAB molten core is compared to the Fe-P-S phase diagram (Schürmann and Neubert, 1980; Raghavan, 1988), it is clear the metallic liquid encounters a large immiscibility field and should consequently produce two immiscible metallic liquids, one S-rich and one P-rich. The effect of liquid immiscibility has not been included in this mixing model. However, experiments have been conducted at conditions believed to be relevant to the IIIAB crystallizing core, and these experiments suggest the role of liquid immiscibility in crystallizing asteroidal cores is much smaller than the published Fe-P-S phase diagram predicts (Chabot and Drake, 1999b). Chapter 6 presents these experiments and discusses this issue in detail.

The effects of liquid immiscibility on the IIIAB elemental trends have been examined by Ulff-Møller (1998) and found to significantly change the predicted trends from simple fractional crystallization calculations. Ulff-Møller examined three crystallization scenarios. One of the scenarios involved fractional crystallization with the two immiscible liquids in complete equilibrium with each other. The two disequilibrium scenarios considered crystallizing from only the S-rich liquid or from only the P-rich liquid, which would be the two most extreme disequilibrium cases and bracket all other possibilities.

The resulting trends for these crystallization scenarios which involve liquid immiscibility are plotted on a Ge versus Ir diagram in Fig. 5.9 and do not reproduce the distinctive shape of the late stage crystallizing portion of the IIIAB trend. Thus, even if liquid immiscibility does affect the crystallizing metallic core of the IIIAB parent body,

some other process is still necessary to effectively buffer element concentrations and explain the late stage crystallizing members of the IIIAB group.

5.5 Discussion

5.5.1 Discrepancies between Model Results and Meteorite Collections

In all four mixing scenarios and simple fractional crystallization calculations only about 60% of the original mass of the molten core solidifies; the remaining 40% of the metallic liquid has the Fe-FeS eutectic composition, at which point the model stops. This remaining liquid is a significant mass of the core, yet there are no meteorites that appear to be samples of this reservoir. It has been argued that perhaps S-rich objects would be too weak to survive the journey through space or the passage through the atmosphere and would weather quickly on Earth if they did survive; consequently these S-rich meteorites are not represented in our meteorite collections (Kracher and Wasson, 1982). In their dendritic crystallization model, Haack and Scott (1994) reported only 6% remaining eutectic composition liquid. Such a low amount of uncrystallized liquid was achieved by constantly removing S from the system. Thus, in the model of Haack and Scott, there is only 6% eutectic composition liquid, but there is also a considerable amount of S-rich boundary layer material remaining at the end of crystallization.

If it is assumed that each IIIAB meteorite is from a random location of the IIIAB parent body core, the IIIAB parent body core has been sampled randomly nearly 200 times. Contrary to the lack of S-rich meteorites, there is an overabundance of late stage crystallizing IIIAB iron meteorites compared to model predictions. All model

calculations have been conducted in equal mass steps. Each point on a modeled trend, shown in Fig. 5.1, Fig. 5.6, Fig. 5.7, Fig. 5.9, and Fig. 5.10, corresponds to an amount of 1% of the original liquid. The markers at the late stage portion of the crystallization trends are more widely spaced while initially the markers are so close together they are indistinguishable. The IIIAB meteorites, on the other hand, while not uniformly distributed on the elemental trends, do not show the distribution predicted by the model calculations.

This discrepancy is depicted quantitatively in Fig. 5.11. In this figure, every meteorite is assumed to be one sample of the crystallized core, regardless of the mass of the meteorite. If the mass of each IIIAB meteorite is used, the distribution becomes dominated by the few very large samples. Figure 5.11a shows a histogram of observed IIIAB iron meteorite Ni concentrations and the model predictions from simple fractional crystallization and from mixing scenario 4, the scenario involving non-constant mixing parameters. There are over twice as many high Ni IIIAB iron meteorites as predicted by either model, suggesting either the high Ni IIIAB iron meteorites are delivered to Earth in numbers not representative of their one time abundance in the IIIAB parent body core or both models fail to match the observed frequency distribution. Figure 5.11b is a histogram of Ir concentrations, and similar to Ni concentrations, the distribution from a simple fractional crystallization model drops off too quickly and predicts far fewer low Ir IIIAB meteorites than actually exist. Calculations from mixing scenario 4 produce a distribution for Ir concentrations which resembles simple fractional crystallization except for the addition of a second peak at
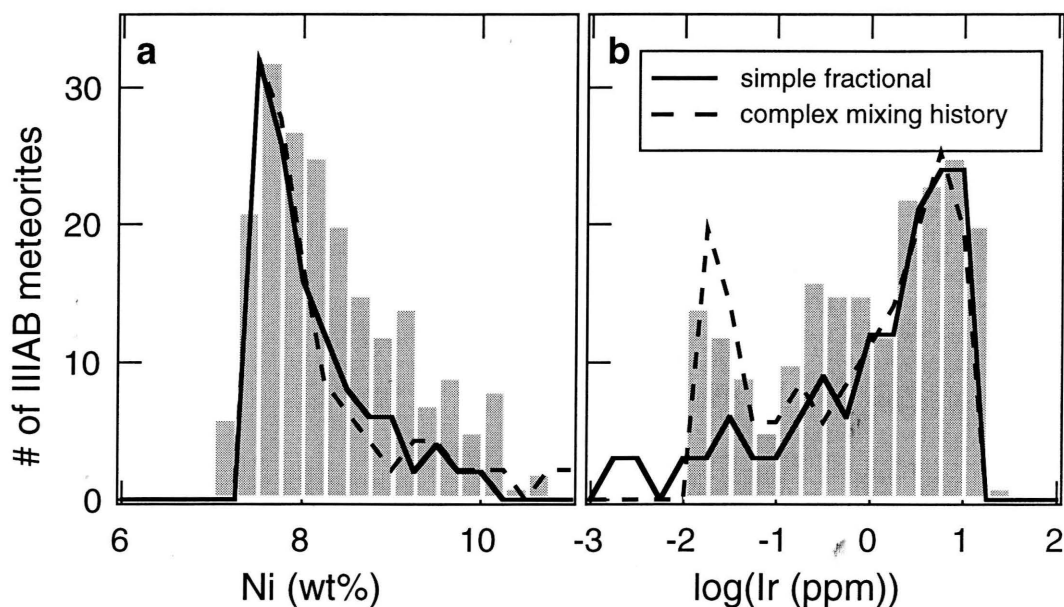
FIG. 5.11. The actual number of IIIAB meteorites at each (**a**) Ni and (**b**) Ir concentration are compared to the predicted number of meteorites from models of simple fractional crystallization and mixing scenario 4, the mixing scenario with the complex crystallization history. Model calculations were done in equal mass steps, and if each IIIAB meteorite is considered to be a random sized sample from a random location in the IIIAB parent body's core, the actual number of IIIAB meteorites should match the model predictions. In actuality, there is an overabundance of late stage crystallizing meteorites relative to model predictions. For mixing scenario 4, the leveling off of the Ir concentration is shown as a second peak in the predicted distribution. This second Ir peak is perhaps suggested in the actual IIIAB distribution, though the second Ir peak produced by mixing scenario 4 is larger than the observed distribution and not enough meteorites are predicted at intermediate Ir concentrations.

low Ir concentrations, corresponding to the buffering of Ir concentrations. The distribution produced by mixing scenario 4 is closer to the observed abundance of IIIAB iron meteorites, though it still predicts fewer meteorites than exist for the Ir range between the two peaks.

The general shape of both model distributions is in agreement with the observed IIIAB distribution shape, peaking initially and then decreasing. The model distributions evolve too quickly, producing fewer late stage crystallizing meteorites than our meteorite collections contain. Perhaps removing S from the system, into S-rich boundary layers, as suggested by Haack and Scott (1993), could slow the liquid evolution and produce a more gradual decrease in the predicted distributions. The amount of eutectic composition liquid could also be decreased, as Haack and Scott (1993) demonstrated, but a different S-rich reservoir would be created.

5.5.2 Inward versus Outward Crystallization

As Fig. 5.3 illustrates, three out of the four mixing scenarios crystallize the molten core from the core/mantle boundary inward. Haack and Scott (1992) have suggested that there are physical reasons which necessitate the method of inward crystallization for metallic cores of asteroid-sized bodies. In mixing scenarios 2-4, the core is chosen to crystallize inward so it will remain gravitationally stable. As solid metal crystallizes, *Zone 1*, the crystallizing liquid, is enriched in S and consequently less dense than it was initially. *Zone 2* is not involved in crystallization, and its S-content is always less than

or equal to the S-content of *Zone 1*. The denser liquid, *Zone 2*, must be beneath the lighter, crystallizing liquid of *Zone 1*, suggesting inward crystallization.

However, inward crystallization of the metallic core of the IIIAB parent body complicates the formation of pallasites. To explain their mixture of olivine and metal, a core/mantle boundary origin has been proposed for pallasites. The trace element composition of the metal in main group pallasites resembles the composition of late stage crystallizing members of the IIIAB iron meteorite group (Scott, 1977). If the IIIAB core crystallized from the core/mantle boundary inward, there is the added difficulty of transporting late stage evolved metallic liquid from the central region of the core, through the crystallized solid, to the core/mantle boundary to combine with olivine and form pallasites.

5.5.3 Other Magmatic Groups

Three other magmatic iron meteorite groups were studied to examine the extent to which mixing effects are necessary to reproduce crystallization trends from other parent bodies. Figure 5.12 shows the Ge versus Ir trends for the IIAB, IVB, and IVA magmatic iron meteorite groups, with the Ir scale for each group being different. Simple fractional crystallization trends were calculated for each group as were trends from all four mixing scenarios. The mixing scenarios used the initial parameters given in Table 5.3, even though these parameters were optimized to reproduce the IIIAB trend. Starting concentrations for each group are given in Table 5.1. The S-content of the molten core has a significant effect on the resulting trends, and consequently, the S-content for each

magmatic group was taken from previous studies (Jones and Drake, 1983; Scott et al., 1996) which determined the initial S concentration of the metallic core by modeling many different elements simultaneously.

The IIAB trend, similar to the IIIAB trend, exhibits a well-defined leveling off of Ir concentrations, shown in Fig. 5.12a. The IIAB meteorite data are from Wasson (1974), Kracher et al. (1980), Malvin et al. (1984), and Wasson et al. (1989). Simple fractional crystallization can not reproduce the late stage crystallizing portion of the trend while all four mixing scenarios buffer Ir concentrations and produce trends which level off. Mixing scenario 1, the boundary layer case, reproduces the IIAB trend the best. Malvin (1988) modeled the IIAB group using an assimilation-fractional crystallization model, which would produce a trend indistinguishable from mixing scenario 1 and consequently also match the IIAB meteorites. Thus the IIAB group, like the IIIAB, requires a more complex explanation than simple fractional crystallization. A process which uses two reservoirs of liquids to effectively buffer element concentrations can reproduce the observed IIAB Ge versus Ir trend. However, an initial S-content of 17 wt% is used in all model calculations, leaving over 60% of the core with an Fe-FeS eutectic composition.

The scattered trends of the IVB iron meteorite group have been explained by simple fractional crystallization of a S-free metallic liquid (Rasmussen et al., 1984). The limited IVB meteorite data are from Wasson (1974) and Kracher at al. (1980). As is shown on Fig. 5.12b, all four mixing scenarios produce similar trends to simple fractional crystallization and, consequently, fit the scattered IVB meteorites as well as

simple fractional crystallization. For elements such as Ir, in a S-free system the partition coefficient is closer to 1.0 and the resulting range of element concentrations produced is much less than in a system containing S. Comparing Fig. 5.12a with Fig. 5.12b, the S-free IVB trend contains Ir concentrations which vary between 10 to 40 ppm while the Ir concentrations in the IIAB group, which has an initial S-content of 17 wt%, range over 3 orders of magnitude. With a partition coefficient closer to 1.0, the effects of mixing are negligible since the molten core does not become as depleted in elements such as Ir, for example. Thus, the IVB iron meteorite group does not require any buffering from mixing effects to reproduce the observed crystallization trends, but including the effects of mixing still reproduces the crystallization trends.

The Ge versus Ir trend for the IVA magmatic group is shown in Fig. 5.12c. References for the IVA meteorite data are given in Table A1 of Scott et al. (1996). As for the IVB group, trends from the mixing scenarios and simple fractional crystallization calculations are similar. However, none of these five model calculations are able to reproduce the observed late stage crystallizing portion of the IVA trend. Scott et al. (1996) had previously noticed the inability of simple fractional crystallization to reproduce this portion of the IVA trend, and consequently attempted to model the trend with a more complex crystallization history. In the model of Scott et al., the solid core crystallized inward, but a region in the center of the molten liquid retained its original composition. This original composition liquid was then added to the crystallizing liquid in amounts of 1% of the remaining liquid. This model is conceptually similar to mixing scenarios 2, 3, and 4. However, an important difference
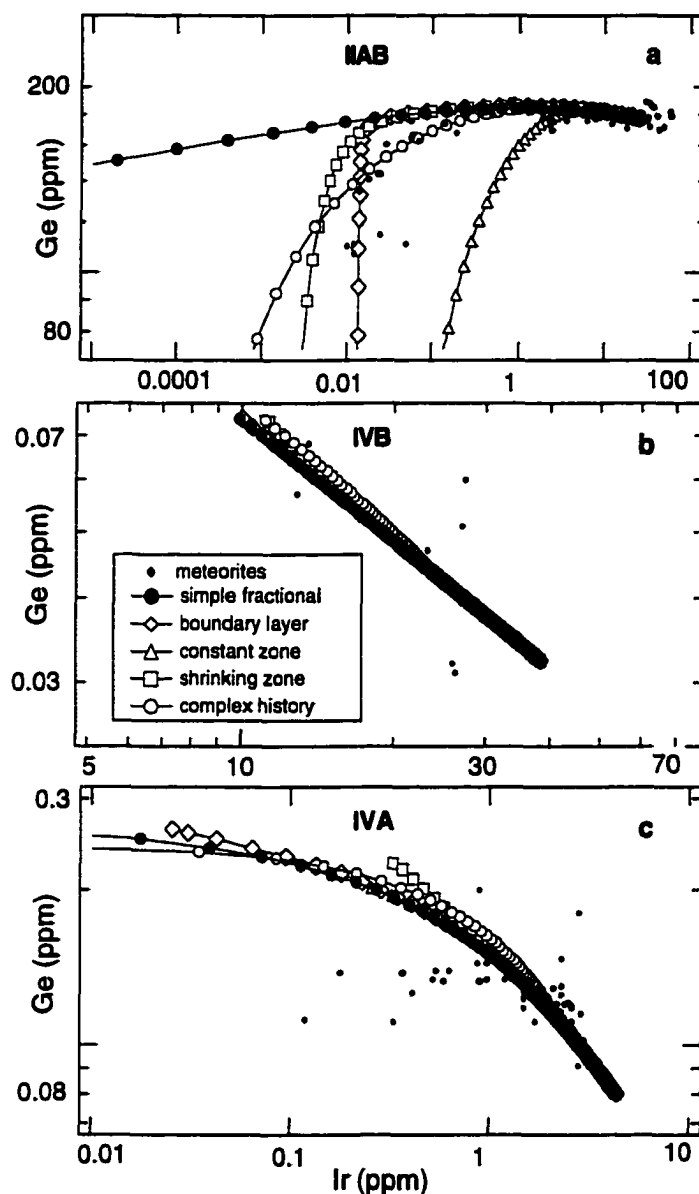
Fig. 5.12. Other magmatic iron meteorite groups were modeled to examine if the effects of mixing were present in other crystallizing cores. (a) The IIAB Ge versus Ir trend is similar to the trend of the IIIAB group; the trend is not fit by simple fractional crystallization while some mixing scenarios do produce trends which match more closely the observed meteorite abundances. (b) The IVB meteorite group shows trends which are fit equally well by simple fractional crystallization or any of the mixing scenarios in a S-free system. (c) The Ge versus Ir trend for the IVA iron meteorites is not matched by simple fractional crystallization or any of the four mixing scenarios. Some process besides simple fractional crystallization is necessary to explain the late stage crystallizing members of the IVA group.

is that Scott et al. used a D_S which changed during the crystallization process and ranged from approximately 0.01 to 1.0. Like the dendritic crystallization model of Haack and Scott (1993), this fictive D_S was meant to account for S being removed from the crystallizing system by S-rich pockets and boundary layers. Because of their choice for D_S, Scott et al. calculated that this method of crystallization would initially only involve the upper 2% of the entire molten core and admitted that this was consequently not a probable method of crystallization. Nevertheless, the concept is similar to the mixing models investigated here since it involves mixing a different composition liquid into the crystallizing portion of the molten core. This model, however, did not successfully reproduce the IVA trend, and Scott et al. concluded that some kind of liquid mixing model may account for the poorly matched portion of the trend. The four mixing scenarios examined with this mixing model are unable to reproduce the IVA Ge versus Ir trend. Some process besides simple fractional crystallization is necessary to explain the late stage crystallizing members of the IVA group, though the effects of mixing, as they are modeled in this chapter, are not sufficient.

5.6 Summary

Simple fractional crystallization calculations do not reproduce the late stage crystallizing portion of the Ge versus Ir trend for the IIIAB iron meteorites. The mixing model developed in this chapter, which divides the molten core into two zones of liquid and then allows interactions between these two zones, can match the IIIAB Ge versus Ir trend, including the late stage crystallizing portion. This model does not suggest a

unique method of core crystallization since four significantly different crystallization scenarios can reproduce the Ge versus Ir trend. The most complex of these four scenarios, which involves an inwardly crystallizing core with an initially high rate of mixing that decreases as crystallization proceeds, reproduces the IIIAB trends the best. The point of the modeling in this work is not to determine a specific scenario of core crystallization but rather to examine the effects of mixing. A metallic core which does not have all its liquid actively involved in crystallization leaves the possibility for mixing within the molten portion. Such mixing can effectively buffer element concentrations and consequently reproduce magmatic iron meteorite trends.

Other models of crystallization have been developed to explain the IIIAB iron meteorites. An assimilation-fractional crystallization model by Malvin (1988) is mathematically similar to mixing scenario 1, the boundary layer scenario developed in this chapter, and is able to reproduce the IIIAB Ge versus Ir trend. The plausibility of adding unfractionated liquid from the mantle throughout core crystallization has been questioned, but as in the mixing model, two reservoirs of liquid can effectively buffer element concentrations. A model by Haack and Scott (1993), which attempts to account for the effects of dendritic crystallization, fails to reproduce the Ge versus Ir trend in a way similar to simple fractional crystallization, even if dendritic crystallization may be the method by which a metallic core in an asteroid-sized body solidifies. Liquid immiscibility, as modeled by Ulff-Møller (1998), also can not reproduce the entire IIIAB trend, though as Ulff-Møller showed, liquid immiscibility can have a significant effect on the solid metal which crystallizes. Discrepancies also exist between model

predictions and the IIIAB samples in meteorite collections; there is an overabundance of late stage crystallizing IIIAB members and a lack of S-rich meteorites in the meteorite collections compared to the predictions of the crystallization models.

Other magmatic iron meteorite groups also suggest another process besides simple fractional crystallization, such as mixing, is necessary to explain the entire shape of the observed crystallization trends. The IIAB group is fit well by the mixing scenarios developed in this chapter to explain the IIIAB trends. The IVB group is equally well modeled by either simple fractional crystallization or any of the four mixing scenarios in a S-free molten core. The Ge versus Ir trend of the IVA group is not reproduced by simple fractional crystallization or the mixing scenarios but does suggest a process occurred during core solidification which affected the composition of the metal formed during the final stages of crystallization.

CHAPTER 6

LIQUID IMMISCIBILITY DURING CORE CRYSTALLIZATION

Magmatic iron meteorites are commonly thought to have formed by fractional crystallization of the metallic cores of asteroid-sized bodies, for reasons discussed in Chapter 1. As fractional crystallization proceeds, light elements such as P and S are enriched in the molten portion of the core, and, consequently, liquid immiscibility may be encountered. I have conducted experiments with three phases, solid metal and two immiscible metallic liquids, to determine the location of the liquid immiscibility field near conditions thought to be relevant to magmatic iron meteorites. My results show a significant suppression of the liquid immiscibility field as compared to the previously published Fe-P-S phase diagram. My revised phase diagram suggests that liquid immiscibility was encountered during the crystallization of asteroidal cores, but much later during the crystallization process than predicted by the previously published diagram.

6.1 Motivation

Elemental trends observed in magmatic iron meteorite groups are commonly attributed to fractional crystallization of asteroidal cores (Scott, 1972). Though simple fractional crystallization cannot reproduce all of the observed elemental trends, more complex models are, fundamentally, just variations on simple fractional crystallization (e.g., Chabot and Drake, 1999). In all models, as fractional crystallization proceeds, elements such as P and S, which are incompatible in the crystallizing solid, become enriched in the molten portion of the core.

Depending on the levels of enrichment, liquid immiscibility may occur, causing the molten portion of the core to form two metallic liquids, one P-rich and one S-rich, rather than just a single metallic liquid. The onset of liquid immiscibility could cause the core to separate into two layers, the lower of which would be the denser P-rich liquid, or the two immiscible liquids could remain intimately mixed throughout the core. In either case, modeling by Ulff-Møller (1998) has shown elemental trends resulting by crystallization from two liquids differ significantly from crystallization trends formed from only one liquid.

Figure 6.1 shows the paths of the molten portion of the core as modeled by simple fractional crystallization for the IIAB (Jones and Drake, 1983), IIIAB (Chabot and Drake, 1999), and IVA (Scott et al., 1996) magmatic iron meteorite groups. Also shown in Fig. 6.1 is the shaded field of solid metal and one metallic liquid, taken from the Fe-P-S phase diagram (Raghvan, 1988). Figure 6.1 clearly shows that the paths of the iron

へ
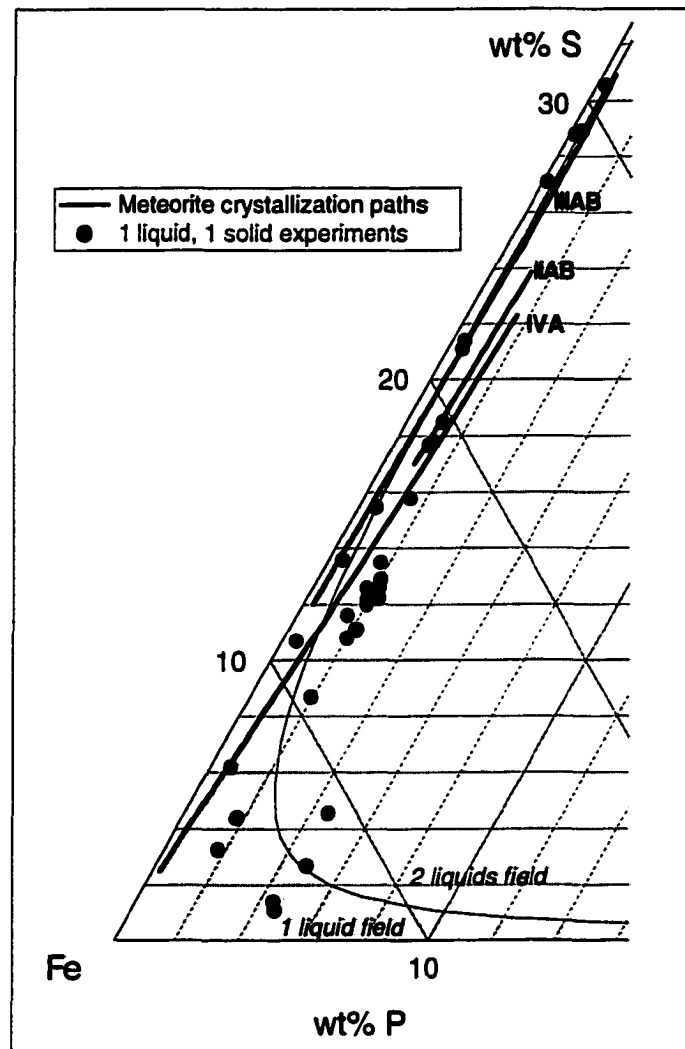
FIG. 6.1. The compositional evolution of the molten portion of the core as modeled by simple fractional crystallization is plotted for the IIAB (Jones and Drake, 1983), IIIAB (Chabot and Drake, 1999), and IVA (Scott et al., 1996) magmatic iron meteorite groups on the Fe-rich corner of the Fe-P-S system (Raghvan, 1988). According to the Fe-P-S phase diagram, the meteorite crystallization trends encountered the two liquids field and experienced liquid immiscibility. The metallic liquid compositions from solid metal/liquid metal partitioning experiments (Jones and Drake, 1983; Malvin et al., 1986) are also plotted on the Fe-P-S system, and though the experiments contained only one liquid and one solid, many of the resulting liquid compositions fall in the two liquids field. If the cores of the iron meteorite parent bodies experienced similar conditions to those of the experiments, liquid immiscibility might have been similarly suppressed during the crystallization of iron meteorites.

meteorite groups evolve into the field of two immiscible liquids. However, experiments designed to examine the partitioning of trace elements in iron meteorites have reported metallic liquid compositions inconsistent with the Fe-P-S phase diagram (Jones and Drake, 1983; Malvin et al., 1986). The experiments contained one liquid and one solid, and the compositions of the metallic liquids formed in each of the experiments are also plotted in Fig. 6.1. Though each experiment contained just a single liquid, many of the experimental compositions plot in the two liquids field.

If the experiments are relevant to the crystallization of iron meteorites, liquid immiscibility might have been similarly suppressed in the crystallizing cores of the iron meteorite parent bodies. To help determine to what extent liquid immiscibility was involved in the crystallization of magmatic iron meteorites, I have conducted experiments which contained three phases, solid metal and two metallic liquids. With these experiments, I have determined the location of the two liquids field in the Fe-P-S system at conditions which are believed to be relevant to the crystallization of magmatic iron meteorites.

6.2 Experimental and Analytical Methods

The experiments were conducted using a technique similar to that of Jones and Drake (1983) and are listed on Table 6.1. Mixtures of dominantly Fe, Ni, FeS, and P were prepared, and 200-500 mg of each mixture was contained in a ~5 mm diameter, ~2 cm tall alumina crucible. The crucible was inserted into a high purity silica glass tube that was 9 mm in inner diameter with 2 mm thick walls. Each tube was evacuated and

sealed before being lowered into a Deltech vertical tube furnace. The furnace was ramped up to temperatures ranging from 1050–1200°C and held at the desired run temperature for at least a week. Samples were quenched by removing the silica tube from the furnace and immersing the tube in water.

In three of the experiments, marked with stars in Table 6.1, a second crucible which contained pure Fe was placed below the crucible containing the sample mixture. The purpose of the second crucible was to buffer the oxygen fugacity near the IW (iron-wüstite) level. However, all experiments contained a solid Fe-rich metallic phase, which would also serve to maintain oxygen fugacities near the IW level. Experiments whose run number begins with the letter E also contained small amounts of trace elements in the starting mixture.

After quenching, samples were mounted, cut, and polished to prepare them for microprobe analysis. All experiments consisted of three phases: a solid Fe-Ni phase, a P-rich metallic liquid, and a S-rich metallic liquid. Figure 6.2 shows three back scattered electron (BSE) images of a run product and the phases produced. As shown in Fig. 6.2b and 6.2c, the P-rich and S-rich metallic phases did not quench to a single homogenous phase but rather formed Fe-dendrites surrounded by interstitial P-rich and S-rich phases. If the two metallic liquids were intertwined in the run product, the dendritic texture of each made it difficult to identify which features were caused by liquid immiscibility at the run conditions and which features were only formed upon quenching. All the experiments listed in Table 6.1 contained substantial amounts of the

TABLE 6.1. Experimental conditions and resulting compositions.

Run #	30*	E1*	E6	E2*	E9
Temp (°C)	1050	1050	1100	1150	1200
Duration	18 days	21 days	12 days	19 days	7 days
Solid					
Fe (wt%)	86.9 ±1.6	82.4 ±0.8	89.2 ±1.4	84.7 ±0.8	84.6 ±1.2
Ni (wt%)	13.4 ±0.3	13.2 ±0.3	10.3 ±0.3	10.7 ±0.3	12.5 ±0.3
P (wt%)	0.90 ±0.05	0.77 ±0.07	0.81 ±0.09	0.62 ±0.05	0.51 ±0.03
P-rich liq.					
Fe (wt%)	76.3 ±0.5	72.7 ±1.3	77.9 ±1.4	76.2 ±0.8	73.3 ±1.1
Ni (wt%)	14.9 ±0.1	15.7 ±0.4	11.1 ±0.4	12.1 ±0.3	12.6 ±0.7
P (wt%)	7.4 ±0.3	7.0 ±1.1	5.9 ±0.6	5.0 ±0.5	3.0 ±0.5
S (wt%)	1.7 ±0.2	1.9 ±0.8	4.8 ±2.1	4.9 ±1.3	9.5 ±2.0
S-rich liq.					
Fe (wt%)	62.6 ±0.9	61.6 ±1.2	63.9 ±1.1	61.6 ±1.3	64.3 ±1.3
Ni (wt%)	7.9 ±0.6	7.4 ±0.7	6.0 ±0.6	6.6 ±0.7	8.7 ±1.0
P (wt%)	0.5 ±0.3	0.31 ±0.08	0.3 ±0.1	0.32 ±0.07	0.5 ±0.2
S (wt%)	29.0 ±1.4	30.0 ±1.3	29.6 ±1.4	29.4 ±1.5	25.0 ±2.2

* Experiments which contained a second crucible of pure Fe as a buffer below the sample crucible.

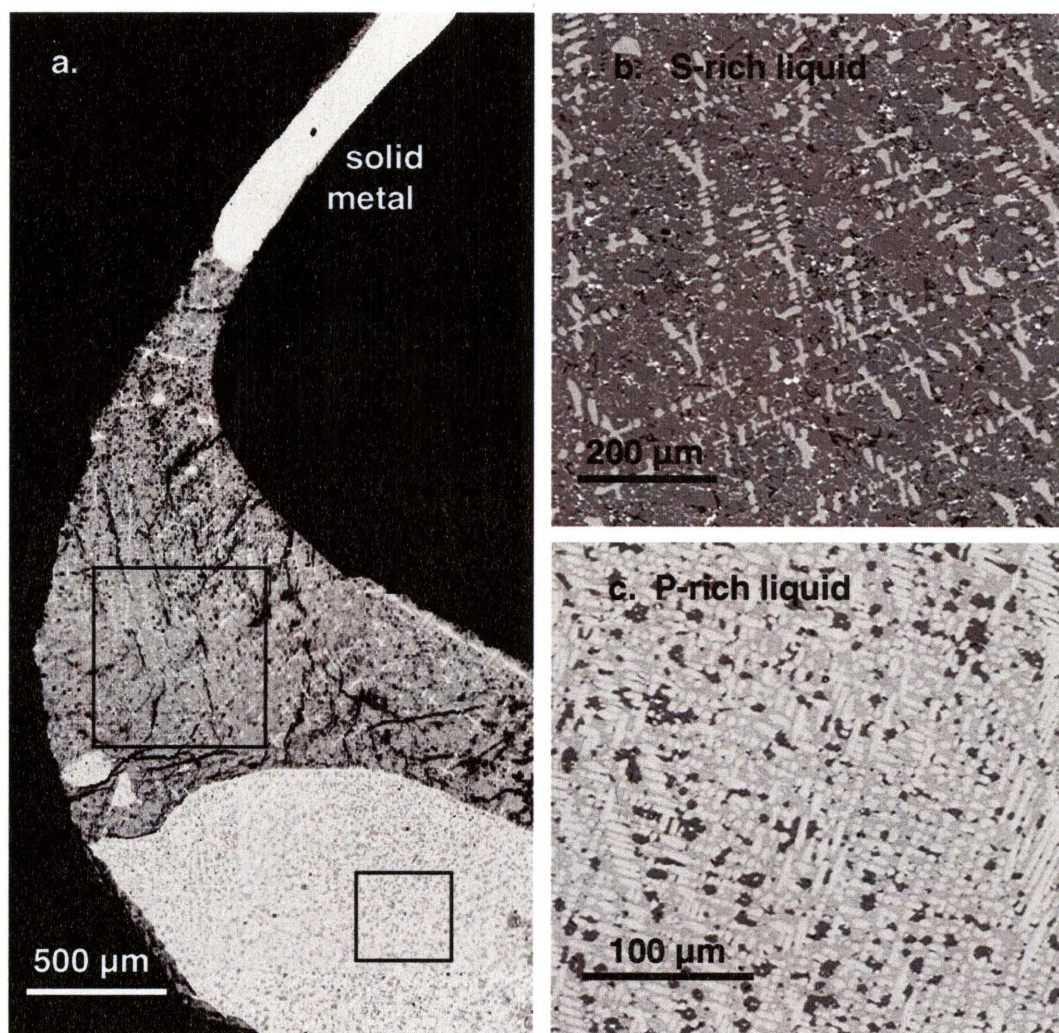**FIG. 6.2.** BSE images of run #E2 are shown. **(a)** Three phases were present in each of the experiments: solid metal and two metallic liquids. Only experiments which showed clear separation of the phases and produced enough of each phase to yield good microprobe results were used. The **(b)** S-rich and **(c)** P-rich metallic liquids did not quench to a single phase but rather formed a dendritic texture.

two metallic liquids and showed clear separation of the phases. Experiments which did not meet these criterion were not used.

All experiments were analyzed for Fe, Ni, P, and S using the electron microprobe with a voltage of 15 kV, a beam current of 20 nA, and a counting time of 20 sec. Except for S in the solid metallic phase, concentrations of these four elements were high enough to be easily measured with the electron microprobe. Instead, analysis was complicated by the dendritic texture of the P-rich and S-rich liquids. Consequently, a raster beam of 16 μm was used for all measurements. To determine the bulk composition of the P-rich and S-rich metallic liquids, 40 to 80 individual raster beam measurements were averaged. Averaging many measurements from a raster beam of this size has been shown through image processing to accurately measure the bulk compositions of similar dendritic textures (Chabot and Drake, 1997).

Table 6.1 lists the microprobe measurements for each run along with the errors. For the solid metallic phase, the error was calculated as twice the standard deviation of multiple measurements. However, for the two metallic liquids which did not quench to a single homogenous texture, the variation between each measurement does not indicate how accurately the bulk composition can be determined. Consequently, twice the standard deviation of the mean of multiple microprobe measurements was used to represent the error in the compositions determined for the metallic liquid phases.

6.3 Results and Discussion

Figure 6.3a plots the P and S concentrations of the two metallic liquids for the experiments. The P-rich metallic liquid and the S-rich metallic liquid are connected by a tie-line for each experiment. The location of the one solid and one liquid field according to the Fe-P-S phase diagram (Raghvan, 1988) is shown as a shaded region on Fig. 6.3a, and if my three phase experiments formed liquid compositions in agreement with the Fe-P-S phase diagram, my experimental points should fall on the boundary of the shaded and unshaded regions of Fig. 6.3a. However, even with the large $\pm 2\sigma$ error bars due to the difficulty in analyzing the dendritic quench texture of the metallic liquids, my three phase experiments show a smaller liquid immiscibility field than that predicted by the Fe-P-S phase diagram.

The liquid immiscibility field of the published Fe-P-S phase diagram (Raghvan, 1988) is based largely on the work of Schürmann and Schäfer (1968) and Schürmann and Neubert (1980). Their experiments were run in an Ar atmosphere and analysis of the composition of each phase was done using wet chemistry techniques. The largest errors associated with the determination of the composition of each phase are ± 0.08 wt% for P and ± 0.05 wt% for S (Schürmann, personal communication). Thus, the discrepancy between my three phase experiments and the published Fe-P-S phase diagram can not be accounted for by the estimated errors in the experiments used to create the published phase diagram.

The two liquids field suggested by my experiments is shown as a dashed line in Fig. 6.3a and is in good agreement with the results of previous solid metal/liquid metal

experiments (Jones and Drake, 1983; Malvin et al., 1986). The metallic liquid compositions of the previous solid metal/liquid metal experiments are plotted in Fig. 6.3a. Though the previous experiments contained just one metallic liquid, their metallic liquid compositions do not all lie within the shaded one liquid, one solid field suggested by the published Fe-P-S phase diagram but do all lie within the one liquid field suggested by my experiments. Figure 6.3a also shows the previous one liquid, one solid experiments with different symbols for different experimental conditions. Eighteen experiments were conducted at 1250°C, nine at IW (iron-wüstite) and nine at QFI (quartz-fayalite-iron). At the conditions of the experiments, QFI is approximately half an order of magnitude below IW. As shown in Fig. 6.3a, the difference in oxygen fugacity did not appear to affect the resulting metallic liquid composition in the experiments. Experiments conducted at IW and QFI produced similar metallic liquid compositions, both of which were inconsistent with the Fe-P-S phase diagram of Raghvan (1988).

The discrepancy between the Fe-P-S phase diagram of Raghvan (1988) and the metallic liquid compositions of the previous experiments was first attributed to the affect of Ni on Fe-P-S system (Jones and Drake, 1983). However, Malvin et al. (1986) noted that starting compositions which did not produce two immiscible liquids in experiments run at an oxygen fugacity near IW did encounter liquid immiscibility when run in a much more reducing atmosphere of Ar-H_2. Since Ni was present in both circumstances, Malvin et al. (1986) concluded that the effect of oxygen fugacity on the Fe-P-S system, not the presence of Ni, was the explanation for the difference between

the experimental liquid compositions and the Fe-P-S phase diagram. Unfortunately, the experiments conducted in an Ar-H_2 atmosphere experienced a significant amount of S loss due to being conducted in open crucibles, complicating direct comparisons between the two types of experiments conducted at different oxygen fugacities.

Experiments run in an Ar atmosphere, such as those of Schürmann and Schäfer (1968) and Schürmann and Neubert (1980), may have experienced a more reducing environment than experiments conducted near IW, and the effect of oxygen fugacity on the Fe-P-S system may explain the discrepancy between the two sets of experiments. However, my interest is to apply the Fe-P-S phase diagram to the crystallization of magmatic iron meteorites. A study of phosphate minerals in IIIAB iron meteorites concluded the oxygen fugacity was below the IW level, but "did not represent extreme reduction such as seen in enstatite chondrites and achondrites" (Olsen et al., 1999). It has also been stated that an oxygen fugacity 0.5-1 order of magnitude below the QFI level can "account for the O-bearing phases in IIIAB irons" (Ulff-Møller, 1998). As a metallic core crystallizes, O, like S and P, will be excluded from the crystallizing solid and enriched in the molten portion of the core; though this effect may not be very large, the crystallizing environment will only become more oxidizing, not more reducing, as crystallization proceeds (Kracher, 1983).

Experiments at both IW and QFI show significant suppression of the liquid immiscibility field as compared to the Fe-P-S phase diagram of Raghvan (1988) and are near the oxygen fugacity thought to be relevant to magmatic iron meteorites. Thus, the
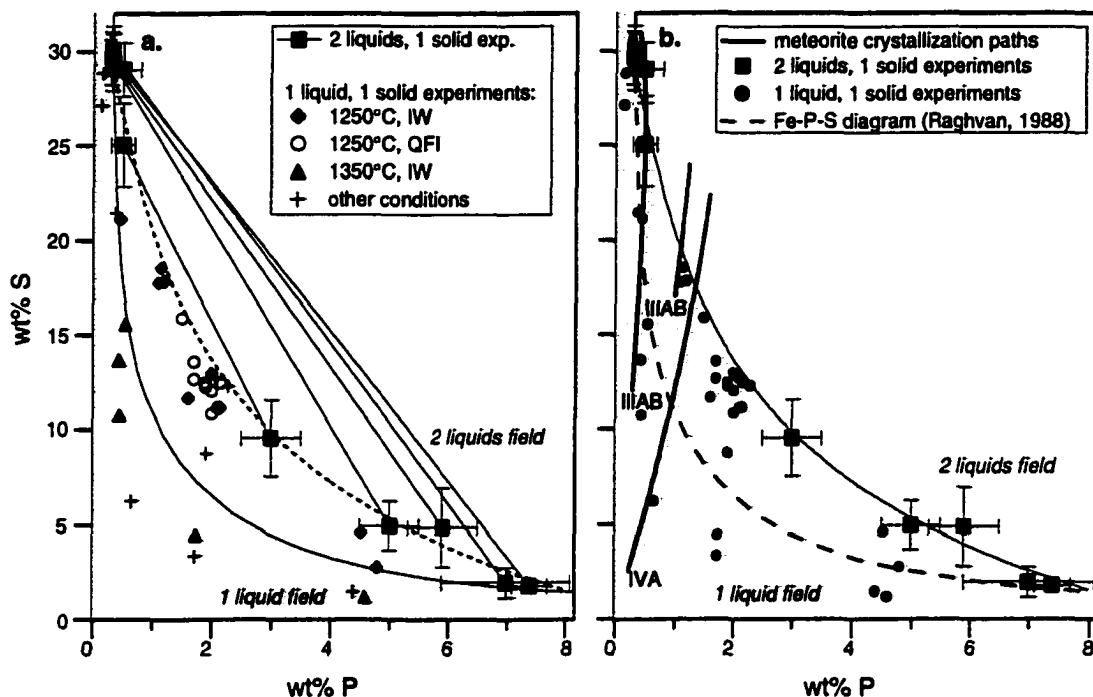
FIG. 6.3. (a) The compositions of the two metallic liquids produced in each of the three phase experiments are plotted with $\pm 2\sigma$ error bars and connected by tie lines. The three phase experiments suggest a much larger one liquid, one solid field, shown as a dashed curve, than indicated on the Fe-P-S phase diagram (Raghvan, 1988), shown as the shaded region. The liquid compositions from previous experiments which contained just one liquid and one solid (Jones and Drake, 1983; Malvin et al., 1986) do not all fall within the shaded one liquid field of the Fe-P-S phase diagram. However, the previous two phase experiments conducted at both IW and QFI are consistent with the liquid immiscibility field suggested by my three phase experiments. (b) The one liquid, one solid field defined by my three phase experiments is shaded, and the compositional paths of the molten portion of the core during simple fractional crystallization for the IIAB (Jones and Drake, 1983), IIIAB (Chabot and Drake, 1999), and IVA (Scott et al., 1996) magmatic iron meteorite groups are shown. Even using the liquid immiscibility field suggested by my three phase experiments, the crystallization paths of the iron meteorites still encounter the two liquids field, just at a significantly different composition than suggested by the previously published Fe-P-S phase diagram.

role of liquid immiscibility in crystallizing asteroidal cores may not have been as large as the published Fe-P-S phase diagram would suggest. Figure 6.3b shows the simple fractional crystallization trends of three magmatic iron meteorite groups with the one liquid, one solid field implied from my three phase experiments shaded. The crystallization paths of the iron meteorites still encounter the two liquids field but at a much different composition than suggested by the Fe-P-S phase diagram of Raghvan (1988). Models more involved than simple fractional crystallization have been developed to better explain the observed elemental trends in magmatic iron meteorites (e.g., Chabot and Drake, 1999), but these models are essentially variations on simple fractional crystallization. In all models, as fractional crystallization proceeds, P and S become enriched in the molten portion of the core, and depending on the levels of enrichment, liquid immiscibility may occur. Thus, liquid immiscibility may not occur until significantly later in the crystallization process than predicted by the Fe-P-S phase diagram of Raghvan (1988) but still may affect the late-stage crystallizing portion of the asteroidal core.

6.4 Summary

Three phase experiments conducted near IW define a larger one liquid, one solid field than shown on the Fe-P-S phase diagram of Raghvan (1988). The liquid immiscibility field suggested by my three phase experiments is in good agreement with previous solid metal/liquid metal experiments which produced liquid compositions inconsistent with the published Fe-P-S phase diagram. The difference between the solid

metal/liquid metal experiments and the phase diagram has been attributed to the effect of oxygen fugacity on the Fe-P-S system. The effect of oxygen fugacity may explain the discrepancy, but experiments at IW and QFI both show a significantly smaller liquid immiscibility field as compared to the Fe-P-S phase diagram of Raghvan (1988), and an oxygen fugacity slightly below QFI is thought to be relevant to the crystallization of magmatic iron meteorites. Thus, if the experimental conditions are near the conditions present during the crystallization of magmatic iron meteorites, the role of liquid immiscibility in crystallizing asteroidal cores may not have been as large as the Fe-P-S phase diagram of Raghvan (1988) would suggest. However, simple fractional crystallization models for three magmatic iron meteorite groups still indicate that all three groups will encounter liquid immiscibility, even using the revised phase diagram defined by my experiments, just much later during the crystallization process than the previously published phase diagram implies.

CHAPTER 7

SUMMARY

From both experimental and theoretical geochemical studies, my research has improved our understanding of the nature of the metallic cores of terrestrial planetary bodies. Specifically, the following questions have been addressed:

• Is the decay of radioactive K an important heat source in the cores of terrestrial planetary bodies?

• How does the evolution of metallic cores affect the distribution of element pairs important to chronometry in iron meteorites?

• What is the method of core crystallization in asteroid-sized bodies?

• How significant is the role of liquid immiscibility during the evolution of metallic cores?

To determine the importance of K as a heat source in planetary cores, metal/silicate partitioning experiments were conducted. The presence of S in the metallic liquid was found to increase the K concentration in the metal to a level detectable with the electron microprobe. Sulfur-free metal or C-rich metal contained K concentrations too low to be measured. The silicate composition was discovered to affect the metal/silicate partitioning behavior of K, with D_K increasing by nearly two orders of magnitude with increasing depolymerization of the silicate melt. However, despite this increase, my experiments show no evidence for significant solubility of K in metal. The implied concentration of K in the Earth's core from my experiments is less than 1 ppm and

would provide ~10^{10} W, which is 2-3 orders of magnitude lower than estimates of the power necessary to drive the Earth's geodynamo. Although my work shows no indication that K is an important heat source in planetary cores, additional experiments at higher pressures and temperatures would be worthwhile.

During the evolution of metallic cores, elements will partition between solid and liquid metal. The concentrations of S and P in the metallic liquid will affect the partitioning of Ag, Pd and Re, Os, two element pairs used to date early solar system events. My experimental work shows as the S-content of the metallic liquid increases, the solid metal/liquid metal partition coefficient of Pd increases but that of Ag decreases. Phosphorus has no effect on the partitioning behavior of Ag or Pd, but both Re and Os increase with increasing P concentration in the metallic liquid. With this new understanding of the effect of S and P on the partitioning behavior, the Pd trends in iron meteorite groups can be explained for the first time. The concentration of Ag in troilite-rich nodules also agrees well with my experimental results, though the Pd abundances in troilite-rich nodules remain unexplained.

Elemental trends in iron meteorite groups offer insight into the method of crystallization of the metallic cores of asteroid-sized bodies. I have shown that though simple fractional crystallization appears to reproduce many of the observed elemental trends when plotted versus Ni, on a graph of Ge against Ir, it is clear simple fractional crystallization fails to explain a significant portion of the trend. I have developed a model which allows slight inhomogeneities to exist in the molten core. Mixing then occurs between liquid in the actively crystallizing region and liquid too far from the

crystallization front to be involved in the crystallization process. This model does not suggest a unique method of crystallization, but the most successful crystallization scenarios involve inward crystallization of the core from the core-mantle boundary. This mixing model can reproduce the entire Ge versus Ir trend observed in the IIIAB group, the largest iron meteorite group, while most other proposed crystallization models cannot. The success of this model suggests mixing is an important process during the crystallization of the metallic cores of asteroid-sized bodies.

During the crystallization of a metallic core, light elements such as S and P are enriched in the molten portion of the core, creating the possibility that liquid immiscibility may be encountered. The onset of liquid immiscibility would cause the molten portion of the core to separate into two liquids of different densities, which would significantly affect the subsequent evolution of the core. The published Fe-P-S phase diagram suggests liquid immiscibility was encountered fairly early in the crystallization processes for some iron meteorite groups. My experimental work, conducted near conditions believed to be relevant to magmatic iron meteorites, indicates liquid immiscibility played a much smaller role in the evolution of the cores of asteroid-sized bodies than the published phase diagram implies. Liquid immiscibility may still be encountered by crystallizing metallic cores, but it will be significantly later in their evolution than previously believed.

Each of the four topics which were just discussed can be viewed as an independent project, but together they have investigated many different aspects of the cores of

terrestrial planetary bodies. When the four topics are combined, my research has covered the subjects of:

- The composition of cores following core formation

- The distribution of elements during core evolution

- The crystallization method of cores

- The processes involved during core evolution

The results of this work have provided insight into the nature of the cores of terrestrial planetary bodies and the processes which affect those cores.

REFERENCES

Anderson J.D., Lau E.L., Sjogren W.L., Schubert G., and Moore W.B. (1996a) Gravitational constraints on the internal structure of Ganymede. *Nature* **384**, 541-543.

Anderson J.D., Sjogren W.L., and Schubert G. (1996b) Galileo gravity results and the internal structure of Io. *Science* **272**, 709-712.

Anderson J.D., Lau E.L., Sjogren W.L., Schubert G., and Moore W.B. (1997) Europa's differentiated internal structure: Inferences from two Galileo encounters. *Science* **276**, 1236-1239.

Beatty J.K., Petersen C.C., and Chaikin A. (1999) The New Solar System, fourth edition. Sky Publishing Corporation and Cambridge University Press, Canada, 421 pp.

Binzel R.P. and Xu S. (1993) Chips off of asteroid 4 Vesta: Evidence for the parent body of basaltic achondrite meteorites. *Science* **260**, 186-191.

Bukowinski M.S.T. (1976) The effect of pressure on the physics and chemistry of potassium. *Geophys. Res. Lett.* **3**, 491-494.

Buffett B.A., Huppert H.E., Lister J.R., and Woods A.W. (1996) On the thermal evolution of the Earth's core. *J. Geophys. Res.* **101**, 7989-8006.

Cameron A.G.W. (1986) The impact theory for the origin of the Moon, *in* Origin of the Moon, W.K. Hartmann, R.J. Phillips and G.J. Taylor eds., Lunar and Planetary Institute, Edwards Bros., USA, 609-616.

Carmichael I.S.E., Lange R.A., and Luhr J.F. (1996) Quaternary minettes and associated volcanic rocks of Mascota, western Mexico: A consequence of plate extension above a subduction modified mantle wedge. *Contrib. Mineral. Petrol.* **124**, 302-333.

Capobianco C.J. and Amelin A.A. (1994) Metal-silicate partitioning of nickel and cobalt: The influence of temperature and oxygen fugacity. *Geochim. Cosmochim. Acta* **58**, 125-140.

Capobianco C.J., Jones J.H., and Drake M.J. (1993) Metal-silicate thermochemistry at high temperature: Magma oceans and the "excess siderophile element" problem of the Earth's upper mantle. *J. Geophys. Res.* **98**, 5433-5443.

Chabot N.L. and Drake M.J. (1996) Formation of magmatic iron meteorites by fractional crystallization with metallic magma mixing (abstract). *Meteorit. Planet. Sci.* **31**, A26-A27.

Chabot N.L. and Drake M.J. (1997) An experimental study of silver and palladium partitioning between solid and liquid metal, with applications to iron meteorites. *Meteorit. Planet. Sci.* **32**, 637-645.

Chabot N.L. and Drake M.J. (1998) Solubility of K in metal: Preliminary results of the effects of C, pressure, and temperature. *Mineralogical Magazine* **62A**, 298-299.

Chabot N.L. and Drake M.J. (1999a) Crystallization of magmatic iron meteorites: The role of mixing in the molten core. *Meteorit. Planet. Sci.* **34**, 235-246.

Chabot N.L. and Drake M.J. (1999b) Crystallization of magmatic iron meteorites: The effects of Phosphorus and liquid immiscibility. submitted to: *Meteorit. Planet. Sci.*

Chabot N.L. and Drake M.J. (1999c) Potassium solubility in metal: the effects of composition at 15 kbars and 1900°C on partitioning between iron alloys and silicate melts. *Earth. Planet. Sci. Lett.* **172**, 323-335.

Chen J.H. and Wasserburg G.J. (1983) The isotopic composition of silver and lead in two iron meteorites: Cape York and Grant. *Geochim. Cosmochim. Acta* **47**, 1725-1737.

Chen J.H. and Wasserburg G.J. (1990) The isotopic composition of Ag in meteorites and the presence of ^{107}Pd in protoplanets. *Geochim. Cosmochim. Acta* **54**, 1729-1743.

Chen J.H. and Wasserburg G.J. (1996) Live ^{107}Pd in the early solar system and implications for planetary evolution. *in* Earth Processes: Reading the Isotopic Code, A. Basu and S.R. Hart eds., Geophysical Monograph **95**, American Geophysical Union, Washington, DC, 1-20.

Choi B.G., Ouyang X., and Wasson J.T. (1995) Classification and origin of IAB and IIICD iron meteorites. *Geochim. Cosmochim. Acta.* **59**, 593-612.

Consolmagno G.J. and Drake M.J. (1977) Composition and evolution of the eucrite parent body: Evidence from rare earth elements. *Geochim. Cosmochim. Acta.* **41**, 1271-1282.

Esbensen K.H., Buchwald V.F., Malvin D.J., and Wasson J.T. (1982) Systematic compositional variations in the Cape York iron meteorite. *Geochim. Cosmochim. Acta.* **46**, 1913-1920.

Fleet M.E. and Stone W.E. (1991) Partitioning of platinum-group elements in the Fe-Ni-S system and their fractionation in nature. *Geochim. Cosmochim. Acta* **55**, 245-253.

Fuchs L.H. (1966) Djerfisherite, alkali copper-iron sulfide: A new mineral from enstatite chondrites. *Science* **153**, 166-167.

Ganguly J. and Kennedy G.C. (1977) Solubility of K in Fe-S liquid, silicate-K-(Fe-S)[liq] equilibria, and their planetary implications. *Earth Planet. Sci. Lett.* **35**, 411-420.

Gaffey M.J., Bell J.F., and Cruikshank D.P. (1989) Reflectance spectroscopy and asteroid surface mineralogy, *in* Asteroids, R.P. Binzel, T. Gehrels, and M.S. Matthews eds., University of Arizona Press, Tucson, Arizona, USA, 98-127.

Graham A.L., Bevan A.W.R., and Hutchison R. (1985) *Catalogue of Meteorites.* 4th ed., British Museum (Natural History), London. 460 pp.

Goettel K.A. (1972) Partitioning of potassium between silicates and sulphide melts: Experiments relevant to the Earth's core. *Phys. Earth Planet. Inter.* **6**, 161-166.

Goettel K.A. and Lewis J.S. (1973) Comments on a paper by V.M. Oversby and A.E. Ringwood. *Earth Plant. Sci. Lett.* **18**, 148-150.

Goettel K.A. (1976) Models for the origin and composition of the Earth, and the hypothesis of potassium in the Earth's core. *Geophys. Surv.* **2**, 369-397.

Gubbins D., Masters T.G., and Jacobs J.A. (1979) Thermal evolution of the Earth's core. *Geophys. J. R. Astr. Soc.* **59**, 57-99.

Haack H. and Scott E.R.D. (1992) Asteroid core crystallization by inward dendritic growth. *J. Geophys. Res.* **97**, 14727-14734.

Haack H. and Scott E.R.D. (1993) Chemical fractionations in group IIIAB iron meteorites: Origin by dendritic crystallization of an asteroidal core. *Geochim. Cosmochim. Acta* **57**, 3457-3472.

Hall H.T. and Murthy V.R. (1971) The early chemical history of the Earth: Some critical elemental fractionations. *Earth Planet. Sci. Lett.* **11**, 239-244.

Haughton D.R., Roeder P.L, and Skinner B.J. (1974) Solubility of sulfur in mafic magmas. *Econ. Geol.* **69**, 451-467.

Hillgren V.J., Drake M.J., and Rubie D.C. (1994) High-pressure and high-temperature experiments on core-mantle segregation in the accreting Earth. *Science* **264**, 1442-1445.

Hillgren V.J., Drake M.J., and Rubie D.C. (1996) High pressure and high temperature metal-silicate partitioning of siderophile elements: The importance of silicate liquid composition. *Geochim. Cosmochim. Acta* **60**, 2257-2263.

Hoashi M., Brooks R.R., and Reeves R.D. (1993) Palladium, platinum and ruthenium in iron meteorites and their taxonomic significance. *Chemical Geology* **106**, 207-218.

Ito E. and Morooka K. (1993) Dissolution of K in molten iron at high pressure and temperature. *Geophys. Res. Lett.* **20**, 1651-1654.

Jacobs J.A. (1992) Deep Interior of the Earth. Chapman and Hall, UK, 167 pp.

Jagoutz E., Palme H., Baddenhausen H., Blum K., Cendales M., Dreibus G., Spettel B., Lorenz V., and Wänke H. (1979) The abundances of major, minor, and trace elements in the Earth's mantle as derived from primitive ultramafic nodules. *Proc. Lunar. Planet. Sci. Conf.* **10**, 2031-2050.

Jana D. and Walker D. (1997) The influence of silicate melt composition on distribution of siderophile elements among metal and silicate liquids. *Earth Planet. Sci. Lett.* **150**, 463-472.

Jarosewich E. (1990) Chemical analyses of meteorites: A compilation of stony and iron meteorite analyses. *Meteoritics* **25**, 323-327.

Jones J.H. and Drake M.J. (1983) Experimental investigations of trace element fractionation in iron meteorites, II: The influence of sulfur. *Geochim. Cosmochim. Acta* **47**, 1199-1209.

Jones J.H. and Drake M.J. (1986) Geochemical constraints on core formation in the Earth. *Nature* **322**, 221-228.

Jones J.H. and Malvin D.J. (1990) A nonmetal interaction model for the segregation of trace metals during solidification of Fe-Ni-S, Fe-Ni-P, and Fe-Ni-S-P alloys. *Metall. Trans. B* **21B**, 697-706.

Jones J.H., Hart S.R., and Benjamin T.M. (1993) Experimental partitioning studies near the Fe-FeS eutectic, with an emphasis on elements important to iron meteorite chronologies (Pb, Ag, Pd, and Tl). *Geochim. Cosmochim. Acta.* **57**, 453-460.

Jones J.H. and Jurewicz A.J.G. (1994) Partitioning of Ir, Re, and Os between solid metal and liquid metal. *EOS Trans. Am. Geophys. Union* **75**, 694-695.

Kaiser T. and Wasserburg G.J. (1983) The isotopic composition and concentration of Ag in iron meteorites and the origin of exotic silver. *Geochim. Cosmochim. Acta* **47**, 43-58.

Keil K. and Wilson L. (1993) Explosive volcanism and the compositions of cores of differentiated asteroids. *Earth Planet. Sci. Lett.* **117**, 111-124.

Kivelson M.G., Khurana K.K., Russell C.T., Walker R.J., Warnecke J., Coroniti F.V., Polanskey C., Southwood D.J., and Schubert G. (1996a) Discovery of Ganymede's magnetic field by the Galileo spacecraft. *Nature* **384**, 537-541.

Kivelson M.G., Khurana K.K., Walker R.J., Russell C.T., Linker J.A., Southwood D.J., and Polanskey C. (1996b) A magnetic signature at Io: Initial report from the Galileo magnetometer. *Science* **273**, 337-340.

Kivelson M.G., Khurana K.K., Joy S., Russell C.T., Southwood D.J., Walker R.J., and Polanskey C. (1997) Europa's magnetic signature: report from Galileo's pass on 19 December 1996. *Science* **276**, 1239-1241.

Konopliv A.S., Binder A.B., Hood L.L., Kucinskas A.B., Sjogren W.L., and Williams J.G. (1998) Improved gravity field of the Moon from Lunar Prospector. *Science* **281**, 1476-1480.

Kracher A. and Wasson J.T. (1982) The role of S in the evolution of the parental core of the iron meteorites. *Geochim. Cosmochim. Acta* **46**, 2419-2426.

Kracher A. (1983) Notes on the evolution of the IIIAB/pallasite parent body. *Lunar. Planet. Sci.* **14**, 405-406.

Kracher A., Willis J., and Wasson J.T. (1980) Chemical Classification of iron meteorites - IX. A new group (IIF), revision of IAB and IIICD, and data on 57 additional irons. *Geochim. Cosmochim. Acta* **44**, 773-787.

Lauer H.V. Jr. and Jones J.H. (1999) Tungsten and Nickel partitioning between solid and liquid metal; Implications for high-pressure metal/silicate experiments. *Proc. Lunar. Planet. Sci. Conf.* **30**, 1617.

Lewis J.S. (1971) Consequences of the presence of sulfur in the core of the Earth. *Earth Planet. Sci. Lett.* **11**, 130-134.

Li C. and Naldrett A.J. (1993) Sulfide capacity of magma: A quantitative model and its application to the formation of sulfide ores at Sudbury, Ontario. *Econ. Geol.* **88**, 1253-1260.

Li J. and Agee C.B. (1996) Geochemistry of mantle-core differentiation at high pressure. *Nature* **381**, 686-689.

Lister J.R. and Buffett B.A. (1995) The strength and efficiency of thermal and compositional convection in the geodynamo. *Phys. Earth. Planet. Int.* **91**, 17-30.

Liu L. (1986) Potassium and the Earth's core. *Geophys. Res. Lett.* **13**, 1145-1148.

Lüder E. (1924) Gleichgewichte zwischen metallpaaren und schwefel. Das ternäre system silber-eisen-schwefel. (Equilibrium between metal pairs and sulfur. The ternary system of silver-iron-sulfur.) *Metall und Erz* **21**(4), 65-69.

Horan M.F., Smoliar M.I., and Walker R.J. (1998) ^{182}W and ^{187}Re-^{187}Os systematics of iron meteorites: Chronology from melting, differentiation, and crystallization in asteroids. *Geochim. Cosmochim. Acta* **62**, 545-554.

MacDonald G.J.F. and Knopoff L. (1958) On the chemical composition of the outer core. *Geophys. J. R. Astron. Soc.* **1**, 284-297.

Malvin D.J. (1988) Assimilation-fractional crystallization modeling of magmatic iron meteorites (abstract). *Lunar Planet. Sci.* **19**, 720-721.

Malvin D.J., Wang D, and Wasson J.T. (1984) Chemical classification of iron meteorites - X. Multielement studies of 43 irons, resolution of group IIIE from IIIAB, and evaluation of Cu as a taxonomic parameter. *Geochim. Cosmochim. Acta* **48**, 785-804.

Malvin D.J., Jones J.H., and Drake M.J. (1986) Experimental investigations of trace element fractionation in iron meteorites. III: Elemental partitioning in the system Fe-Ni-S-P. *Geochim. Cosmochim. Acta* **50**, 1221-1231.

Mermelengas N., De Laeter J.R., and Rosman K.J.R. (1979) New data on the abundance of palladium in meteorites. *Geochim. Cosmochim. Acta* **43**, 747-753.

Morgan J.W., Wandless G.A., Petrie R.K., and Irving A.J. (1980) Composition of the Earth's upper mantle - II: Volatile trace elements in ultramafic xenoliths. *Proc. Lunar Planet. Sci. Conf.* **11**, 213-233.

Murrell M.T. and Burnett D.S. (1986) Partitioning of K, U, and Th between sulfide and silicate liquids: Implications for radioactive heating of planetary cores. *J. Geophys. Res.* **91**, 8126-8136.

Murthy R.V. (1991) Early differentiation of the Earth and the problem of mantle siderophile elements: A new approach. *Science* **253**, 303-306.

Murthy V.R. and Hall H.T. (1970) The chemical composition of the Earth's core: Possibility of Sulphur in the core. *Phys. Earth Planet. Int.* **2**, 276-282.

Mysen B.O. (1991) Relations between structure, redox equilibria of iron, and properties of magmatic liquids, *in* Physical Chemistry of Magmas, L.L. Perchuk and I. Kushiro eds., Springer, New York, 41-98.

Narayan C. and Goldstein J.I. (1982) A dendritic solidification model to explain Ge-Ni variations in iron meteorite chemical groups. *Geochim. Cosmochim. Acta* **46**, 259-268.

Newsom H.E. and Sims K.W.W. (1991) Core formation during early accretion of the Earth. *Science* **252**, 926-933.

Nichiporuk W. and Brown H. (1965) The distribution of platinum and palladium metals in iron meteorites and in the metal phase of ordinary chondrites. *J. Geophys. Res.* **70**, 459-470.

Ohtani E., Kato T., Onuma K., and Ito E. (1992) Partitioning of elements between mantle and core materials and early differentiation of the Earth, *in* High-Pressure Research: Application to Earth and Planetary Sciences, Y. Syono and M.H. Manghnani eds., Terra Scientific Publishing Company, Tokyo, 341-349.

Ohtani E., Yurimoto H., Segawa T., and Kato T. (1995) Element partitioning between MgSiO$_3$ perovskite, magma, and molten iron: Constraints for the earliest processes of the Earth-Moon system, *in* The Earth's Central Part: Its Structure and Dynamics, T. Yukutake, eds., Terra Scientific Publishing Company, Tokyo.

Ohtani E. and Yurimoto H. (1996) Element partitioning between metallic liquid, magnesiowustite, and silicate liquid at 20 GPa and 2500°C: A secondary ion mass spectrometric study. *Geophys. Res. Lett.* **23**, 1993-1996.

Ohtani E., Yurimoto H., and Seto S. (1997) Element partitioning between metallic liquid, silicate liquid, and lower-mantle minerals: Implications for core formation of the Earth. *Phys. Earth Planet. Inter.* **100**, 97-114.

Olsen E.J., Kracher A., Davis A.M., Steele I.M., Hutcheon I.D., and Bunch T.E. (1999) The phosphates of IIIAB iron meteorites. *Meteorit. Planet. Sci.* **34**, 285-300.

Ostro S.J., Campbell D.B., Chandler J.F., Hine A.A., Hudson R.S., Rosema K.D., and Shapiro I.I. (1991) Asteroid 1986 DA: Radar evidence for a metallic composition. *Science* **252**, 1399-1404.

Oversby V.M. and Ringwood A.E. (1971) Time of formation of the Earth's core. *Nature* **234**, 463-465.

Oversby V.M. and Ringwood A.E. (1972) Potassium distribution between metal and silicate and its bearing on the occurrence of potassium in the Earth's core. *Earth Planet. Sci. Lett.* **14**, 345-347.

Oversby V.M. and Ringwood A.E. (1973) Reply to comments by K.A. Goettel and J.S. Lewis. *Earth Planet. Sci. Lett.* **18**, 151-152.

Parker L.J., Atou T., and Badding J.V. (1996) Transition element-like chemistry for potassium under pressure. *Science* **273**, 95-97.

Raghavan V. (1988) Phase Diagrams of Ternary Iron Alloys 2, Indian National Scientific Documentation Centre, New Delhi, India, 360 pp.

Rasmussen K.L., Malvin D.J., Buchwald V.F., and Wasson J.T. (1984) Compositional trends and cooling rates of group IVB iron meteorites. *Geochim. Cosmochim. Acta* **48**, 805-813.

Rasmussen K.L. (1989) Cooling rates of group IIIAB iron meteorites. *Icarus* **80**, 315-325.

Righter K. and Drake M.J. (1996) Core formation in the Earth's Moon, Mars and Vesta. *Icarus* **124**, 513-529.

Righter K. and Drake M.J. (1997) Metal-silicate equilibrium in a homogeneously accreting Earth: New results for Re. *Earth Planet. Sci. Lett.* **146**, 541-553.

Righter K., Drake M.J., and Yaxley G. (1997) Prediction of siderophile element metal-silicate partition coefficients to 20 GPa and 2800°C: The effects of pressure, temperature, oxygen fugacity, and silicate and metallic melt compositions. *Phys. Earth Planet. Int.* **100**, 115-134.

Righter K. and Drake M.J. (1999) Metal/silicate equilibrium in the early Earth – New constraints from the volatile moderately siderophile elements Ga, Cu, P, and Sn. submitted to: *Geochim. Cosmochim. Acta.*

Ringwood A.E. (1966) Chemical evolution of the terrestrial planets. *Geochim. Cosmochim. Acta* **30**, 41-104.

Schmid E.E. (1988) Silver-Iron-Sulfur, *in* Ternary Alloys 2, G. Petzov and G. Effenberg eds., VCH Verlagsgesellschaft, Weinheim, Federal Republic of Germany and VCH Publishers, New York, NY, USA, 106-116.

Schubert G., Zhang K., Kivelson M.G., and Anderson J.D. (1996) The magnetic field and internal structure of Ganymede. *Nature* **384**, 544-545.

Schürmann E. and Neubert V. (1980) Schmelzgleichgewichte in den eisenreichen Ecken der Dreistoffsysteme Eisen-Schwefel-Kohlenstoff, Eisen-Schwefel-Phosphor und Eisen-Schwefel-Silicium. *Giesserei-Forschung* **32**, 1-5.

Schürmann E. and Schäfer K. (1968) Schmelzgleichgewichte in den Dreistoffsystemen Eisen-Schwefel-Kohlenstoff, Eisen-Schwefel-Phosphor und Eisen-Schwefel-Silizium. *Giesserei-Forschung* **24**, 21-33.

Scott E.R.D. (1972) Chemical fractionation in iron meteorites and its interpretation. *Geochim. Cosmochim. Acta* **36**, 1205-1236.

Scott E. R. D. (1977) Pallasites – metal composition, classification and relationships with iron meteorites. *Geochim. Cosmochim. Acta* **41**, 349-360.

Scott E.R.D. and Wasson J.T. (1976) Chemical classification of iron meteorites - VIII. Groups IC, IIE, IIIF and 97 other irons. *Geochim. Cosmochim. Acta* **40**, 103-115.

Scott E.R.D., Wasson J.T., and Buchwald V.F. (1973) The chemical classification of iron meteorites - VII. A reinvestigation of irons with Ge concentrations between 25 and 80 ppm. *Geochim. Cosmochim. Acta* **37**, 1957-1983.

Scott E. R. D. and Wasson J. T. (1975) Classification and properties of iron meteorites. *Rev. Geophys. Space Phys.* **13**, 527-546.

Scott E.R.D., Haack H., and McCoy T.J. (1996) Core crystallization and silicate-metal mixing in the parent body of the IVA iron and stony-iron meteorites. *Geochim. Cosmochim. Acta* **60**, 1615-1631.

Sellamuthu R. and Goldstein J. I. (1985) Analysis of segregation trends observed in iron meteorites using measured distribution coefficients. *Proc. Lunar and Planet. Sci. Conf. 15th, J. Geophys. Res.* **90**, C677-C688.

Shen J.J., Papanastassiou D.A., and Wasserburg G.J. (1996) Precise Re-Os determinations and systematics of iron meteorites. *Geochim. Cosmochim. Acta* **60**, 2887-2900.

Sherman D.M. (1990) Chemical bonding and the incorporation of potassium into the Earth's core. *Geophys. Res. Lett.* **17**, 693-696.

Smales A.A., Mapper D., and Fouché K.F. (1967) The distribution of some trace elements in iron meteorites, as determined by neutron activation. *Geochim. Cosmochim. Acta* **31**, 673-720.

Smoliar M.I., Walker R.J., and Morgan J.W. (1996) Re-Os ages of group IIA, IIIA, IVA, and IVB iron meteorites. *Science* **271**, 1099-1102.

Somerville M. and Ahrens T.J. (1980) Shock compression of $KFeS_2$ and the question of potassium in the core. *J. Geophys. Res.* **85**, 7016-7024.

Stacey F.D. (1992) Physics of the Earth, 3rd edn, Brookfield Press, Brisbane, 513 pp.

Stevenson D.J., Spohn T., and Schubert G. (1983) Magnetism and thermal evolution of the terrestrial planets. *Icarus* **54**, 466-489.

Takahashi E. (1986) Melting of a dry peridotite KLB-1 up to 14 GPa: Implications on the origin of peridotitic upper mantle. *J. Geophys. Res.* **91**, 9367-9382.

Taylor L.A. (1970a) The system Ag-Fe-S: phase equilibria and mineral assemblages. *Mineral Depsoita* **5**, 41-58.

Taylor L.A. (1970b) The system Ag-Fe-S: phase relations between 1200° and 700°C. *Met. Trans.* **1**, 2523-2529.

Tschauner O., Zerr A., Specht S., Rocholl A., Boehler R., and Palme H. (1999) Partitioning of Nickel and Cobalt between silicate perovskite and metal at pressures up to 80 GPa. *Nature* **398**, 604-607.

Ulff-Møller F. (1998) Effects of liquid immiscibility on trace element fractionation in magmatic iron meteorites: A case study of group IIIAB. *Meteorit. Planet. Sci.* **33**, 207-220.

Vogel R. (1961) Ergebnisse ternärer Zustandsdiagramme des Eisens, angewandt auf Fragen der Kosmochemie. *Chemie der Erde* **21**, 24-47.

Wallace P. and Carmichael I.S.E. (1992) Sulfur in basaltic magmas. *Geochim. Cosmochim. Acta* **56**, 1863-1874.

Wänke H. (1981) Constitution of terrestrial planets. *Phil. Trans. R. Soc. Lond. A* **303**, 287-302.

Wasson J.T. (1974) Meteorites: Classification and Properties. Springer-Verlag, New York, New York. 316 pp.

Wasson J.T., Ouyang X., Wang J., and Jerde E. (1989) Chemical classification of iron meteorites: XI. Multi-element studies of 38 new irons and the high abundance of ungrouped irons from Antarctica. *Geochim. Cosmochim. Acta* **53**, 735-744.

Willis J. and Goldstein J.I. (1982) The effects of C, P, and S on trace element partitioning during solidification in Fe-Ni alloys. *Proc. Lunar Planet. Sci. Conf. 13th. Part I, J. Geophys. Res.* **87**, *Supplement*, A435-A445.

Wood B.J. (1993) Carbon in the core. *Earth and Planet. Sci. Lett.* **117**, 593-607.